

**IMAGING CALCIFICATION IN CEREBRAL ANEURYSM TISSUE –  
A MULTI-MODAL APPROACH**

by

**Chih-Yuan Chuang**

B.S., University of Illinois at Urbana Champaign, 2015

Submitted to the Graduate Faculty of  
Swanson School of Engineering in partial fulfillment  
of the requirements for the degree of  
Master of Science

University of Pittsburgh

2018

UNIVERSITY OF PITTSBURGH

SWANSON SCHOOL OF ENGINEERING

This thesis was presented

by

Chih-Yuan Chuang

It was defended on

April 2, 2018

and approved by

Julie Phillippi, Ph.D., Assistant Professor, Department of Bioengineering

Bryan Brown, Ph.D., Assistant Professor, Department of Bioengineering

Thesis Advisor: Anne M. Robertson, Ph.D., Professor,

Department of Mechanical Engineering and Materials Science

**IMAGING CALCIFICATION IN CEREBRAL ANEURYSM TISSUE –  
A MULTI-MODAL APPROACH**

Chih-Yuan Chuang, M.S.

University of Pittsburgh, 2018

Intracranial aneurysms are abnormal bulges in the walls of brain arteries that have high morbidity and mortality rates when they rupture. Because the risks associated with treatment are substantial, it is important to identify patients at lower risk for rupture who can avoid treatment. However, to date, a clinically used tool for risk assessment remains elusive. Our group has recently identified calcification as a remarkably common finding in human cerebral aneurysm tissue and have demonstrated that it can play an important role in generating stress concentrations in cerebral aneurysms. While arterial calcification in atherosclerotic plaques has been the focus of extensive study, relatively little attention has been given to calcification in cerebral aneurysms. The studies of calcification in arteries have addressed the location, development and morphological patterns of calcification in atherosclerosis as well as the possibly beneficial role of calcification in mechanical reinforcement and deleterious role as a source of stress concentration. A central objective of this thesis was the development of protocols for studying calcification and lipid pools in cerebral aneurysms using multiple imaging modalities. These protocols were successfully

developed and then applied to a case study to investigate the relationship between calcification, collagen fibers, and lipid pools. The approaches developed here will be used in an ongoing large-scale investigation of sources of strength and weakness in cerebral aneurysm walls.

## TABLE OF CONTENTS

<b>TABLE OF CONTENTS .....</b>	<b>V</b>
<b>LIST OF TABLES .....</b>	<b>IX</b>
<b>LIST OF FIGURES .....</b>	<b>X</b>
<b>PREFACE.....</b>	<b>XV</b>
<b>1.0 INTRODUCTION.....</b>	<b>1</b>
<b>1.1 INTRACRANIAL ANEURYSMS: PREVALENCE AND TREATMENT ..</b>	<b>1</b>
<b>1.2 CURRENT KNOWLEDGE OF THE PATHOPHYSIOLOGY OF INTRACRANIAL ANEURYSMS .....</b>	<b>3</b>
<b>1.3 ATHEROSCLEROSIS.....</b>	<b>8</b>
<b>1.4 IMPLICATIONS OF CALCIFICATION.....</b>	<b>11</b>
<b>2.0 MATERIALS AND METHODS .....</b>	<b>14</b>
<b>2.1 FLOWCHART.....</b>	<b>14</b>
<b>2.2 BACKGROUND INFORMATION ABOUT ANEURYSM SPECIMENS..</b>	<b>15</b>
<b>2.3 CONTROL TISSUE PREPARATION.....</b>	<b>16</b>
<b>2.4 ANEURYSM TISSUE PREPARATION.....</b>	<b>17</b>
<b>2.5 MICRO-CT SCANNING .....</b>	<b>18</b>
<b>2.6 DISSECTING MICROSCOPE .....</b>	<b>18</b>
<b>2.7 MAPPING .....</b>	<b>19</b>

2.7.1	Mapping for control tissue.....	19
2.7.2	Mapping for aneurysms .....	21
2.8	<b>PROTOCOL FOR FLUORESCENT STAINING OF CALCIFIED REGIONS.....</b>	<b>24</b>
2.9	<b>BACKGROUND ON MULTIPHOTON MICROSCOPY (MPM).....</b>	<b>24</b>
2.9.1	Specialized tissue chamber of MPM analysis.....	26
2.9.2	MPM settings .....	27
2.9.3	3D reconstruction of MPM images .....	27
2.10	<b>TISSUE EMBEDDING .....</b>	<b>28</b>
2.11	<b>CRYOSECTIONING .....</b>	<b>29</b>
2.12	<b>HISTOLOGY.....</b>	<b>32</b>
2.12.1	H&E staining .....	32
2.12.2	Alizarin Red staining (American MasterTech, CA, USA).....	34
2.12.3	Von Kossa staining (Abcam, MA, USA).....	35
2.12.4	Oil Red O staining (Abcam, MA, USA).....	40
2.13	<b>BRIGHT-FIELD MICROSCOPY .....</b>	<b>44</b>
3.0	<b>RESULTS .....</b>	<b>47</b>
3.1	<b>CONFIRMATION OF LIPID POOLS AND CALCIFICATION IN MICRO-CT IMAGES .....</b>	<b>47</b>
3.1.1	H&E staining.....	48
3.1.2	Alizarin Red staining.....	49
3.1.3	Von Kossa staining .....	50
3.1.4	Oil Red O staining .....	51

<b>3.2</b>	<b>ANALYSIS OF ANEURYSM SAMPLE: UIC 011 .....</b>	<b>53</b>
3.2.1	Morphology of UIC 011 .....	53
3.2.2	Imaging calcification and collagen fibers in UIC 011 under Multiphoton Microscopy.....	54
<b>3.3</b>	<b>ANALYSIS OF ANEURYSM SAMPLE: AGH 091 .....</b>	<b>60</b>
3.3.1	Morphology of AGH 091.....	60
3.3.2	Imaging calcification and collagen fibers in AGH 091 under Multiphoton Microscopy.....	62
3.3.3	Categories of relationships between collagen and calcification.....	66
3.3.4	Histology .....	73
<b>4.0</b>	<b>DISCUSSION .....</b>	<b>85</b>
<b>4.1</b>	<b>CONFIRMATION OF CALCIFICATION AND LIPID POOLS IDENTIFIED UNDER MICRO-CT.....</b>	<b>85</b>
<b>4.2</b>	<b>CALCIFICATION LOCATION AND APPEARANCE IN THE ANEURYSM WALL.....</b>	<b>86</b>
4.2.1	Distribution of calcification in the aneurysm wall.....	86
4.2.2	Calcification shape & size observed in the aneurysm wall under different modalities .....	87
4.2.3	Calcification in the artery wall.....	87
4.2.4	Comparison of calcification in the aneurysm and artery wall .....	88
<b>4.3</b>	<b>COLLAGEN FIBERS NEAR CALCIFICATION IN ANEURYSM TISSUE ..</b>	<b>91</b>
<b>4.4</b>	<b>LIPID POOL AND CALCIFICATION .....</b>	<b>92</b>
<b>4.5</b>	<b>COMPARISON OF DIFFERENT MODALITIES.....</b>	<b>94</b>

<b>4.6</b>	<b>MECHANICAL IMPLICATIONS OF THE CALCIFICATION STUDY IN ANEURYSM TISSUE.....</b>	<b>96</b>
<b>4.7</b>	<b>FUTURE DIRECTIONS.....</b>	<b>97</b>
	<b>BIBLIOGRAPHY .....</b>	<b>98</b>

## LIST OF TABLES

Table 1. H&E reagents and functions.....	34
Table 2. Von Kossa troubleshooting.....	39
Table 3. Oil Red O troubleshooting.....	43
Table 4. AGH 091 Abluminal locations selected from 3D reconstruction (2D projections) .....	64
Table 5. luminal locations selected for 3D reconstruction (2D projections) .....	65
Table 6. Summary of relationship categories .....	66
Table 7. Confirmation of calcification and lipid from physical aneurysm tissue with histology .....	74
Table 8. Examples of calcification patterns for aneurysm calcification categories 1-3 and descriptive summary of histological findings for categories $\alpha$ $\beta$ $\gamma$ that have been used for atherosclerotic plaque.....	89
Table 9. Comparison of different modalities for imaging calcification and collagen.....	94

## LIST OF FIGURES

Figure 1. Normal arterial wall structure. Image provided courtesy of P. Fratzl [11]. .....	4
Figure 2. Each square indicates a Chapter 2 section, numbered accordingly based on the sequence of work flow. Connections between these stages are colored as red to represent aneurysms, blue for control.....	15
Figure 3. Circle of Willis from a human cadaver. Region used for this study is outlined in white. ....	17
Figure 4. Control tissue with markers. Blue dye was applied as separate dots at approximately 1 mm apart, to indicate locations as reference for cryosectioning.....	20
Figure 5. Identification of UIC 011 morphology. A, UIC 011 physical sample image taken by a dissection microscope. B, 3D reconstructed micro-CT image of UIC 011, where calcification is marked by the yellow region. ....	22
Figure 6. Identification of AGH 091 morphology. A, AGH 091 physical sample image taken by a dissection microscope. B, 3D reconstructed micro-CT image of AGH 091, where calcification is marked by the yellow region. ....	23
Figure 7. Tissue chamber for MPM analysis. Aneurysm samples UIC 011 and AGH 091 were mounted inside this chamber with the abluminal side as the top surface, in A and B respectively. ....	26

Figure 8. Cryosectioning equipment (Microm HM 525, Thermo Fisher Scientific, MA, US). The white arrows indicate the stationary location of blade, and where tissue specimen is mounted for cryosectioning by moving repeatedly towards the directions pointed by the red arrows..... 31

Figure 9. Alizarin red staining of human kidney. Image provided courtesy of American MasterTech (STARE 100). Free calcium is represented by the bright red areas..... 38

Figure 10. Von Kossa staining of bone. Image provided courtesy of Abcam (ab150687). Calcium deposits are represented by the black areas..... 38

Figure 11. Oil Red O staining of normal human skin. Image provided courtesy of Abcam (ab150678). Lipid droplets are represented by orange red. .... 41

Figure 12. Oil Red O staining of control cerebral artery. Lipid region appears in darker purple at the bottom left corner, circled in light blue, because it was overwritten by hematoxylin ..... 42

Figure 13. H&E staining of control cerebral artery. Subfigure A is a micro-CT image taken near the depth of the associated histology slice, in which lipid appears at low grayscale level. Subfigure B is a 10X image of a cerebral artery cross-section stained with H&E. Subfigure C is a 20X zoom-in image at the black square from subfigure B, capturing the border between cellular and acellular regions..... 48

Figure 14. Alizarin Red staining of control cerebral artery. Subfigure A is a micro-CT image taken near the depth of the associated histology slice, in which calcification appears at high grayscale level, circled in yellow. Subfigure B is the 10X image of a cerebral artery cross-section stained with Alizarin Red. Subfigures C, D, and E are 20X zoom-in images at the black squares from subfigure B..... 49

Figure 15. Von Kossa staining of control cerebral artery. Subfigure A is a micro-CT image taken near the depth of the associated histology slice, in which calcification appears at high grayscale level. Subfigure B is the 10X image of a cerebral artery cross-section stained with von Kossa. Subfigure C is a 20X zoom-in image at the black square from subfigure B. .... 50

Figure 16. Oil Red O staining of control cerebral artery. Subfigures A, B, C, and D are 20X zoom-in images at the black squares from subfigure E. Subfigure F is a micro-CT image taken near the depth of the associated histology slice, in which lipid appears at low grayscale level, circled in yellow. .... 52

Figure 17. UIC 011 Appearance. Subfigure A is the post-fixed image of UIC 011. Subfigure B elaborates on the wall thickness of the entire sample. Subfigures C and D are screenshots of micro-CT images from the abluminal and luminal side ..... 54

Figure 18. UIC 011 MPM Imaging. Subfigure A shows the montage of MPM images from the calcification channel. Subfigure B and C are reproduced from Figure 5 to clarify the calcification region..... 56

Figure 19. UIC 011 MPM Imaging. Subfigure A shows the montage of MPM images from the collagen channel. Subfigure B is reproduced from Figure 5 to illustrate the imaged region, as boxed in orange. .... 56

Figure 20. UIC 011 3D Imaris reconstruction for location a. Subfigure A and Subfigure B are the 3D reconstructed images from the collagen and Cy5 channel of MPM respectively.. 58

Figure 21. UIC 011 Imaris reconstruction for location b. Subfigure A and Subfigure B are the 3D reconstructed images from the collagen and Cy5 channel of MPM respectively..... 59

Figure 22. AGH 091 Appearance. Subfigure A is the post-fixed image of AGH 091. Subfigure B and C are screen-shots of micro-CT images from the abluminal and luminal side. Subfigure D and E elaborate on the wall thickness of the entire sample from the abluminal and luminal views. .... 61

Figure 23. AGH 091 MPM Imaging of collagen and calcification. Subfigure A and B are the montage of 2D projected MPM images captured from the collagen and calcification signal in MPM. Subfigure C merges the 2D projected images from calcification and collagen altogether. Subfigure D is reproduced from Figure 6B to clarify the physical morphology of AGH 091, as well as the calcification region..... 63

Figure 24. AGH 091 Imaging from the luminal side. Squares labeled with a, b and c are the locations imaged under MPM from the luminal side..... 65

Figure 25. Relationship category I between collagen and calcification. Subfigure A and subfigure B were 3D reconstructed images from Imaris, illustrating the collagen and calcification signal separately. Subfigure C merges these two channels..... 68

Figure 26. Relationship category II between collagen and calcification. Subfigure A and subfigure B were 3D reconstructed images from Imaris, illustrating the collagen and calcification signal separately. Subfigure C merges these two channels..... 70

Figure 27. Category III between collagen and calcification. Subfigure A and subfigure B were 3D reconstructed images from Imaris, illustrating the collagen and calcification signal separately. Subfigure C merges these two channels. .... 72

Figure 28. H&E staining of AGH 091. Subfigure A shows 10X image of a cross-section stained with H&E, as well as a micro-CT image (top left corner) taken near the associated depth.

Subfigure B, C, and D are 20X zoom-in images at locations circled in black in subfigure A..... 75

Figure 29. Alizarin Red staining of AGH 091. Subfigure A, D, and G are 10X images of cross-sections stained with Alizarin Red, as well as a micro-CT image taken near the associated depth. Subfigures B, C, E, F, H, and I are 20X zoom-in pictures from the locations circled in black in subfigures A, D, and G. .... 77

Figure 30. Oil Red O staining of AGH 091. Subfigures A, D, and E are cross-sections stained with Oil Red O. Subfigures B, C and G are the micro-CT images at the associated depths. Subfigures F, H and I are 20X zoom-in pictures from locations labeled accordingly in subfigure E ..... 80

Figure 31. Von Kossa staining of AGH 091. Subfigure A is a cross-section of AGH 091 stained with von Kossa. Subfigure B is a 40X zoom-in picture at the location as circled in black and labeled accordingly in subfigure A. Subfigure C is the micro-CT image taken at the associated depth. .... 83

Figure 32. Mix of calcification patterns from category 1 and category 2..... 91

Figure 33. Location of lipid and calcification in the aneurysm sample AGH 091. Subfigure A and B are images of Alizarin Red and Oil Red O stained cross-sections, reproduced here from Figure 29G, and Figure 30E respectively..... 92

## **PREFACE**

This work was supported by NIH Grant 1R01NS097457-01. The completion of this thesis could not have been made possible without the support from many people. I would like to first express my most sincere gratitude to my thesis advisor Dr. Anne M. Robertson for her patience and continuous guidance throughout this research project. I am greatly thankful for her role as my research supervisor during the graduate career. I would also like to thank Dr. Keewon Lee for his help with histochemistry, Dr. Yasutaka Tobe for offering valuable knowledge in aneurysmal pathology and instructions in preparing for my defense presentation, and Piyusha Gade for providing key advices on operating the bioimaging equipment.

I would like to thank my committee members, Dr. Julie Phillippi and Dr. Bryan Brown for serving on my thesis committee and their excellent suggestions and comments. I wish to thank the Alzheimers Disease Research Center (ADRC) of the University of Pittsburgh for providing the control cerebral vessel used in my study, and the Center for Biologic Imaging at the University of Pittsburgh for providing the bioimaging equipment and regular troubleshooting discussions during the process of my imaging work.

## **1.0 INTRODUCTION**

### **1.1 INTRACRANIAL ANEURYSMS: PREVALENCE AND TREATMENT**

An intracranial aneurysm (IA), also known as a cerebral aneurysm, or brain aneurysm, is an abnormal bulge of a brain artery. These lesions can pose life-threatening risks to patients. For instance, when subarachnoid hemorrhage (SAH) occurs, which is frequently a sign of a ruptured aneurysm, blood is released into the subarachnoid space, causing damage on brain cells. In some cases, the bleeding can lead to stroke. The pathogenesis of intracranial aneurysms (IAs) has been debated for many years and still remains unclear. IAs occur in 3% to 5% of the general population and can be characterized by localized structural deterioration of the cerebral arterial wall making the wall vulnerable to rupture [1]. Unfortunately, most are often asymptomatic and never detected until rupture [2]. The consensus has generally been that Finland and Japan are the two countries with a significantly high incidence of aneurysmal SAH when compared to the rest of the world [3][4]. The reason for such high prevalence in Japan and Finland is undetermined. In the US, according to the Brain Aneurysm Foundation, an estimated 6 million people have an unruptured brain aneurysm, or 1 in 50 people.

There are two types of IAs when categorized by geometry: saccular and fusiform. The saccular type accounts for 90% of intracranial aneurysms [5], though fusiform aneurysms are the most prevalent outside the brain. A classic saccular aneurysm is a focal outpouching of the wall of a proximal intracranial artery, typically at a site of bifurcation, and mainly pointing in the direction of blood flow when in the absence of the bifurcation [6]. Most commonly, IAs occur at the circle of Willis, which is a unique vascular region, where several arteries join together to form a circle. This circular formation of vessels ensures that if some of these arteries are blocked, the other arteries belonging to the circle enable blood circulation to the brain. The middle cerebral artery (MCA), Anterior Communication Artery (ACOM), Anterior Cerebral Artery (ACA) and Internal Carotid Artery (ICA) are some of the arteries in the circle of Willis and are also common arteries where aneurysms occur [7][8].

Even though ruptured aneurysms are statistically larger than unruptured aneurysms, there is no size cut-off that can be used to ensure an aneurysm will not rupture [9]. For example, typical results have demonstrated the mean size of unruptured aneurysms to be between 4 and 6 mm, and that of ruptured aneurysms to be between 5 and 8 mm [9]. However, a substantial percentage of rupture aneurysms are even less than 5 mm, indicating that size is insufficient as a single parameter to assess rupture risk [9]. Other risk factors have been identified including age of the patient, pre-existing familial conditions, sex, and hypertension [2]. Smoking has also been associated with higher rate of rupture [2].

Diagnostic tests for the existence of intracranial aneurysms can be done via CT scans, MRI, and cerebral angiogram. Surgeons will normally operate only if there is a high risk of rupture, as the chances that surgical procedures can lead to brain damages are not negligible [10]. Surgical clipping and endovascular coiling are some of the commonly used treatments. In surgical clipping,

the aneurysm neck is clipped during open brain surgery in order to isolate the aneurysm from the circulation and therefore prevent the aneurysms from serving as a source of hemorrhage. This approach is invasive because the skull needs to be opened for surgical access to the circle of Willis.

Endovascular coiling, on the other hand, is a minimally invasive technique. During endovascular coiling, a catheter is guided from the groin up into the artery containing the aneurysm. Platinum coils are then deployed to induce embolization of the aneurysm dome, occluding blood from entering the aneurysmal space. However, in both cases, the possibility remains that a secondary aneurysm may occur. More recently, flow diverters have been introduced as a second endovascular treatment. While promising, this approach also has serious risks.

As of now, there are no medical approaches available other than surgical treatment- either open brain surgery or endovascular. Hence, patients have to make decisions about whether to undergo risky procedures when diagnosed with an aneurysm. For this reason, aneurysm studies to assist in the clinical risk stratification remain of critical importance. Understanding the physical nature of aneurysms is a prerequisite for designing future medical innovations. Researchers and doctors are dedicated to the development of lower risk treatments.

## **1.2 CURRENT KNOWLEDGE OF THE PATHOPHYSIOLOGY OF INTRACRANIAL ANEURYSMS**

The arterial system is a living conduit that can undergo repair and remodeling in response to changes to the mechanical and chemical milieu. However, during a diseased state, such as the case associated with an intracranial aneurysm, structural and pathological changes take place in the

vessel wall, resulting in large deviations from the homeostatic conditions. The pathogenesis of IA formation is a multifactorial and incompletely understood process. At present, the actual cause and location of the aneurysm initiation is yet to be determined, as the pathways might be multiple.

Normal vessel walls are organized into three primary layers: intima (innermost layer), media (middle layer), and adventitia (outermost layer). Each of these layers is composed of a mix of collagen, connective tissues and cellular components. *Figure 1* [11] illustrates a diagram of the major components of a healthy artery. The intima is composed mainly of endothelial cells, which extends throughout the vascular system. At the boundary between the intima and media is a membrane of elastic fibers known as the internal elastic lamina (IEL). The middle part of an arterial wall, also known as the media, is generally the thickest and consists of abundant smooth muscle cells. Further away from the lumen is the adventitial layer, which blends with the surrounding connective tissues outside the vessel and is made up of collagenous fibers in thick bundles.

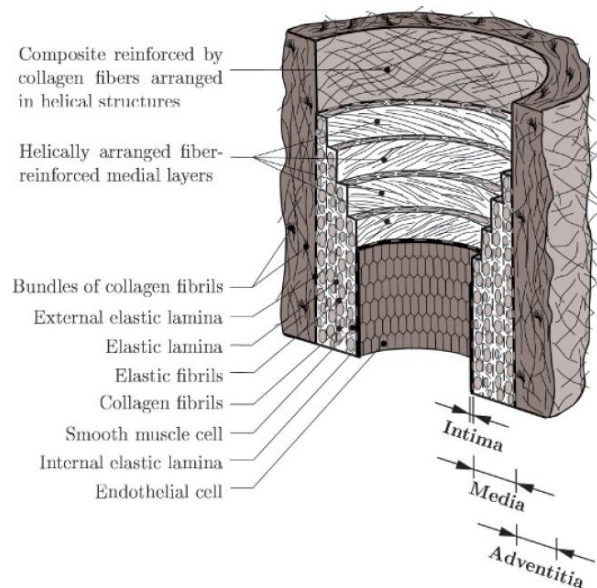


**Figure 1** Normal arterial wall structure. Image provided courtesy of P. Fratzi [11].

In the case of an aneurysm, the wall has fewer distinct layers, generally characterized by disintegration of the internal elastic lamina (IEL) and can include progressive disorganization of the muscular media, intimal hyperplasia, and progressive irregularity of the luminal surface [12]. However, there is great variability. To examine why these pathological changes take place, it is important to first understand how the roles and functions of the IEL, collagen fibers, SMCs, and endothelial cells differ between healthy and aneurysmal wall. Most of our knowledge concerning the pathology of IAs is derived from histological investigations on the autopsy or surgical specimens. Laboratory-based animal models are also used to study IA initiation as well as progression, though they do not necessarily reflect the human condition [13][14].

The existence of the IEL allows an artery to stretch and relax when it is periodically expanded by pulsatile blood flow during the cardiac cycles. In animal models, disruption of the IEL defines early aneurysm formation or early aneurysmal change [15]. The IEL layer has generally been regarded as missing in aneurysm studies. Without this layer, the vessel loses elasticity, potentially leading to focalized bulging of the wall. Collagen fibers and SMCs are key components that provide contribution to the wall's mechanical stiffness and strength. Collagen is the main load bearing element, and relatively inextensible, serving as a structural reinforcement for an artery. In an aneurysm, type I collagen can be found dispersed throughout the wall in stark contrast to a normal vessel, where expression of type I collagen is restricted to the adventitia [15]. However, aneurysm walls differ greatly, and this is not necessarily a common finding. Additionally, type III and IV collagen appear to decrease in an aneurysm [15]. SMCs show a range of phenotypes and contribute in a range of ways to the function of healthy arterial walls. They can alter the diameter of the blood vessel in response to changes in flowrate and can also assume a synthetic phenotype where they contribute to produce extracellular matrix (ECM). Details about

the SMCs behavior in aneurysms will be illustrated in the next paragraph. In a large percentage of aneurysms, the endothelium is missing, which is the inner-most layer that enables the blood vessel to detect changes in flow rate and also protects the arterial wall from being directly in contact with blood. Perturbations in the vascular endothelium are found in both experimental and human aneurysms [12]. It is commonly believed that without the protection of the endothelium, an inflammatory response is triggered which in turn leads to disturbances in the adjacent layers and potentially initiating a physiological pathway that leads to the formation of an aneurysm.

The reason that aneurysmal progression is a cross-disciplinary science is because of the complexity of the coupling of biological pathways involved in aneurysm formation and development which can lead to different case-specific outcomes. As an example, understanding the pathology of SMCs thoroughly would be one of many standalone pieces in solving the aneurysm puzzle. The mechanisms behind a diversity of different functions that SMCs can exert have been a subject of intense research. Physiologically, SMCs are highly sensitive to both the mechanical stress and signals broadcasted radially from a variety of biochemical molecules. We know that, following environmental stimulation, such as nonphysiological flow-induced inflammation, SMCs can alter their phenotype from one primarily concerned with contraction to a pro-inflammatory and matrix remodeling phenotype [16]. When SMCs are contractile, they alter the vessel's luminal diameter, and facilitate appropriate control of blood pressure. But, when remodeling takes place in a vessel wall during conditions such as pregnancy, or after vascular injury, SMCs increase their rate of migration and proliferation, also referred to as the synthetic phenotype. Synthetic SMCs produce large amounts of extracellular matrix (ECM) components, change cell number and connective tissue composition [17].

One study of the histology of the unruptured IAs found the walls frequently display intimal hyperplasia [18], presumed to arise from ECMs produced by synthetic SMCs, as described above. In some reviews, intimal hyperplasia is considered to be a wound healing process that adds strength to a weakening wall as the medial layer thickens. Other studies have suggested that following phenotypic modulation during aneurysm formation, SMCs may ultimately lose their phenotype altogether, both contractile and synthetic, and undergo apoptosis leading to aneurysm rupture [16]. Apoptosis can be considered as silent cell death because it is not accompanied by an inflammatory reaction in contrast with necrosis. Loss of mural SMCs was found to be a characteristic of some ruptured IA walls [19]. Additionally, according to a Japanese study [20], SMCs in the wall of ruptured aneurysms were much more degenerated than those in the unruptured walls and exhibited a higher number of apoptotic bodies. These findings appear to suggest a potential correlation between apoptosis and rupture. However, it is important to consider the possibility that apoptosis was induced as a result of subarachnoid hemorrhage (SAH) and thus a characteristic of the post ruptured wall, rather than a stage in wall degeneration leading to rupture. If a similar level of apoptosis was found in other unruptured cases, then aneurysmal failure might also come from factors other than tissue wall deterioration. The mechanisms by which SMC phenotypic modulation occurs are difficult to trace. Furthermore, we do not yet have a clear understanding about the extent to which SMCs modulate their phenotype in aneurysms. For example, it remains an open question whether SMCs retain any contractility under such diseased state, and if they do, how they contribute to the overall rigidity of the aneurysm structure.

In addition to change in the ECM constituents, IA walls have also been identified with atherosclerotic-like lesion [21]. While in the smallest aneurysms, diffuse intimal thickening (proliferated SMCs) and macrophages are found, in the largest aneurysms, advanced

atherosclerotic lesions with phenotypically modulated SMCs, lipid-laden macrophages, and lymphocytes have been reported [15]. Kosierkiewicz et al. (1994) found that progression of atherosclerosis correlated positively with aneurysm growth [15]. However, there still remains little information on the nature of atherosclerosis in the aneurysm wall. For this reason, the following section, Section 1.3, will be dedicated to introducing a brief overview of background material on atherosclerosis in arteries.

### **1.3 ATHEROSCLEROSIS**

Atherosclerosis is an arterial disease, in which deposits of fat, cholesterol, calcium, and other blood substances build up inside the vessel wall, forming a plaque [22]. As the plaque grows, the vessel wall becomes hardened and thicker, which can then decrease the transport of oxygen-rich blood to other parts of the body. As a result, atherosclerosis can lead to serious problems including heart attack, stroke, or even death.

The immune inflammation processes are responsible for much of the atherosclerotic pathology. Similar to IAs, sites for atherosclerotic lesion formation are usually found in regions of arterial branching or curvature due to the morphology and orientation of the endothelium at these locations. In cylindrical vascular regions, where blood flow is uniform and laminar, endothelial cells are ellipsoid in shape and aligned in the direction of flow [23]. However, in regions where flow is disturbed and possibly even turbulent, endothelial cells lose this alignment, appearing as polygonal shapes without a particular orientation. These latter areas show increased permeability to macromolecules, such as low-density lipoprotein (LDL) [23]. Accumulation of LDL is regarded

as a primary initiation event in atherosclerosis, and the penetration of LDL into the arterial wall sparks a cascade of inflammatory response, as described below in an overview of well-established scientific knowledge that is well described in [24].

Blood leukocytes, also known as white blood cells, are mediators of the host defense and inflammation that participate in neutralizing and removal of injurious agents. In experimental animals, as well as in humans, blood leukocytes are found to localize in the earliest lesions of atherosclerosis, indicating intrusion of matters foreign to the arterial wall [24]. The endothelium is the first layer impacted by inflammation. In normal physiological function, the endothelium does not enable binding of white blood cells. However, when the endothelial monolayer becomes inflamed, it expresses adhesion molecules that are able to bind cognate ligands on leukocytes. Upon adherence to the endothelium, the leukocytes penetrate into the intima, secreting cytokines and growth factors that promote the migration and proliferation of SMCs, enhancing their transformation into a synthetic phenotype. As a result, the phenotypically modulated SMCs express enzymes that degrade elastin and collagen. The subsequent degradation of extracellular matrix permits further migration of the SMCs through the elastic laminae, leading to a growing plaque that diminished the cross section of the lumen.

When analyzing the appearance of an atherosclerotic plaque via H&E staining, or through micro-CT scan, the first grossly visible lesion in the plaque is a fatty streak. Atherosclerosis is believed to start when lipid accumulation appears as confluent extracellular lipid pools and extracellular lipid cores with decreased cellularity [25]. During inflammation, the adhesion molecules secreted by the activated endothelial cells, along with the chemokines and chemo-attractant released from SMCs, draw a variety of white blood cells into a vessel wall. White blood cells are guided by the increasing signal of chemokines concentration at an infected or damaged area. Upon entry, one type of these white blood cells, known as monocytes, transform into macrophages,

take up lipids as multiple small inclusions, and become foam cells. Increasing accumulation of extracellular lipid forms into pools and causes cell necrosis. The enlarging pool dominates the central part of the intima and ultimately occupies 30% to 50% of the wall [25].

Overlying the lipid-rich necrotic core in an atherosclerotic plaque is a layer called the fibrous cap, found just under the endothelium. The cap is made up of fibrous connective tissue that is thicker and less cellular than the normal intima. From observations of patient data across different ages, fibrous cap formation appears to be a relatively late event in atherosclerosis, occurring after and, by implication, as an evolution from macrophage-rich fatty streak lesions [26]. The cap arises from the migration and proliferation of vascular smooth muscle cells and from matrix depositions [27]. Fibrous caps are believed to be both the structural support for an atherosclerotic plaque, and a subendothelial barrier between lumen and the necrotic core. Destroyed caps expose contents of the necrotic core to the lumen, prompting thrombosis and potential artery occlusion. However, many ruptures of thin fibrous caps are clinically silent because they can heal by forming new fibrous tissue matrices which may rupture again followed by thrombus formation [25]. In fact, in 60% of sudden cardiac deaths, cyclic healing of ruptures has been reported [25].

Increasing interest has also focused on understanding how atherosclerotic pathology is related to calcium mineral depositions. Calcification in atherosclerotic plaque has been viewed in some studies as an active and presumably regulated process that exhibits intriguing similarities to new bone formation, or remodeling. For example, the bone morphogen BMP2, which is one of the critical inducers of bone formation, was shown to be expressed in calcifying atherosclerotic plaques of human vessels [28]. Vascular calcification may be localized to atherosclerotic plaques where it occurs as dispersed punctuate or patchy crystals, [29]. Calcification in the atherosclerotic

neointima is detected as microcalcifications, ranging from less than 0.5 to 15 microns [30], in its early stages. There are various paths that lead to the formation of calcification. First, according to [29], microcalcifications near the internal elastic lamina are believed to originate from apoptotic smooth muscle cells (SMC) or matrix vesicles released by these cells. Secondly, they are believed to associate with lipid deposition [30]. The third possibility is that an interaction between macrophages and VSMCs leads to microcalcifications [31]. Vascular SMCs have been shown to differentiate to osteoblast-like cells and enact a cellular process that mediates deposition of bone matrix in blood vessels [32]. Proudfoot et al. [33] suggested that VSMC-derived cell death enables concentration and crystallization of calcium.

#### **1.4 IMPLICATIONS OF CALCIFICATION**

In humans, calcification is found to exist in the majority of advanced atherosclerotic lesions and considered as a great contributing factor to the morbidity of atherosclerosis by decreasing the vessel wall's elasticity. Meanwhile, the calcified mineral deposits in atherosclerosis have been identified as the same mineral as in bone, expressing features during its development process that suggest a mechanism similar to osteogenesis [34][35].

From computational and biomechanical studies of atherosclerosis, the calcification in the atherosclerotic plaque has been shown to change the structure's overall rigidity. However, whether this change diminishes or accelerates the risk of rupture remains an ongoing research discussion. Maldonado et al. [36] suggested that microcalcifications, which are greater than 5  $\mu\text{m}$ , can produce a 200 to 700 % increase in peak circumferential stress and transform a stable plaque into a vulnerable one. In contrast, they concluded that microcalcifications that are less than 5  $\mu\text{m}$  would

not increase risk. Maldonado et al.'s investigation included four categories based on the spatial relation between the microcalcifications and the lipid and necrotic cores. These categories were summarized as i) microcalcifications between 0.5 to 5  $\mu\text{m}$  size at the core boundary, ii) small calcified particles less than 100  $\mu\text{m}$  diameter dispersed within the core, iii) large calcification region greater than 100  $\mu\text{m}$  in diameter found as aggregates within the core, and iv) advanced calcifications that grow beyond the core and extend into the media.

Vengrenyuk et al. [37], and Wenk et al. [38] using modeling approaches to study the impact of microcalcifications on stress in the fibrous cap. Both groups concluded that stress induced by microcalcifications in fibrous caps will increase plaque rupture. Vengrenyuk et al. [37] used a 3D theoretical model that consisted of a rigid spherical inclusion in a fibrous cap located between the lumen and lipid core boundary. This model is in line with the first category of microcalcification patterns used by Maldonado et al. and discussed above [36]. The fibrous cap was subjected to a circumferential tensile stress modeled by unidirectional tension applied at infinity. Their results indicated that the presence of the rigid inclusion increases the local stress around the inclusion, nearly doubling the stress in the direction of the applied tension. They also found that the resultant amplification is almost independent of the size of the particle and relatively insensitive to its position in the fibrous cap. Wenk et al. [38] used numerical modeling in their study, finding that when microcalcification is present in the central portion of the cap, the maximum circumferential stress shifts to this region. In some cases, the average circumferential stress in the fibrous tissue was found to increase by 37.5% relative to the noncalcified case.

On the other hand, there are conflicting studies indicating that calcification stabilizes the plaque [39][40]. Cheng et al. pointed out in [37] that plaque rupture may not always occur in the region of highest stress since the material properties are not necessarily homogeneous. They raised the important question, that if high circumferential stresses significantly predispose a plaque to rupture, then why do some plaques rupture at locations of secondary stress concentration regions rather than regions of maximum stress. They noted that the process of remodeling in the extracellular matrix is dynamic, resulting in unknown changes to the lesion's strength. For this reason, the likelihood of plaque rupture should depend not only on stress concentrations, but also on local defects arising in the plaque. In a different study, to test the hypothesis that calcification impacts biomechanical stress in atherosclerotic plaques, Huang et al. [40] examined a number of physical sample with finite element analysis and found that calcification did not increase mechanical instability. They also noted that calcification may be a marker reflecting the extent of another systematic process, such as inflammation. But, their finding indicated a correlation between lipid and plaque stress: the more lipid a plaque contains, the higher the maximum internal stresses.

## **2.0 MATERIALS AND METHODS**

Chapter 2.0 focuses on standardization of techniques and optimization of histology protocols in support of the study for this thesis. They are explained with sufficient background information and details for future researchers to be able to repeat the successful protocols developed here and to avoid repeating some of the approaches that were not successful.

### **2.1 FLOWCHART**

Figure 2 displays a flowchart that provides an overview of the methods used in this thesis. It provides information on how specimens were prepared, analyzed via histology and observed with bioimaging equipment. Each square in Figure 2 represents an individual stage numbered accordingly based on the sections in this chapter. There are two different paths, in blue and red, represented for the control and aneurysm samples. Connections colored in purple lead to stages where the control, in blue, share the processing procedure with the aneurysm tissue, in red.

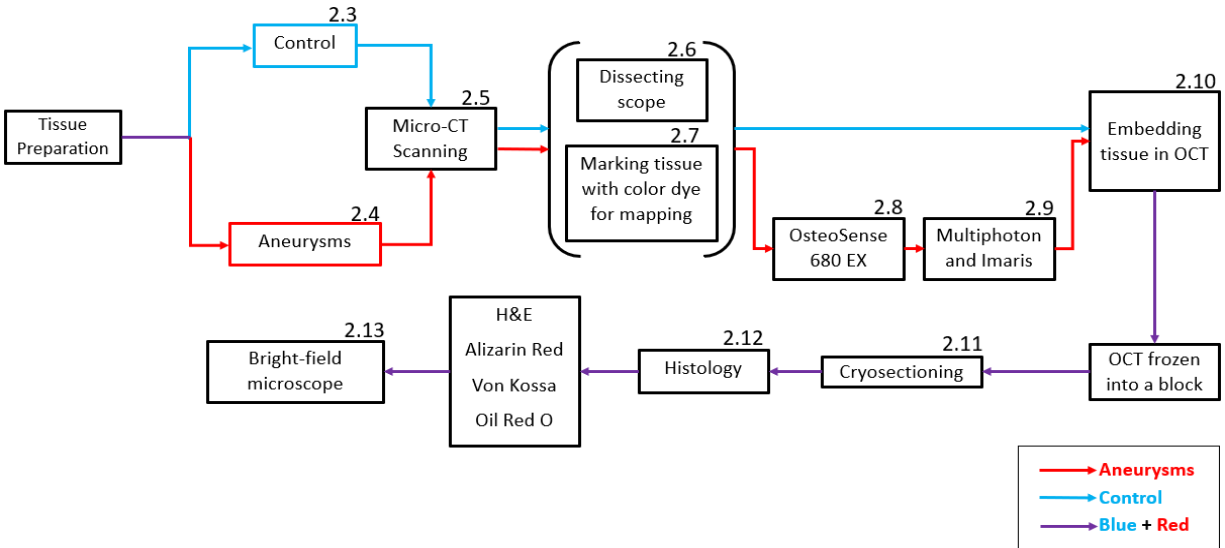


**Figure 2** Each square indicates a Chapter 2 section, numbered accordingly based on the sequence of work flow. Connections between these stages are colored as red to represent aneurysms, blue for control

**2.2 BACKGROUND INFORMATION ABOUT ANEURYSM SPECIMENS**

We consider two aneurysms sample in this thesis, denoted as UIC 011 and AGH 091, which were acquired from University of Illinois at Chicago (UIC), and Allegheny General Hospital (AGH), respectively. Both were harvested from unruptured aneurysms from female patients with no family history of aneurysms. UIC -011 was used for development of some of the techniques and was also quite thin and difficult to handle. Therefore, results for AGH 091 are more complete and representative of results we expect to obtain in samples during future studies.

## 2.3 CONTROL TISSUE PREPARATION

Circles of Willis were harvested from cadavers and supplied to us from the brain bank of the Alzheimer Disease Research 556 Center (ADRC), Figure 3. Upon arrival to our lab, the cadaver tissues were stored unfixed in the minus 20-degree Celsius refrigerator until needed for experiments or data processing. For the purpose of verifying histology staining with H&E, Alizarin Red, von Kossa, and Oil Red O, we picked fresh internal carotid artery from either side of an aged Circle of Willis as a positive control. The region of the artery used in the analysis is traced out with a white curve in Figure 3. The bifurcation region was chosen because we expected an abundance of calcification and lipid in this region, which was in fact the case.

After separating the desired tissue segment from the Circle of Willis, it was fixed in 4% paraformaldehyde (PFA). Fixation is a chemical step in preparation of histological sections that prevents autolysis or putrefaction. According to [41], the optimal time for fixation is determined empirically. If fixation is too short, penetration of fixative to the tissue and crosslinking of macromolecules would not be adequate. Overly long exposure of tissue to fixative may cause over-cross-linking, harden the sample and change its mechanical property to a brittle one. The general rule for fixation penetration is 0.5 mm/hour. In our case, we fixed the control tissue with 4% PFA overnight. The applied volume of fixative was dependent on whether the tissue could be completely immersed.

Post fixed tissue was incubated in 30% sucrose overnight, then stored in 1X PBS until the micro-CT scanning equipment became available. The use of 30% sucrose was so that water would be displaced from tissue, preventing formation of ice crystals inside the tissue wall during

OCT embedding. This is an important step for preservation of the tissue's original morphology. Generally, one way to determine if the incubated tissue had been completely dehydrated by sucrose was by checking whether it sank to the bottom of the immersing solution.

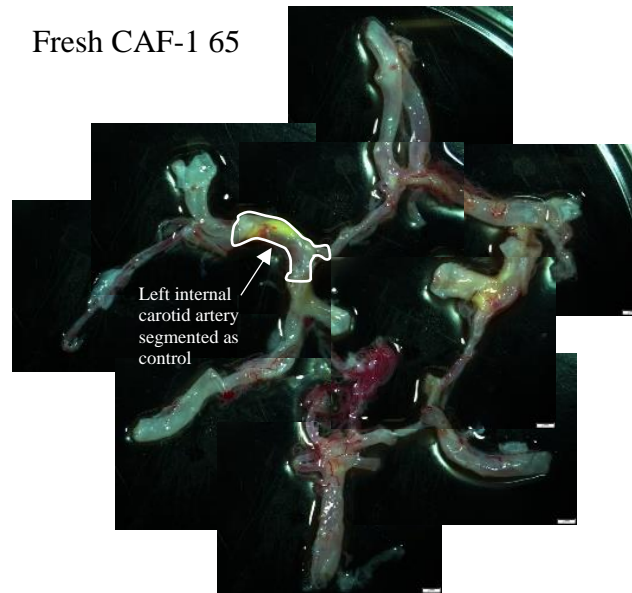


**Figure 3** Circle of Willis from a human cadaver. Region used for this study is outlined in white.

## 2.4 ANEURYSM TISSUE PREPARATION

Both UIC 011 and AGH 091 were preserved long term in 4% paraformaldehyde to prevent bacterial growth. When they were immersed in 30% sucrose for dehydration, the specimens sank directly to the container's bottom, possibly indicating that they were already dehydrated. This could also possibly be due to the fixation method. Further discussion regarding the fixation method and its effects on the final results will be detailed in the Section 4.2, Chapter 4.0.

## **2.5 MICRO-CT SCANNING**

Fixed, intact, control tissues as well as the fixed cerebral aneurysm specimens were scanned using a high resolution micro-CT (Skyscan 1272, Bruker Micro-CT, Kontich, Belgium). In brief, Micro-CT stands for Micro Computed Tomography, which relies on x-ray transmission image technique to analyze the internal structure of materials. The detailed protocol and settings can be found in details from [43].

## **2.6 DISSECTING MICROSCOPE**

Before cryosectioning, staining, or further processing steps, tissues were first inspected under a dissecting microscope (SZX10, Olympus, Tokyo, Japan). These images captured the original morphology and appearance of the specimens. This scope allows for low magnification observation that encompasses the entire tissue area in one window of view. The illumination source and the lens are above the specimen. The image is created from light reflected from the surface of an object rather than transmitted through it. Live view images can be taken during observation through the eyepiece. The orientation of the image captured in the camera is opposite to the actual orientation of the specimen.

## 2.7 MAPPING

One of the objectives of this work is to use classical histology to validate the regions identified as calcification and lipid pools in the micro-CT scans. As a result, it was important to be able to map the locations of the histological sections to the locations in the 3D reconstructed micro-CT data set. In this regard, it was critical to identify the location of cryosectioned samples in the original tissue. As described below, we explored two possible marking methods: tissue dyes and plastic beads. When appropriate, we also used morphological characteristics from observation through a dissecting microscope to confirm the location of the sample.

A second important objective of this thesis was to develop a methodology to determine the calcification distribution in aneurysm samples using multiphoton microscopy. For this second objective, a method was also needed to accurately position the multiphoton lens on the imaging areas of interest.

### 2.7.1 Mapping for control tissue

As just noted, we compared two methods of tissue marking within the control arteries. The plastic beads we considered were 2-50 microns in diameter (Polystyrene Beads, Polysciences, Inc., PA, US). While the plastic beads were good for short term use, in particular visualization under Micro-CT, they typically fell off during tissue processing, with only a few exceptions where they remained partially intact and identifiable. Furthermore, if not carefully applied, the beads could leave indentations and could sometimes cause folds in the tissue, interfering with successful visualization at those particular regions. The dyes we considered were from the Davidson Marking System (Bradley Products, MN, US), including a range of colors, each with a different chemical

makeup. After some preliminary work, we found that the blue dye showed the best adherence and was readily distinguished from the histological staining pigments. Therefore, we determined that dyes were the preferred marking method for histological and MPM analysis and, as a result, are the primary focus of this study. Physical landmarks were also useful for tissues that have distinctive features at the examined spots.

After some preliminary analysis, we developed a simple and useful method for applying the blue dye. Small dots were dabbed across the entire length of the tissue using the tip of a toothpick dipped in blue dye. These dots were aligned perpendicularly to the cryosectioning plane, separated at about 1 millimeter apart, and numbered respectively in a reference diagram, Figure 4. A line was drawn to help with this alignment, and also as a secondary reference in case that blue dots were washed off. A small amount of alcohol was applied to further increase the bonding between the dye and the tissue's surface. The ink was left to dry in air for about one minute before further processing, Figure 4.

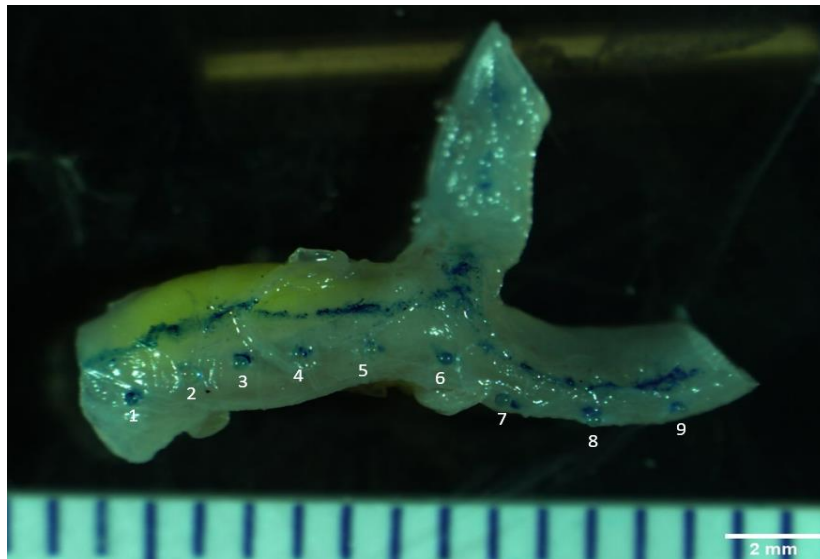


**Figure 4** Control tissue with markers. Blue dye was applied as separate dots at approximately 1 mm apart, to indicate locations as reference for cryosectioning, spacing on ruler is 1 mm.

During cryosectioning, we counted the times at which we encountered these colored locations and match their correspondence with the dots that were numbers on the reference image for the tissue prior to sectioning, Figure 4, thereby providing an estimate of their location on the tissue. For example, cross-sections that first showed the blue ink labeling were assumed to come from the tissue location where the first dot was made. Similarly, cross-sections that first showed up without any dot came from a segment located between the first and second dot on the specimen. The precision of this approach was limited by the size of the dot.

### **2.7.2 Mapping for aneurysms**

#### Mapping steps during cryosectioning

The same mapping approach with blue dye was used for the aneurysm specimens during cryosectioning. The only difference was that aneurysms were much smaller and more heterogeneous on their surface than the control cases, which makes the minimum size of the dye marking a more important limitation. To address this limitation, the information gained from the markers was supplemented by the cutting depths recorded digitally during cryosectioning. This information could then be matched with corresponding location in the 3D reconstructed micro-CT data set.

#### Mapping steps during multiphoton imaging

In the context of microscopic imaging with the multiphoton microscope, two aneurysm specimens were studied for this thesis. As a central objective of this work was to develop a protocol for imaging calcification with the multiphoton microscope, we chose samples which had been identified as having large degrees of calcification and lipid pools from prior micro-CT analysis.

## Mapping for multiphoton imaging of UIC 011

During multiphoton imaging, a cylindrical chamber was used to hold the sample. UIC 011 is a dome shaped sample and was gently flattened in the chamber for imaging. Prior to placement in the chamber, UIC 011 was marked with blue dye along its circumference and one mark on its center, as shown in Figure 5A. These marks helped with creating an imaginary matrix for location reference. While moving the specimen to various x and y coordinates for imaging, we used this matrix, starting from the top left corner. Images were taken in one direction either across consecutive columns with the same row, or across consecutive rows with the same column. During the transition between two imaging locations, we included sufficient overlap to ensure a montage could be created later. It could be seen in the 3D reconstructed micro-CT image, Figure 5B, that UIC 011 has calcification mostly on its left half with some extension to the right. Therefore, we concentrated our analysis in the second quadrant (top left), denoted by a white square in Figure 5.

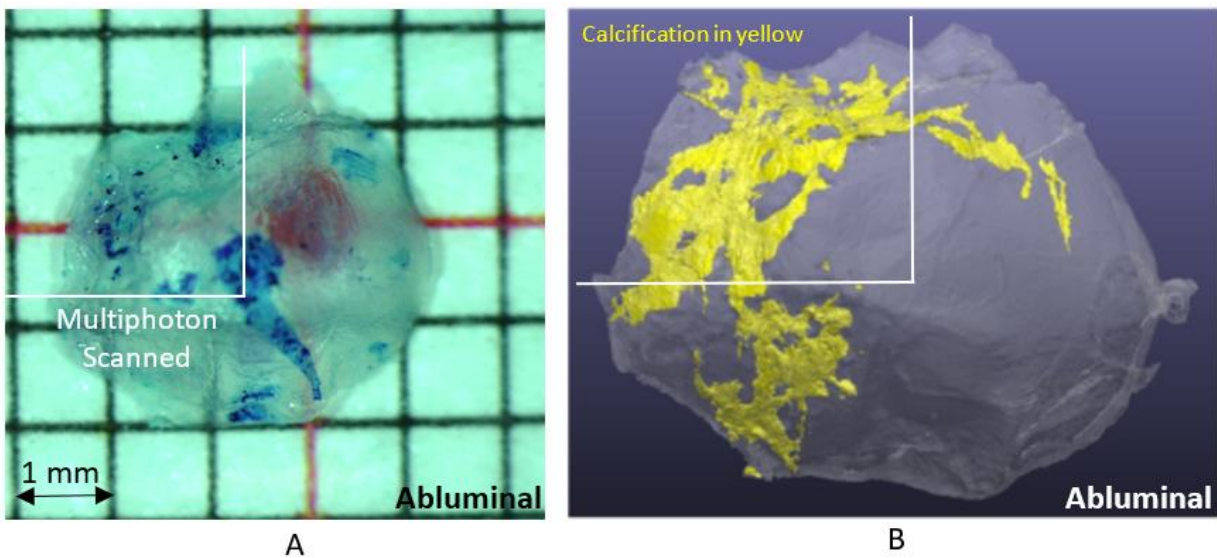


**Figure 5** Identification of UIC 011 morphology. A, UIC 011 physical sample image taken by a dissection microscope. B, 3D reconstructed micro-CT image of UIC 011, where calcification is marked by the yellow region.

## Mapping for multiphoton imaging of AGH 091

Sample AGH 091 has a non-convex shape, and therefore presents greater difficulty in assigning reference locations, Figure 6. From the micro-CT scanning, AGH 091 was found to have a calcified region on the top left corner, as shown in Figure 6B. Therefore, the MPM analysis of this sample was focused on this quadrant. We also relied on manual labeling to quantify locations on the surface of AGH 091 with a matrix. Since the area of focus was much smaller on this specimen, only a small number of dye markers were drawn to indicate left vs. right, and top vs. bottom for imaging purpose, as presented in *Figure 6A*.

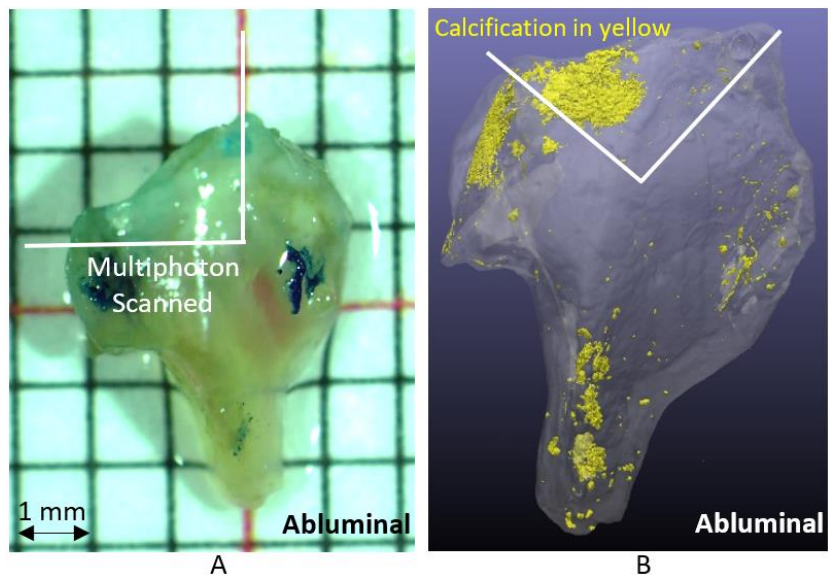


**Figure 6** Identification of AGH 091 morphology. A, AGH 091 physical sample image taken by a dissection microscope. B, 3D reconstructed micro-CT image of AGH 091, where calcification is marked by the yellow region.

## **2.8 PROTOCOL FOR FLUORESCENT STAINING OF CALCIFIED REGIONS**

We developed a protocol using OsteoSense 680 EX (Perkin Elmer, MA, USA) to stain calcification. The difference between OsteoSense and the other staining reagents, such as Alizarin Red, and von Kossa, is that OsteoSense can stain a full-size tissue without additional processing steps. Furthermore, this stain had previously been found to be successful for imaging arterial calcifications under confocal microscope [45], and we therefore prepared the OsteoSense using the previously established protocol [45]. Briefly, the chemical compound arrived in solid form. To create stock solution, it was immersed in 1.2 mL of 1X PBS, wrapped in aluminum foil, and then stored in a 4 degree-Celsius refrigerator. For the working solution, we diluted the stock solution further with 1X PBS, using the 1:100 ratio. For the purpose of this thesis, we stained two aneurysm specimens, UIC 011 and AGH 091 with OsteoSense to visualize in 3D the location of calcification. We were able to identify the signal from OsteoSense using the Cy5 channel (4<sup>th</sup> channel). The respective immersing time frame for UIC 011 and AGH 091 was 48 hours and 56 hours, respectively. The results will be further detailed in Section 3.2.2 and Section 3.3.2, respectively.

## **2.9 BACKGROUND ON MULTIPHOTON MICROSCOPY (MPM)**

Because we are interested in visualizing the presence of calcification and how calcified regions are localized in relationship with collagen fibers, we used MPM to scan aneurysm tissues stained with OsteoSense 680 EX at various locations and reconstructed them in 3D. The concept behind multiphoton microscopy is based on the nonlinear interactions between photons and matter. This imaging technique uses two-photon excitation, which detects the labeled area of a tissue by

delivery of photons to excite the fluorophore in a specimen. Two-photon microscopy has two major advantages. The following information in this and the next paragraph is from a review of [42]. First, two-photon microscopy excitation only occurs at a location where photons coincide, preventing attenuation of the excitation light by fluorophore above or below the point of focus. Two-photon excitation can penetrate up to 1 mm, in the best condition though scanning depths are typically between 150 and 300 microns for the arteries and aneurysms tissue studied here. Depending on the material property of a tissue, this depth can change. Increased spatial resolution, however, sometimes comes with drawbacks, such as tissue damage from high-intensity laser beam, and high-order photobleaching from the high photon flux, which are detrimental for thin specimens less than 10 microns thick. Settings for the scope have to be manually changed to accommodate for these potential hazards.

In order to excite a fluorophore-labeled tissue, a laser emits pulsed near-infrared light at a high speed. When two low-wavelength and low-energy photons meet and are absorbed simultaneously by the same molecule, their combined energy causes transition of the molecule to an excited electronic state. Such excited state remains an extremely short time, from  $10^{-8}$  to  $10^{-9}$  second [40], after which the molecule returns to its original ground state by emitting a new photon. A loss of energy occurs during these processes, and the resulting emitted photon has therefore less energy than the excitation source. Because photon energy is inversely proportional to wavelength, the emitted fluorescence has a longer wavelength than the excitation light. To put this concept in practice, a fluorophore molecule requiring a X wavelength of excitation light can be efficiently excited by a 2X wavelength light when two-photon microscopy is used.

### 2.9.1 Specialized tissue chamber of MPM analysis

MPM Images were taken at 25X, using an Olympus FV1000. Because the aneurysm specimens that we imaged are mostly in the shape of a dome, it would be inconvenient to mount the sample using a regular microscope slide with a coverslip placed on top. However, the inherent curvature of most of these samples prevented them from staying flat. To solve this problem, we used an assembly provided by the Center for Biological Image at the University of Pittsburgh, as shown below in Figure 7. This assembly consists of two threaded metallic rings, where one has a slightly bigger internal diameter than the other. In practice, we would place two separate coverslips between the two rings locked by the threads, and preserve the sandwiched tissue in 1X PBS filling the medium space. Although it was mostly a successful experience in using this assembly, the coverslips would sometimes shatter between the rings if overtightened. Additionally, because the threaded assembly is not air tight, air bubbles can be introduced over time, which are difficult to remove without disassembling the rings. The best approach thus far to reduce air bubbles has been by overfilling the sandwich gap with PBS solution in the first place, and then allowing the excessive overflow liquid to dry out when the two coverslips are merged.

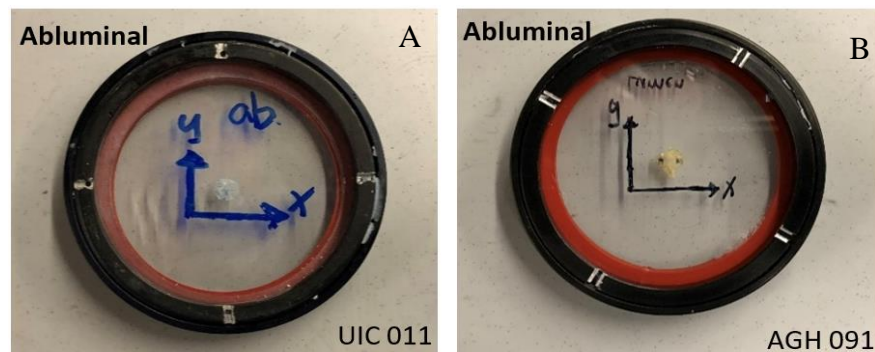


**Figure 7** Tissue chamber for MPM analysis. Aneurysm samples UIC 011 and AGH 091 were mounted inside this chamber with the abluminal side as the top surface, in A and B respectively.

### **2.9.2 MPM settings**

While imaging with the multiphoton microscope, there are a few steps that need careful attention. The first, and most important, step involves setting up the specimen height relative to the lens so as to avoid any chance of damaging the lens during imaging. The specimen stage is first lowered as far below the lens as needed to ensure sufficient space to mount the specimen without potential collision with the lens. During this stage, the lens must be at its bottom most position. Once the specimen had been securely mounted, the stage is brought up close enough to the lens so that the specimen could be successfully focused through the eyepieces. Since the lens is already at its lowest point possible, it would not be allowed to travel further down towards the specimen stage. In this way, damage to the lens in later adjustments could be prevented.

The aneurysm samples were imaged using the following scope settings. The excitation wavelength was 800 nm and the dwell time was 10 microseconds/pixel at a scan pixel count of 1024X1024. The lens was set to travel in either 1 or 2-micron steps from the bottom most layer of the tissue towards the top surface. The imaged stack thickness would be the interval thickness multiplied by the number of vertical scans. The laser intensity was maintained at 7% throughout the imaging process.

### **2.9.3 3D reconstruction of MPM images**

Imaris (Bitplane, Zurich, Switzerland) is a commercially available software, and also provided by the Center for Biologic Imaging at the University of Pittsburgh. This software was used to construct 3D regions from the image stacks obtained from multiphoton analysis. Image qualities had to be manually adjusted to reflect the correct dimensions for each stack imported. The input

parameters were the MPM slice thickness, and the number of total slices. Additionally, the default orientation would always assume the last picture in the stack as the first top slice for reconstruction. For this reason, in order to match with the same orientation that images were taken under the scope, the constructed results were flipped along the y-axis.

## **2.10 TISSUE EMBEDDING**

After fixation and scanning, the tissue was transferred to a plastic embedding mold (cryomold) filled with the OCT compound. The OCT compound is a water-soluble substance made up of glycols and resins that solidifies and provides a specimen matrix for cryostat sectioning at temperature of mins 20-degree Celsius and below. At room temperature, OCT appears as viscous liquid. The fixed artery was slowly and gently immersed into the OCT liquid using a sharp needle, such that no air bubbles would be introduced into the solution. We avoided using other larger tools, such as tweezers, for embedding tissues regardless of size because the OCT compound's high viscosity allows it to cling strongly to a surface, and the larger the surface, the greater the adherence. Because of this effect, embedding with a sharp needle tip prevented mass extraction of the OCT compound when retrieving the tip from inside the fluid. After the arterial tissue had been mounted properly with no air bubbles trapped in close proximity, we adjusted the tissue orientation more precisely to ensure that it would match as closely as possible the same vertical orientation it had during micro-CT scanning.

To prepare the OCT block for cryosectioning, it was conventionally set inside a box of crushed dry ice and left at minus 80-degree refrigerator overnight to freeze. However, if any droplets of water were carried within the tissue wall, the slow overnight freezing process would

allow ice-crystals to form, which might cause distortion in the tissue shape and lead to difficulty in sectioning with the cryostat blade. A good alternative method is to snap freeze at ultra-low temperature. If the specimens were cooled rapidly, the crystals that potentially form would be much smaller and fewer. To increase the freezing speed, we used a super-cool bath of 2-methyl butane at minus 150-degree Celsius. The snap freezing protocol is further detailed as follows. An ice bucket was first filled with liquid nitrogen, approximately 3 cm deep. Also, a glass bucket was filled with 2-methyl butane so that a thin layer of liquid covers the bottom of the container. The bucket was then placed into liquid nitrogen. Vapors would form at first as the 2-methyl butane rapidly cooled. Roughly after 3 minutes, solid white ice became visible at the bottom of the bucket as 2-methyl butane froze. This would be an indication that the liquid had reached its freezing point of minus 150-degree Celsius. At this temperature, the cryomold carrying OCT embedded tissue was dipped into the minus 150-degree Celsius 2-methyl butane. It should never be fully submerged in order that the OCT could be protected from the outside contamination. Complete freeze of the OCT was achieved in approximately three minutes, indicated when the compound turned opaque (white). In the final step, we removed the tissue block and immediately wrapped it in aluminum foil and stored it in a minus 80-degree Celsius freezer.

## **2.11 CRYOSECTIONING**

Once the OCT compound shaped into a frozen cube (tissue block), we transferred it from minus 80-degree Celsius refrigerator to a microtome for cryosectioning. This device was used to cut thin slices of materials so that they could be observed under a microscope. Because OCT block melts quickly when exposed to room temperature, the microtome maintains a minus 20-degree Celsius

environment inside the compartment for cutting. There are several components to the machine, which can be found in Figure 8 with respective captions. The cutting knife plays a significant role in the outcome of sliced sections. The microtome used (Microm HM 525, Thermo Fisher Scientific, MA, US) was equipped with steel blades that can be found commercially available from Thermo Fisher Scientific, MA, USA. In order to achieve consistency in cutting intact tissue slices, the blades were changed frequently. Dull blades might cause cutting artifact and create sections with missing materials, creating artifacts in the histological analysis.

There were a number of steps taken during operation of the microtome. First, we mounted the tissue block on a sample stub by applying OCT in a liquid state in-between the two block and stub and letting them sit inside the microtome's minus 20-degree compartment. In about ten seconds, the cold environment would freeze the applied OCT between the contact surfaces, thus bonding the block and stub together. The stub with the mounted specimen was then tightened onto a stationary holder, which allowed adjustments to align sample with a cutting blade. As we cranked the handle, the tissue block moved towards the blade, as illustrated by the red arrows in Figure 8. Generally, we would start with trimming excessive OCT material before reaching down to the tissue's first surface. All tissues that we cut and used were 8 microns thick. Any thinner sections would more likely peel off during staining protocols and increase handling artifacts.

Common problems that occurred during cryosectioning include upward curling of slices, wrinkling, sections not adhering to cover slides, small holes in tissues, and ripped sections. Upward curling could usually be solved by cooling the tissue block and blade with a freezing spray prior to cutting because it was often due to a temperature difference between them. Another way to uncurl the tissue was by gently pressing the affected areas with a cotton swab until they flattened. In order for sliced frozen sections to be transferred onto glass slides, these slides should have been

kept at room temperature, otherwise, the cold surface would prevent successful adherence. Small holes were sometimes identifiable on the slice, as well as on the block's surface, and from experience, they were mostly caused by trapped bubbles introduced from the embedding process. Additionally, uneven alignment between the tissue block and blade, or slicing with fast speed, would occasionally create ripped and incomplete cuts. When the above situations happened, we would decrease the slicing thickness to a thinner one, such as 5 microns, and continue slicing until the areas of concern were eliminated. Thinner cuts would prevent unexpected, excessive removal of the tissue. Meanwhile, it was important to keep a continuous track of the depth for each cut.

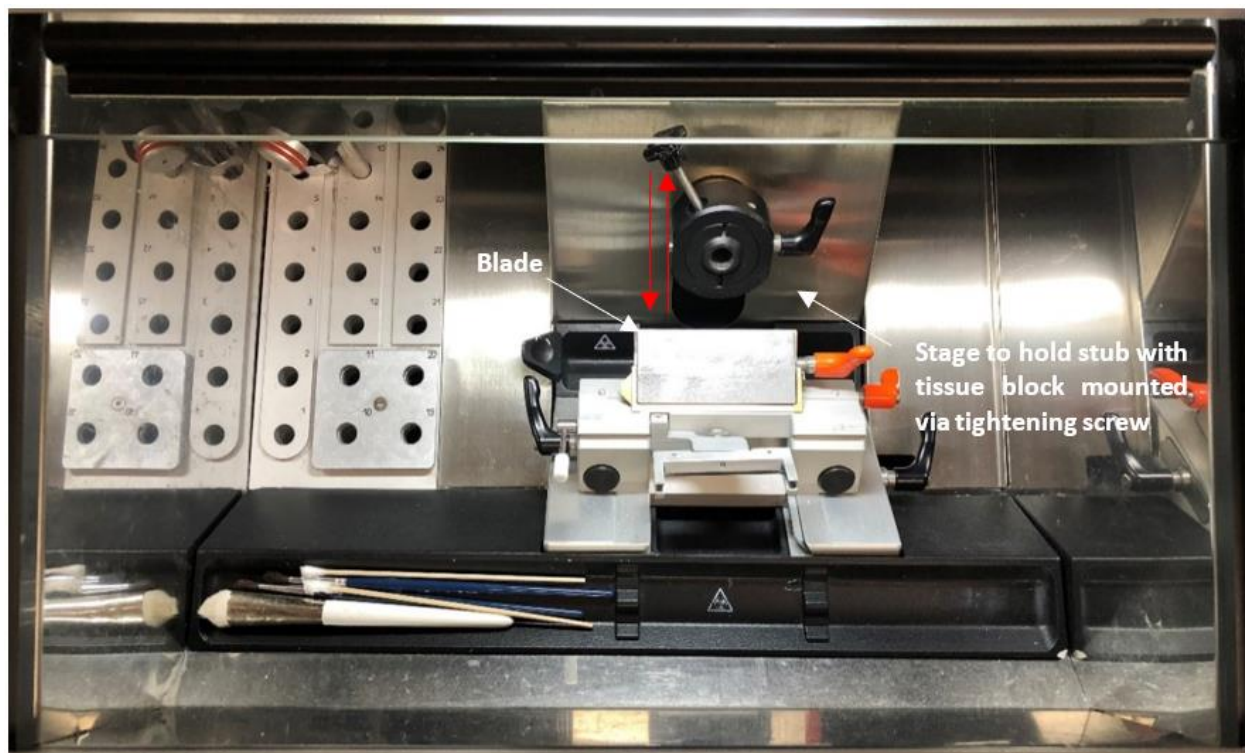


**Figure 8** Cryosectioning equipment (Microm HM 525, Thermo Fisher Scientific, MA, US). The white arrows indicate the stationary location of blade, and where tissue specimen is mounted for cryosectioning by moving repeatedly towards the directions pointed by the red arrows.

## 2.12 HISTOLOGY

### 2.12.1 H&E staining

Most cells are colorless and transparent, and the purpose of staining is so that they can become visible for analysis under a microscope. Hematoxylin and Eosin (H&E) stains are used for recognizing various tissue types and morphologic characteristics. Staining with H&E displays a broad range of cytoplasmic, nuclear, and extracellular matrix features. Hematoxylin can be considered as a basic dye, which has a deep blue-purple color and stains nucleic acids. Eosin, on the other hand, is a pink acidic dye, and stains proteins nonspecifically. Typically, in an H&E stained tissue, nuclei appear as blue, while the cytoplasm and extracellular matrix have different degrees of pink staining. One limitation of H&E staining is that it is not compatible with immunofluorescence. But, the staining protocol is rather fast and easy. To set up a H&E staining station, we used the EasyDip Slide Staining System (Simport Scientific, Quebec, Canada) to sequentially incubate target tissue slides in the respective H&E staining reagents. All tissue sections were frozen sections and had already been fixed with 4% PFA before they were stained. Table 1 below specifies functions of the reagents involved, and the detailed H&E protocol is described as follows.

### Protocol (H&E)

1. When returned to room temperature from storage at the minus 80-degree Celsius refrigerator, tissues slides are first allowed to dry for 15 minutes
2. Incubate slides in 1X DPBS for 3 minutes to dissolve the OCT around tissue
3. Incubate slides in DI water for 1 minute to wash off the dissolved and residual OCT
4. Incubate slides in Hematoxylin for 3 minutes
5. Incubate slides in two changes of DI water for 30 seconds
6. Incubate slides in 1.5%  $\text{NH}_3\text{H}_2\text{O}$ , diluted by distilled water, for 15 seconds.
7. Incubate slides in two changes of DI water for 30 seconds each
8. Incubate slides in Scott's Tap Water for 15 seconds.
9. Incubate slides in two changes of DI water for 30 seconds each
10. Incubate slides in Eosin for 2 minutes
11. Incubate slides in two changes of 95% EtOH for 30 seconds each
12. Incubate slides in two changes of 100% EtOH for 30 seconds each
13. Incubate slides in two changes of Xylene for 30 seconds each
14. Apply mounting medium to seal tissue sides with cover slips on top
15. Sealed slides are left to dry for at least one hour in a hood

**Table 1** H&E reagents and functions

<b>Reagents</b>	<b>Functions</b>
1X DPBS	DPBS provides a balanced PH that's suitable for cell culture applications. In the case of H&E staining, DPBS was used for washing.
DI Water	DI Water is used for washing.
Hematoxylin	Hematoxylin is a staining reagent to stain cell nucleus
1.5% NH <sub>3</sub> H <sub>2</sub> O	Ammonium Hydroxide is used to convert nuclear coloration from reddish purple to a crisp blue/purple.
Scott's Tap Water	Scott's Tap Water also provides bluing of hematoxylin stain, following after the 1.5% NH <sub>3</sub> H <sub>2</sub> O.
Eosin	Eosin is used as a counterstain to hematoxylin and shows other structures in sections of tissue, such as cytoplasm proteins and extracellular matrix.
EtOH (95% & 100%)	Serial incubation with 95% EtOH and 100% EtOH is used to dehydrate the tissue of water. If any water is present, the xylene will cloud in the following step, and the stain will diffuse or fade.
Xylene	Xylene is miscible with alcohol, and as the final step, is used to clear tissues of EtOH.

### **2.12.2 Alizarin Red staining (American MasterTech, CA, USA)**

Alizarin Red staining is a technique used commonly to identify calcium containing osteocytes in paraffin or frozen sections. Stained tissues will display calcium deposits as orange/bright red. The principle reaction is through a chelation process, by which the Alizarin Red Stain binds directly to calcium. We purchased Alizarin Red staining reagents from American MasterTech. For storage, we stocked them at room temperature. The step-by-step staining procedure is further illustrated as below. All tissue sections were frozen sections and had already been fixed with 4% PFA before they were stained. The following protocol is based on information provided by American MasterTech. Figure 9 shows a section from human kidney stained positive with Alizarin Red.

### Protocol (Alizarin Red)

1. When returned to room temperature from storage at the minus 80-degree Celsius refrigerator, tissues slides are first allowed to dry for 15 minutes
2. Incubate slides in 1X DPBS for 3 minutes to dissolve the OCT around tissue
3. Incubate slides in DI water for 1 minute to wash off the dissolved and residual OCT
4. Incubate slice in Alizarin Red Stain for 2 minutes
5. Shake off excess stain
6. Dehydrate slides in Acetone for 15 seconds
7. Place slides in the 1:1 ratio Acetone/Xylene solution for 15 seconds
8. Clear slides through 3 changes of Xylene
9. Apply mounting medium to seal tissue sides with cover slips on top
10. Sealed slides are left to dry for at least one hour in a hood

### **2.12.3 Von Kossa staining (Abcam, MA, USA)**

The von Kossa stain is intended for use in the histological visualization of calcium salts in paraffin or frozen sections. Stained slices will display calcium in mass deposits as black, calcium in dispersed deposits as grey, nuclei as red, and cytoplasm as light pink. The working principle is not specific for calcium itself, but rather by treating tissues with a silver nitrate solution. The silver ion substitutes calcium in calcium salts, such as calcium phosphate. Use of UV light or photographic developer then turns the silver black, therefore staining the distribution of calcium. Von Kossa staining works best when large amounts of phosphate and carbonates are present, as with bones, because it only stains calcium bound to an anion. The step-by-step staining procedure is further illustrated as below, and optimized based on the staining results. Table 2 below presents

troubleshooting for problems that occurred during von Kossa staining, and summarized the relevant solution for future attempts. All tissue sections were frozen sections and had already been fixed with 4% PFA before they were stained. For the purpose of study in this thesis, we purchased the von Kossa staining kit (ab150687) from Abcam. When not in use, the reagents are stored in a 4 degree-Celsius refrigerator. The following protocol has been modified, based on the information provided by Abcam, to better accommodate the staining quality of our specimens. Figure 10 shows positive von Kossa staining of bone using Abcam's protocol.

### Protocol (Von Kossa)

1. When returned to room temperature from storage at the minus 80-degree Celsius refrigerator, tissues slides are first allowed to dry for 15 minutes
2. Incubate slides in 1X DPBS for 3 minutes to dissolve the OCT around tissue
3. Incubate slides in DI water for 1 minute to wash off the dissolved and residual OCT
4. Incubate slide in Silver Nitrate Solution (5%) for 20 minutes with exposure to ultraviolet light. Maintain a height distance of roughly 15 cm between the slides and the ultraviolet light source from above.
5. Incubate slides in Sodium Thiosulfate Solution (5%) for 2 minutes.
6. Slot tissue slides vertically into a staining case pre-filled with tap water, then place the case approximately 5 cm near the tap.
7. Rinse for 2 minutes in running tap water, and be careful not to wash the tissues off as the unsteady intensity of flow can easily peel them off. Do not focus the tap water stream directly onto or too close to the tissues.
8. Incubate slides in two changes of DI water for one minute each
9. Dehydrate with three changes of fresh absolute alcohol
10. Apply mounting medium to seal tissue sides with cover slips on top
11. Sealed slides are left to dry for at least one hour in a hood

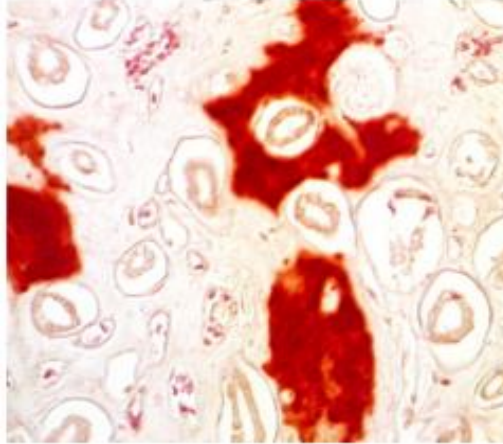


**Figure 9** Alizarin red staining of human kidney. Image provided courtesy of American MasterTech (STARE 100). Free calcium is represented by the bright red areas.

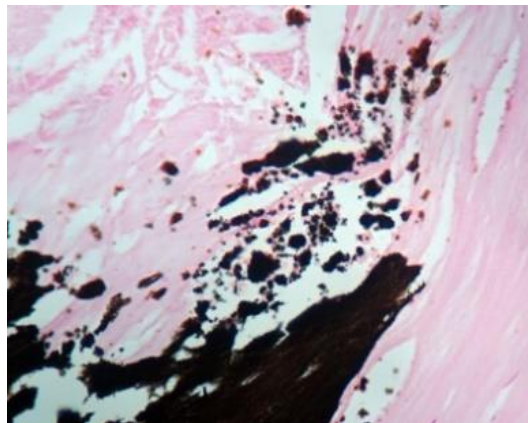


**Figure 10** Von Kossa staining of bone. Image provided courtesy of Abcam (ab150687). Calcium deposits are represented by the black areas.

**Table 2** Von Kossa troubleshooting

No.	Problem	Cause	Solution
1.	Debris were seen floating in 5% Silver Nitrate Solution after 20-minute-long incubation under UV light.	The PBS/DI water washing steps were not carried out thoroughly, and there was still residual OCT remaining around the tissue before incubation with the Silver Nitrate Solution (5%).	Use the EasyDip Slide Staining System to completely immerse tissue slides in the washing steps with PBS and DI water. Pipetting PBS/DI water on the tissue slides would require shaking the liquid off afterwards, which wouldn't be as efficient in the removal of OCT debris.
2.	Majority of the tissue's area appeared as black, as if it were burned.	There could be two reasons for this to happen. First, overly long exposure time to the ultraviolet light could compromise von Kossa's coloration. Also, if placed too close to the light source, tissue cells would potentially be damaged.	From trials and errors, a combination of 20-minute-long UV light exposure with a distance of roughly 15 cm between tissues and light source leads to the most optimal results.
3.	Under coloration of tissue with von Kossa stain, or none at all.	This happened when the UV light exposure time was too short, or when the tissues were placed too far away from the UV light source. Another cause might also be that there was no calcification on the tissue section to begin with.	Same as the solution for problem 2. It is also best to check with micro-CT scanning images, which would indicate whether calcifications are present on the tissue sections before staining.
4.	Tissues were peeled off by the washing steps.	This scenario frequently happened when tap water was running across the tissue sections. Another cause would likely be that the tissue's thickness was too thin from croysectioning.	Bring slides closer to the running tap water, and indirectly wash them by incubating them in a container pre-filled with tap water and aiming the flow into the contained instead.
5.	The tissue section was only partially stained and processed.	This sometimes happened when the tissue sections were not fully immersed in the staining reagents.	Before applying the staining reagents, draw a circle with water repellent PAP pen around the tissue, which then confines the applied liquid within its boundary.

#### **2.12.4 Oil Red O staining (Abcam, MA, USA)**

Oil Red O is a dye used to demonstrate the presence of lipid and fat on frozen tissue sections. We used the Oil Red O Kit (ab150678) from Abcam, which can be stored at room temperature. This staining will theoretically present fat cells as red, neutral fat as red, and nuclei as blue. It cannot be performed on paraffin embedded sections because fat would be removed by alcohols and the clearing agents, such as xylene, used for paraffin processing. The working principle of Oil Red O is not through chemical bonds, but in fact by functioning as an oil-soluble colorant. Chemically, staining lipids presents difficulty to histologists because they are relatively unreactive.

Furthermore, lipids do not stay in tissues after routine processing. They tend to be dissolved and leached out. During staining, in a tissue containing fat, the Oil Red O moves from its original solution to the tissue's fat because the dye has greater solubility in neutral fats than in its original solvent. Oil Red O stained sections are typically counterstained with hematoxylin to present the characteristics of cell nucleus. When staining is complete, they must be mounted with an aqueous medium, contrary to the medium used in the H&E, Alizarin Red, and von Kossa staining. From numerous trial and error attempts, mounting Oil Red O stained slides with medium other than the aqueous type would lead to the positively stained sites being removed and coloration fading. Table 3 details some of the staining challenges with Oil Red O and the respective troubleshooting actions used during the optimization process. The Oil Red O staining protocol can be found in details below, which has been modified based on the original version provided by Abcam's website. Figure 11 shows an example of Oil Red O staining on normal frozen human skin from Abcam.

### Protocol (Oil Red O)

1. When returned to room temperature from storage at the minus 80-degree Celsius refrigerator, tissues slides are first allowed to dry for 15 minutes
2. Incubate slides in 1X DPBS for 3 minutes to dissolve the OCT around tissue
3. Incubate slides in DI water for 1 minute to wash off the dissolved and residual OCT
4. Stain in Hematoxylin (Modified Mayer's) from Abcam's staining kit for 5 seconds
5. Wash thoroughly in running tap water for 3 minutes, and carefully ensure not to wash the tissues off as the unsteady intensity of flow can easily peel them off. Do not focus the tap water stream directly onto or too close to the tissues.
6. Incubate in 1.5%  $\text{NH}_3\text{H}_2\text{O}$ , diluted by distilled water, for 15 seconds to convert nuclear coloration from reddish purple to a crisp blue/purple.
7. Wash in two changes of DI water for 30 seconds each
8. Place in absolute propylene glycol for 2 minutes to avoid carrying water into Oil Red O.
9. Stain in Oil Red O solution, pre-warmed to 60-degree Celsius, for 10 minutes
10. Differentiate in 85% propylene glycol solution for 2 minutes.
11. Wash in two changes of DI water for one minute each

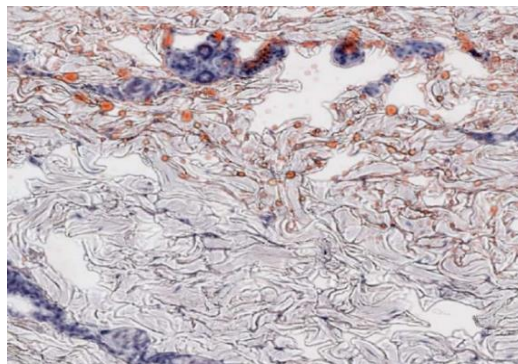


**Figure 11** Oil Red O staining of normal human skin. Image provided courtesy of Abcam (ab150678). Lipid droplets are represented by orange red.

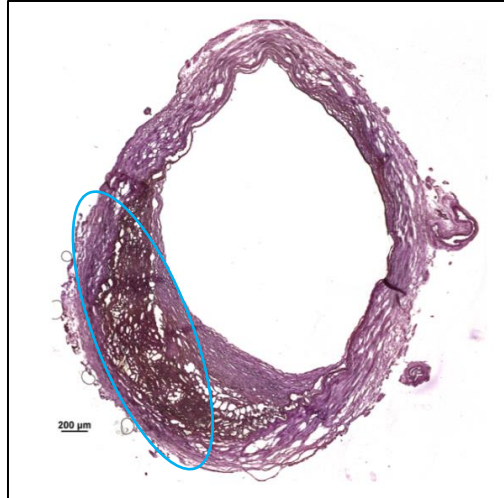


**Figure 12** Oil Red O staining of control cerebral artery. Lipid region appears in darker purple at the bottom left corner, circled in light blue, because it was overwritten by hematoxylin

Conventionally, Hematoxylin counterstaining is performed as the final steps. But, we reversed the conventional protocol and started first with hematoxylin for the following reason. From trials and errors, we noticed that Hematoxylin would always overlap to some extent with regions that showed positive with Oil Red O staining. As a result, the red dye from Oil Red O was frequently overwritten by Hematoxylin's color and became hard to detect, as shown by Figure 12. This might be due to the presence of some dispersed population of cells near the lipid pools. Since the color of Hematoxylin is much darker than Oil Red O's, reversing their order would help with better differentiation. So far, the reversed sequence has been successful in attempts to stain frozen sections with Oil Red O, which were previously identified with lipid regions based on micro-CT scan. Table 3 below documents some of the challenges that we encountered during optimization of Oil Red O staining, and the relevant solutions used to solve them.

**Table 3** Oil Red O troubleshooting

No.	Problem	Cause	Solution
1.	Lipid areas could not be seen or vaguely appeared after staining	No lipid regions identified from micro-CT scanning from the beginning	Always start with micro-CT scanning before histology staining
		Oil Red O solution was not heated up to 60-degree Celsius before it was applied to the staining section	Use water bath to heat up Oil Red O solution prior to running the protocol. It may take roughly 15 minutes for Oil Red O to reach the set temperature.
		Lipid staining was overwritten by hematoxylin	Reverse the place of hematoxylin with Oil Red O in the staining protocol
		Incubation time of staining sections with Oil Red O was too short	Increase the incubation time to 10 minutes
		Lipid coloration was affected by the mounting medium	Must use the aqueous type mounting medium to prevent Oil Red O stained cites from dissolving
		Tissue's lipid regions could have been removed by cryosectioning	Increase the thickness of cut
		Lipid was washed off during the staining protocol, leaving holes on the tissue section as their original locations	The rinsing steps were carried out for too long. For example, it is best not to exceed the one-minute length and number of times to wash with PBS/DI water
2.	Hematoxylin stain was too strong, appearing as dark purple in the background	The amount of hematoxylin solution applied to the tissue section was too much	Apply no more than 100 microliters
		The incubation time with hematoxylin was too long	5-second by far yields the most ideal results
Problem 4. from the von Kossa section			
Problem 5. from the von Kossa section			

## 2.13 BRIGHT-FIELD MICROSCOPY

Stained histology sections must have been mounted with coverslips before they were examined under a microscope. Without coverslips, coloration from staining would fade away while in direct contact with air and unidentified source of debris. Coverslips would allow long term storage and prevent tissue damages affecting interpretations of histology information.

Bright-field microscopy is the simplest of all the optical microscopy illumination techniques, and widely used for stained or naturally pigmented specimens. Each sample placed on a tray is illuminated from above and observed through different magnification of lenses from below. For this reason, the specimen's top surface faces downwards at the lens. Throughout the work of this thesis, Eclipse Ti-E Nikon has been used for observations of all stained sections. Staining images were taken at 10X for full view and 20X for zoom-in at concentrated regions of interest.

There are two options to view a specimen on the microscope, one through the eyepieces and the other on a digital monitor. After powering on all the associated equipment, we would start our view with the eyepieces and adjust the lens accordingly such that the specimen became in focus. A successful adjustment would allow display of defined boundaries around the specimen. After selecting the desired magnification and focusing on the intended tissue area, we would then set the most appropriate exposure intensity for the microscope camera. Longer exposure time creates a brighter image, as the shutter is set to remain open for a longer period. Since different tissue sections were stained with different markers, the amount of exposure time varied from case to case. The general rule is to generate a well illuminated appearance of the stained tissue area while avoiding saturated views.

Adjustment on the level of white balance also had to be made. The difference between a camera and our eyes is that we are able to register a white object as white regardless of the illumination source, whether it be from the sun or a light bulb. However, digital cameras need to be adjusted for different types of lighting in order to render a white object white. Tuning with white balance provides a means to create a higher quality image, yielding better visualization of the staining results. Another important step that we took in setting up the microscope was to correct for uneven illumination in the field of view by a method called background correction. Background correction should be done prior to capturing an image so that the view could avoid nonuniform spatial patterns, in which the middle regions is brighter and light intensity decreases towards the edges. Bright-field microscope typically has built-in functions to run auto-exposure, auto-white-balance, and auto-background-correction. We would usually start with these default features and follow up with a few additional manual iterations until finding satisfactory values were obtained for each setting.

Most pictures were captured as stitched images from separate regions on a tissue. If the image quality wasn't tailored appropriately at each individual view, stitching up a number of them would magnify the errors and result in visual defects. Once the setup was completed as described, we would calibrate the specimen's stage. Calibration was done to ensure that the scope's software could recognize the correct locations while stitching the captured images. If the stage was not properly calibrated, there might be different sizes of overlaps and misplacements on a stitched image. The way that the camera constructed a stitched image was by user-defined boundaries and corners. Finer focus could be applied to views at different locations during the stitching process. Once the stitch was made, we furnished the captured screen of view with moving the lookup table bars from the software. A look up table is essentially a digital file that helps with transforming the

colors and tone of an image. For example, in von Kossa calcification staining, we would want the staining outcomes indicated as black to stand out from the red/light pink background, and we would do that by decreasing the tone of the background RGB colors such that the darker objects stand out more clearly. Depending on the subjects of interest for presentation, a look up table can be altered frequently as desired.

## **3.0 RESULTS**

### **3.1 CONFIRMATION OF LIPID POOLS AND CALCIFICATION IN MICRO-CT IMAGES**

Cadaver cerebral artery tissue from patients who had not been previously diagnosed with presence of cerebral aneurysm was used to validate our approach for identifying lipid pools and calcification in the micro-CT images. In particular, the results of histology staining from H&E, Alizarin Red, Oil Red O, and von Kossa were compared with the cross-section micro-CT images, acquired as close as possible to each associated histology slice. As noted above, in the micro-CT images, lipid pools were identified as the areas of dark low grayscale value, and calcification as regions of high grayscale value (nearly white in color).

### 3.1.1 H&E staining

H&E staining revealed the cell nuclei (stained in deep blue/purple), and the location of other acellular substance, stained in pink. For example, as shown by Figure 13, the acellular region in Figure 13C is seen in the region identified as the lipid pool location, circled in yellow in Figure 13A.

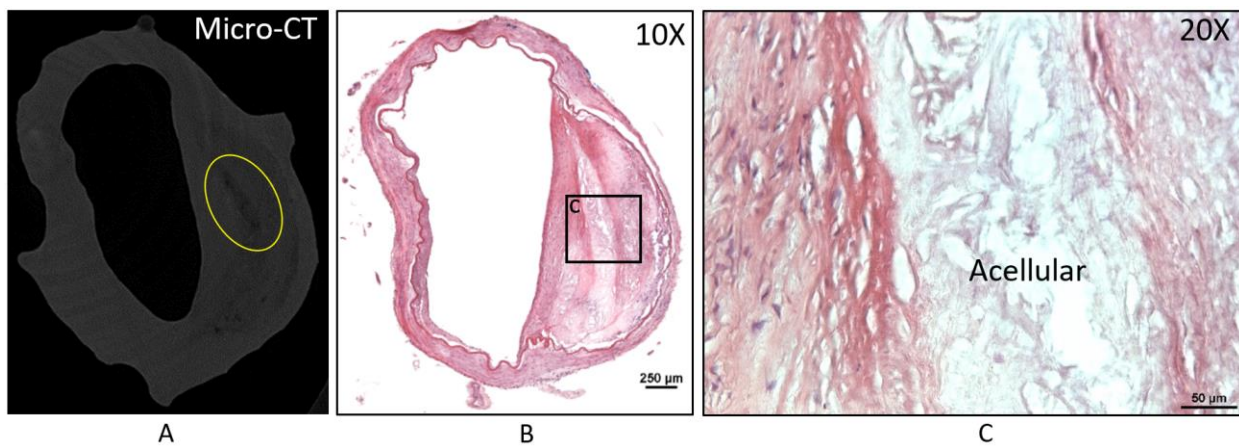


**Figure 13** H&E staining of control cerebral artery. Subfigure A is a micro-CT image taken near the depth of the associated histology slice, in which lipid appears at low grayscale level. Subfigure B is a 10X image of a cerebral artery cross-section stained with H&E. Subfigure C is a 20X zoom-in image at the black square from subfigure B, capturing the border between cellular and acellular regions

### 3.1.2 Alizarin Red staining

Alizarin Red stains free calcium as bright red on a histological cross-section. In Figure 14, the bright red signal from Figure 14C and Figure 14D correspond to the location of the calcification in the micro-CT image in Figure 14A, which is also circled in yellow. Calcification is seen as both singular and aggregated particles. Additionally, their location overlaps with the acellular region identified from H&E. Specifically, the appearance of areas circled in black from Figure 14C, Figure 14D, Figure 14E match with the region labeled as acellular from Figure 13C.

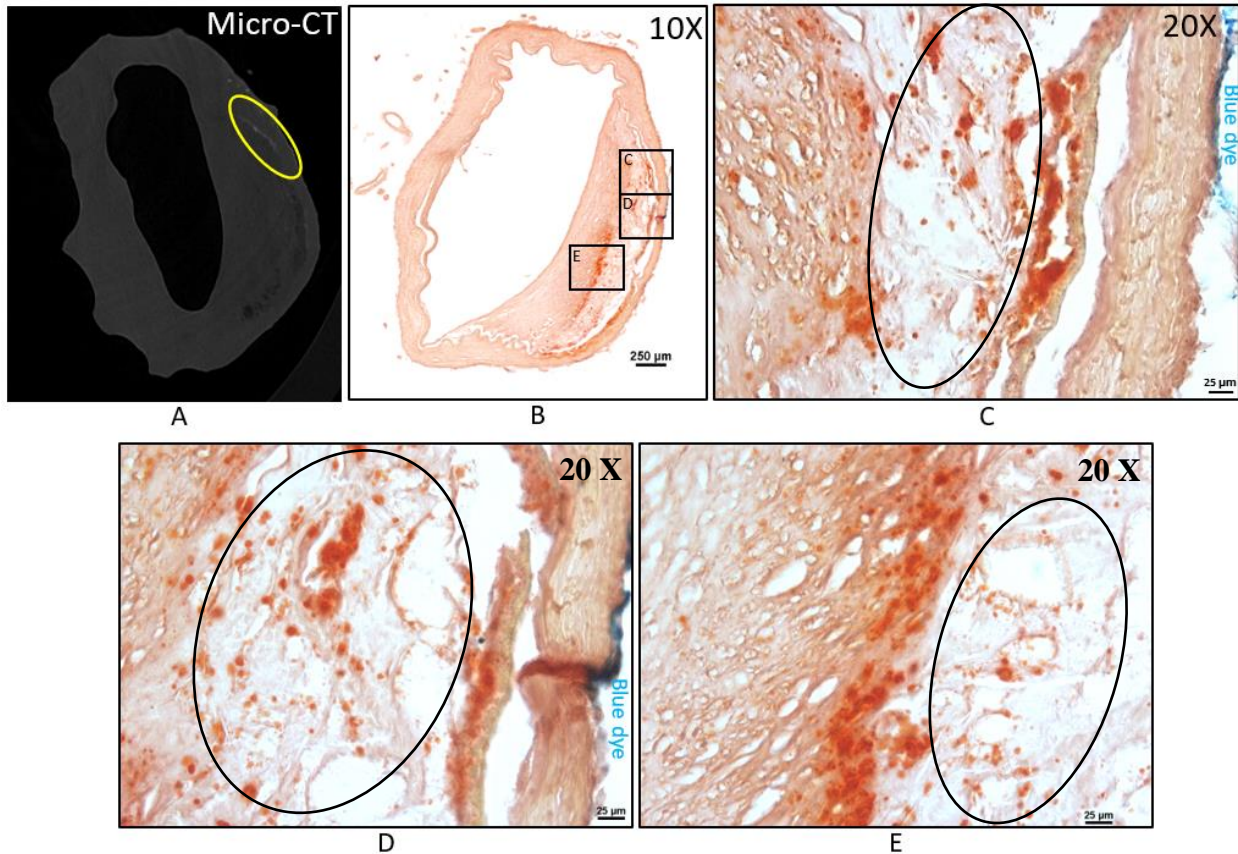


**Figure 14** Alizarin Red staining of control cerebral artery. Subfigure A is a micro-CT image taken near the depth of the associated histology slice, in which calcification appears at high grayscale level, circled in yellow. Subfigure B is the 10X image of a cerebral artery cross-section stained with Alizarin Red.

Subfigures C, D, and E are 20X zoom-in images at the black squares from subfigure B.

### 3.1.3 Von Kossa staining

Von Kossa stain binds specifically to calcium phosphates and for this reason the positively stained region with von Kossa is more limited than Alizarin Red, a more general stain of calcium deposits. When comparing between Figure 14 and Figure 15, Alizarin Red and von Kossa identify the same region with calcification, matching with the information from micro-CT. Calcification identified via von Kossa also appears as either disperse individual particles, or as aggregates ones, but much smaller than in Alizarin Red staining.

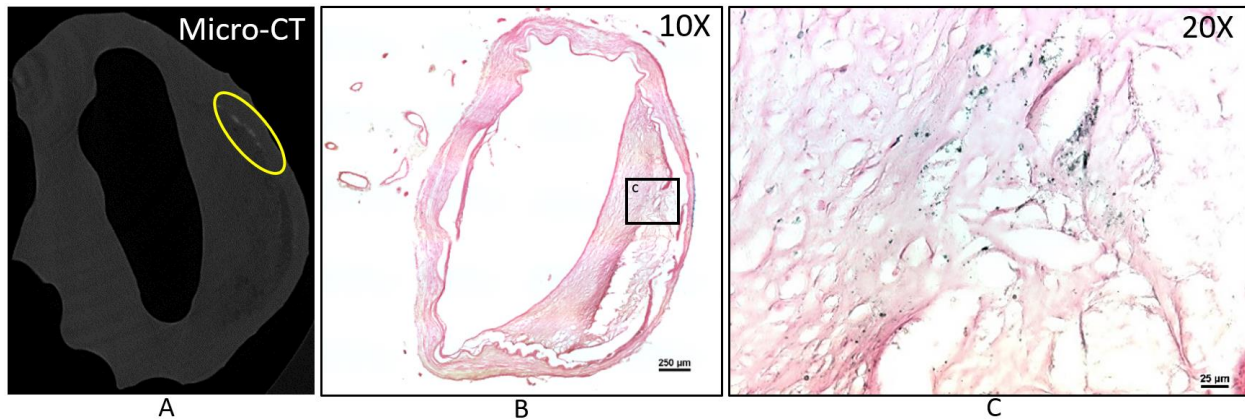


**Figure 15** Von Kossa staining of control cerebral artery. Subfigure A is a micro-CT image taken near the depth of the associated histology slice, in which calcification appears at high grayscale level. Subfigure B is the 10X image of a cerebral artery cross-section stained with von Kossa. Subfigure C is a 20X zoom-in image at the black square from subfigure B.

### 3.1.4 Oil Red O staining

Oil Red O staining was used to identify lipid, which would be labeled with red/orange color. Also included in the staining protocol was hematoxylin, which stains cell nuclei as deep blue. It is noticeable that the morphology of the micro-CT slice from Figure 16F differs from that of the histology slice in Figure 16E. This is the case because they are not the exact same slice, though nearby. We can, however, still see that the lipid regions identified via micro-CT, circled in yellow, are relatively close to the positively stained Oil Red O areas, Figure 16A through Figure 16D, shown at 20X. Consistent with observations in H&E, stained lipid regions are seen to be acellular, Figure 16C and Figure 16D. Cell density is seen to decrease toward the direction of lipid, as denoted by the black arrow heads also in Figure 16C and Figure 16D.

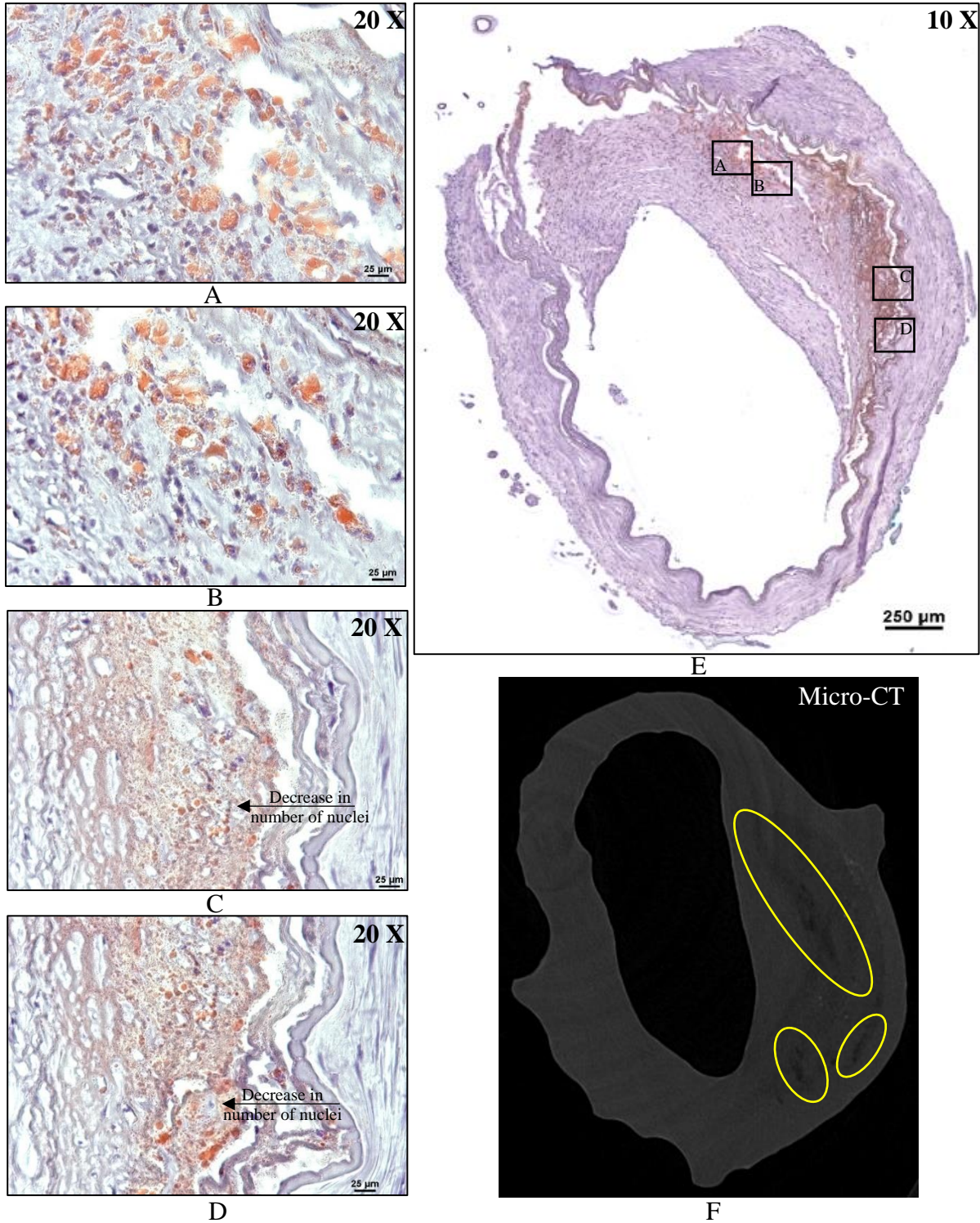


**Figure 16** Oil Red O staining of control cerebral artery. Subfigures A, B, C, and D are 20X zoom-in images at the black squares from subfigure E. Subfigure F is a micro-CT image taken near the depth of the associated histology slice, in which lipid appears at low grayscale level, circled in yellow.

## 3.2 ANALYSIS OF ANEURYSM SAMPLE: UIC 011

### 3.2.1 Morphology of UIC 011

The dissecting microscopy image in Figure 17A illustrates the post-fixed appearance of UIC 011 before it was processed further for imaging. The black square indicates the particular region that was scanned with MPM after immersing with OsteoSense EX 680 to identify presence of calcification. Figure 17C and Figure 17D show the micro-CT images of the same tissue from both the luminal and abluminal side. There is a difference in the morphology between post-fixed, Figure 17A, and when the tissue was being imaged by MPM, Figure 17C. This is the case because the tissue was flattened when mounted in the tissue chamber used for MPM imaging as already noted in 2.7.4 in Chapter 2.

From the 3D reconstructions of the micro-CT data, the surface of UIC 011 could be seen to have rough texture with folds, Figure 17 A and Figure 17D. As a result, when imaging these spots under the MPM, they appear as empty cavities. Figure 17D shows the wall thickness map from the abluminal side. The walls of UIC 011 are exceptionally thin, where the majority of the sample is roughly 35 microns thick. Our current method of cryosectioning was not well suited for these tissues, as the sections would peel off immediately when immersed into liquid during further processing.

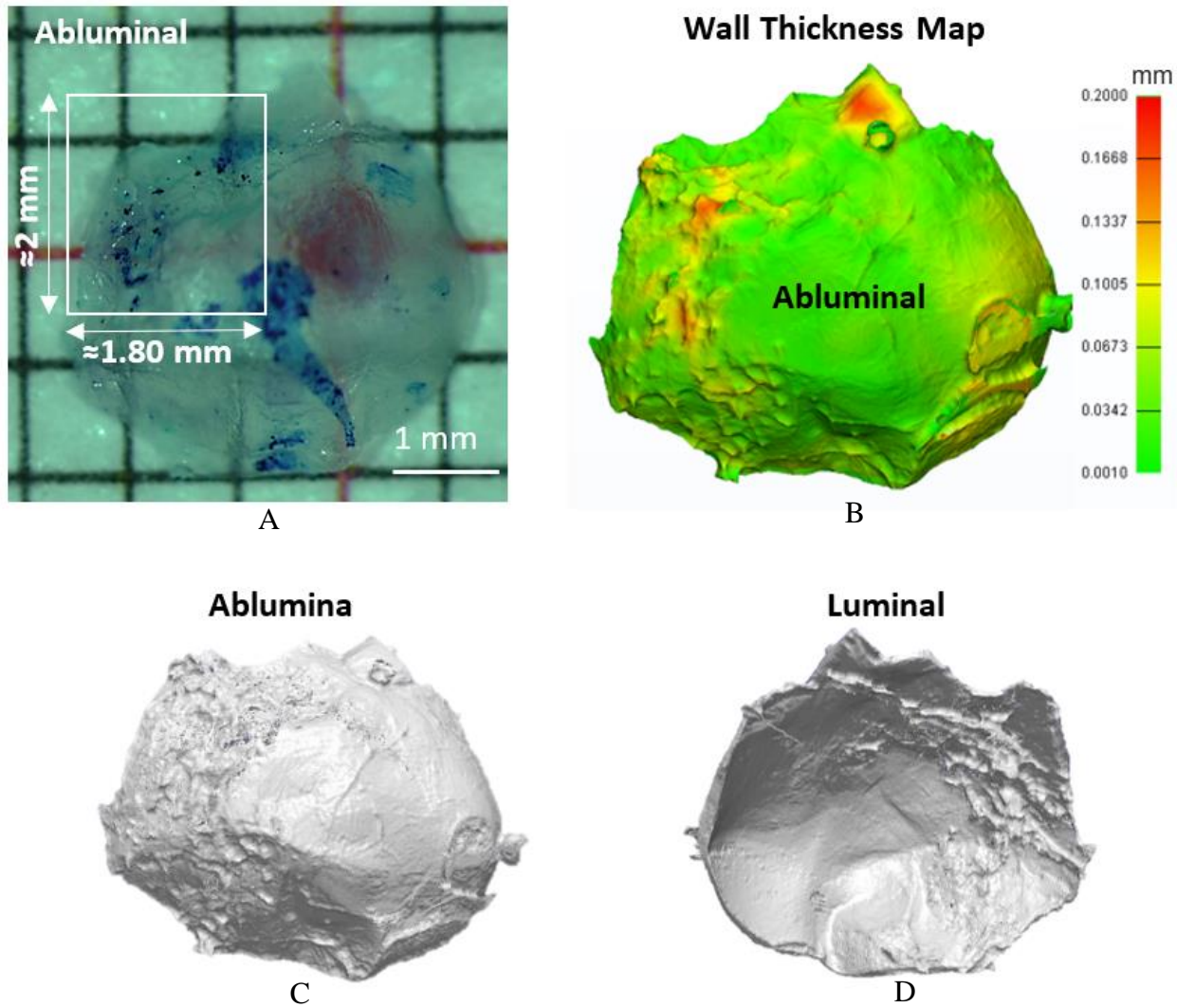


**Figure 17** UIC 011 Appearance. Subfigure A is the post-fixed image of UIC 011. Subfigure B elaborates on the wall thickness of the entire sample. Subfigures C and D are screen-shots of micro-CT images from the abluminal and luminal side

### 3.2.2 Imaging calcification and collagen fibers in UIC 011 under Multiphoton Microscopy

The results of using OsteoSense to image calcification in sample UIC 011 under multiphoton microscopy are shown in Figure 18 and Figure 19. It should be recalled that UIC 011 was our initial sample used for this protocol development and improvements were made in the protocol for

AGH 091. Figure 18A and Figure 19A are projected stacks of 500-micron by 500-micron MPM images stitched together and generated using ImageJ. The step size between each scan was 1 micron, with imaging performed sequentially from the deepest visible region in the tissue up to the abluminal surface. Figure 18A illustrates signal from OsteoSense EX 680 in magenta, indicating calcification, and Figure 19A portrays collagen fibers in red, which are detectable without additional labeling under the MPM. The same colors apply to the subsequent Imaris results from Figure 20 to Figure 21. Micro-CT and dissection scope image, previously shown are reproduced here in Figure 18B and Figure 18C to clarify the location of the MPM images in the tissue. Figure 19B provides the calcification distribution of the full sample.

Stacks denoted as a and b in the combined images in Figure 18 and Figure 19 were selected as examples for 3D reconstruction with Imaris, Figure 20 and Figure 21. The four corners are labeled in counterclockwise order, corresponding with the positions obtained at different orientations. In Figure 20 and Figure 21, subfigure A is the 3D reconstructed images from the collagen signal, and subfigure B shows the combined 3D reconstructed images formed from the calcification and collagen signal.

From observation, UIC 011 did not seem to have been adequately stained by OsteoSense 680 EX (Perkin Elmer, MA, USA). One probable cause is likely due to a larger spread of calcification, when compared with other tissues, such as AGH 091, which will be discussed in Section 3.3. UIC 011 was used as the first attempt in testing the OsteoSense 680 EX (Perkin Elmer, MA, USA) protocol, and based on these results, we increased the immersing time for the second aneurysm sample, AGH 091 from 48 to 56 hours.

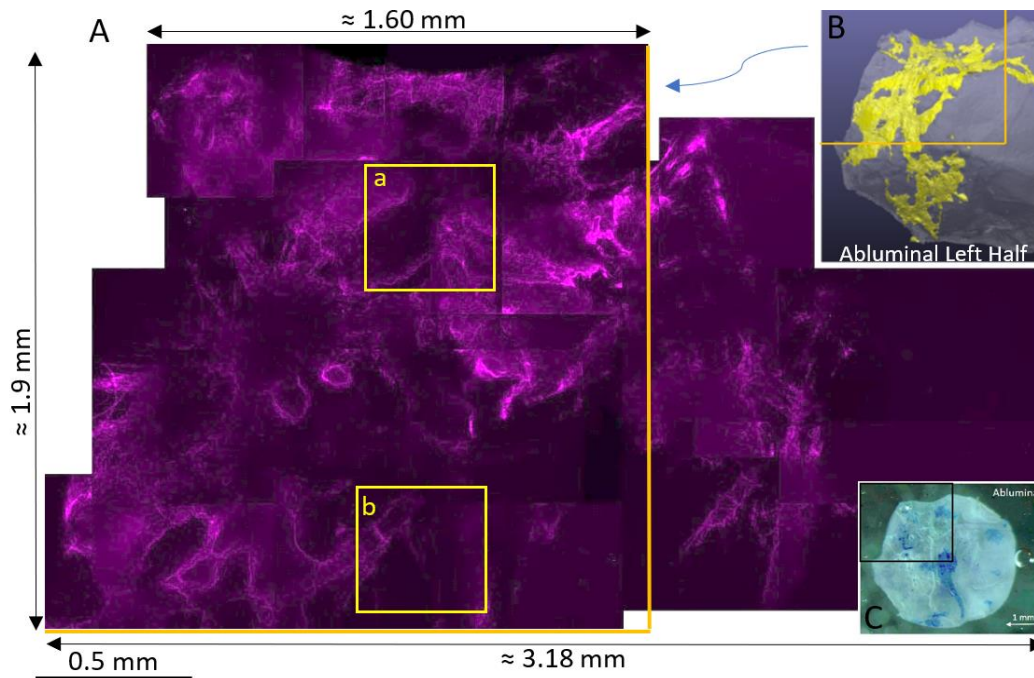


**Figure 18** UIC 011 MPM Imaging. Subfigure A shows the montage of MPM images from the calcification channel. Subfigure B and C are reproduced from Figure 5 to clarify the calcification region.

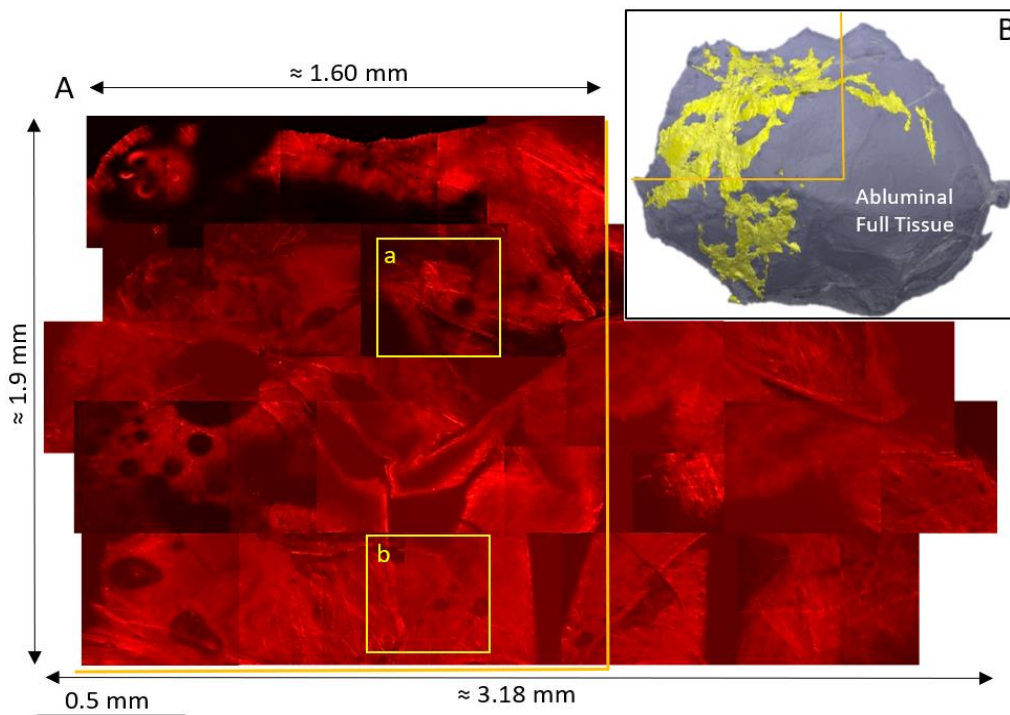


**Figure 19** UIC 011 MPM Imaging. Subfigure A shows the montage of MPM images from the collagen channel. Subfigure B is reproduced from Figure 5 to illustrate the imaged region, as boxed in orange.

At location a, illustrated in details by Figure 20A and Figure 20B, a total of 50 slices, at one-micron step size, were taken and imaged, corresponding a total thickness of 50 microns in the z direction. A large aggregation of calcification was found, for example in the fourth corner, Figure 20B. However, it also appears that part of the calcification body, circle in yellow, was missing. When zooming in closer, it seems that only the boundary of the calcified region has been stained as we can see a stronger fluorescence signal emitted at the periphery. In addition, when observing corner 1 in Figure 20B, collagen fibers appear to go around rather than into the aggregated calcification, as traced out by the white curve.

At location b, shown in details by Figure 21A and Figure 21B, a total of 80 one-micron thick slices were imaged, corresponding to z-direction thickness of 80 microns for the 3D Imaris results, Figure 21A, and Figure 21B. As for the results in location a, the calcification region, circled in yellow at corner 4 in Figure 21B, did not seem to have been fully labeled by OsteoSense. We can see a hollow unstained region in the middle that was likely part of the aggregation. As for collagen fibers in region a, the fibers in region b appear to go around the region of calcification, as traced out by the white curve in corner 1 and 4, Figure 21B.

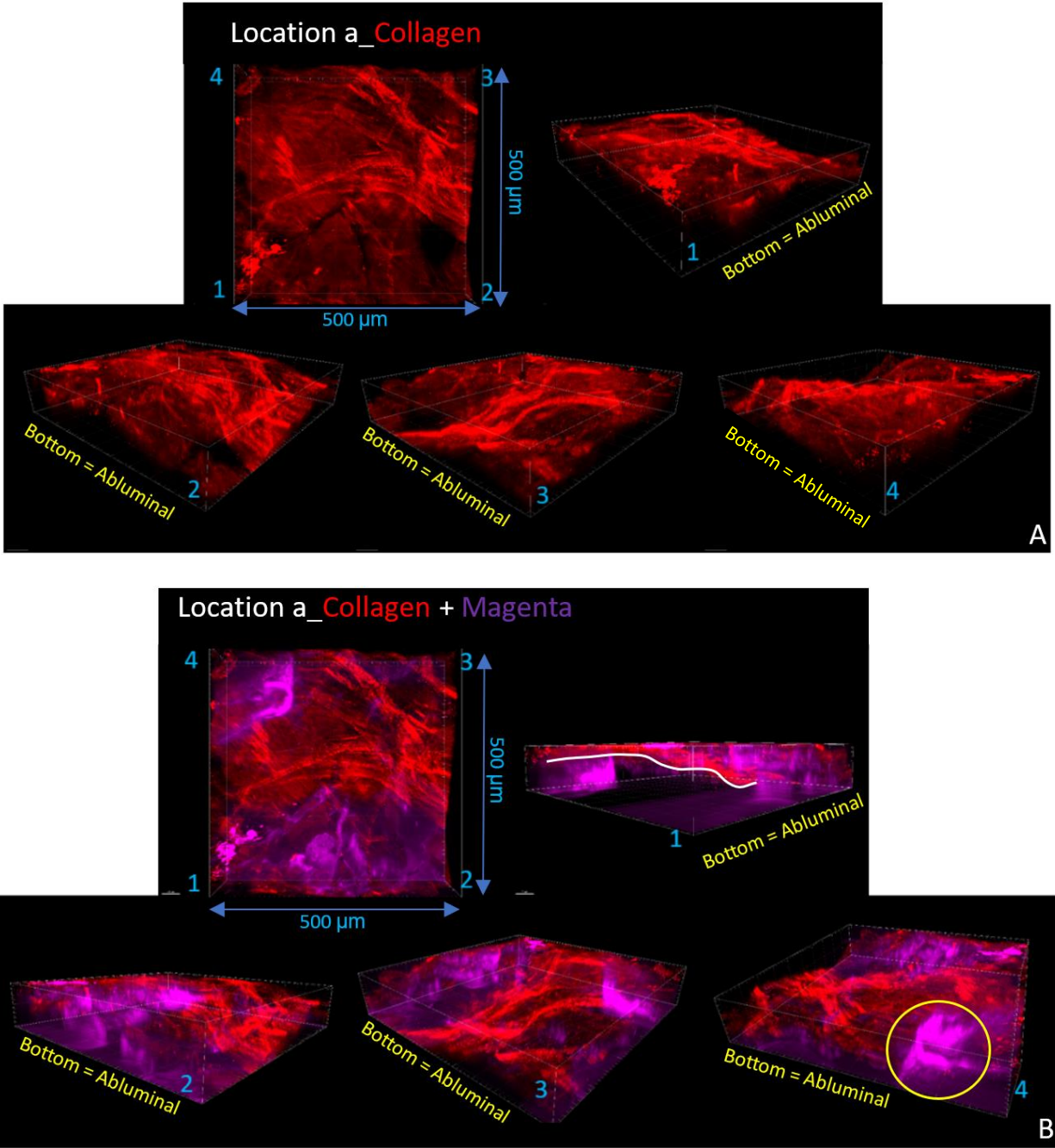


**Figure 20** UIC 011 3D Imaris reconstruction for location a. Subfigure A and Subfigure B are the 3D reconstructed images from the collagen and Cy5 channel of MPM respectively.

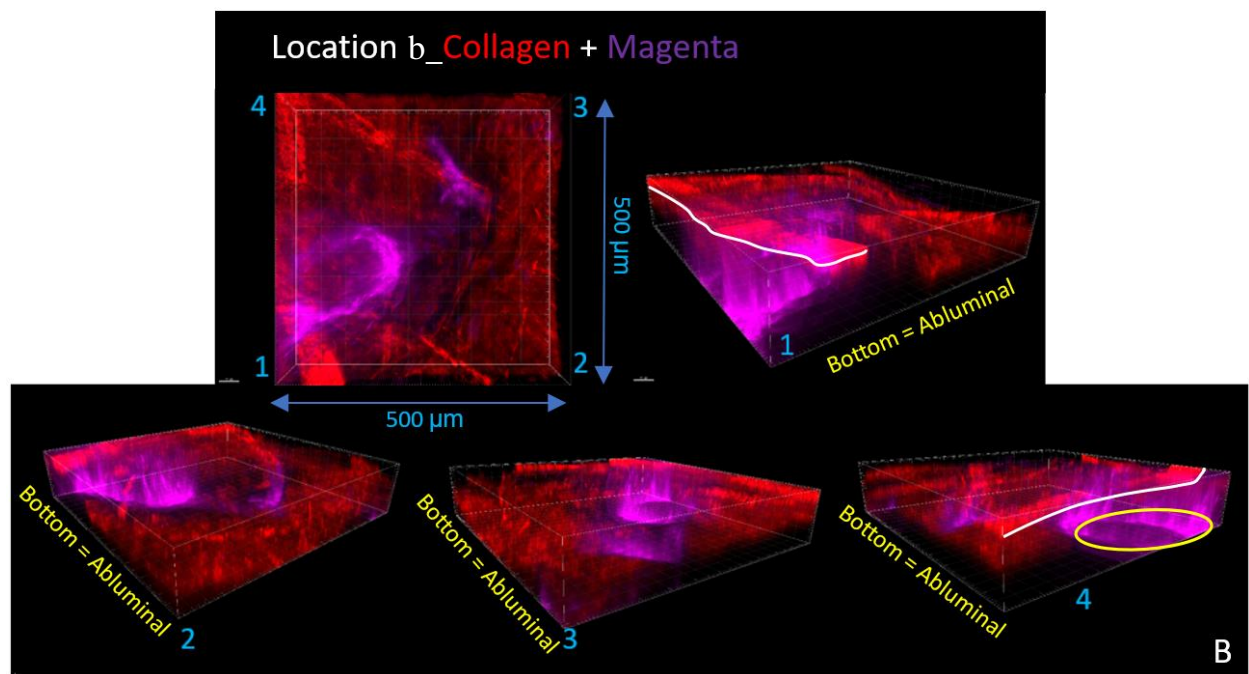
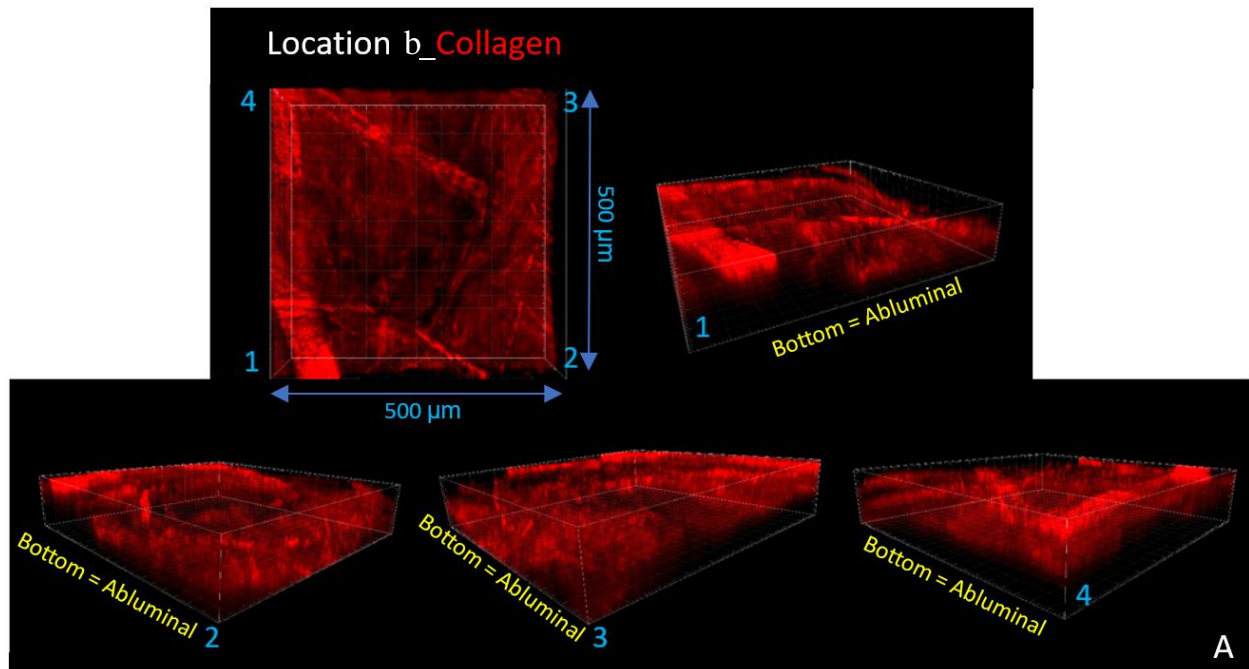


**Figure 21** UIC 011 Imaris reconstruction for location b. Subfigure A and Subfigure B are the 3D reconstructed images from the collagen and Cy5 channel of MPM respectively.

### **3.3 ANALYSIS OF ANEURYSM SAMPLE: AGH 091**

#### **3.3.1 Morphology of AGH 091**

Figure 22A shows the post-fixed image of AGH 091 taken with a dissecting microscope, where the size of each grid in the background is 1 mm by 1 mm. Figure 22B and Figure 22C are 3D images reconstructed from micro-CT scan, and illustrate the morphological appearance of the tissue from the abluminal and luminal side. It is noticeable that while the surface on the abluminal side is relatively smooth, the luminal surface is rough and wrinkly. Additionally, part of the tissue is folded, as circled from the luminal view in Figure 22C and Figure 22E, which also explains the shape as displayed in the cryosectioned slices stained with histology from Figure 28 through Figure 31. As mentioned in the mapping section, 2.7.2.2 from Chapter 2, the top left region enclosed by a black rectangle in Figure 22A was imaged using MPM after the tissue had been immersed in OsteoSense 680 EX (Perkin Elmer, MA, USA) for 56 hours. The width and height of the scanned region are displayed in red, using the grid's size as reference in Figure 22A. Wall thickness maps are also included here in Figure 22D and Figure 22E.

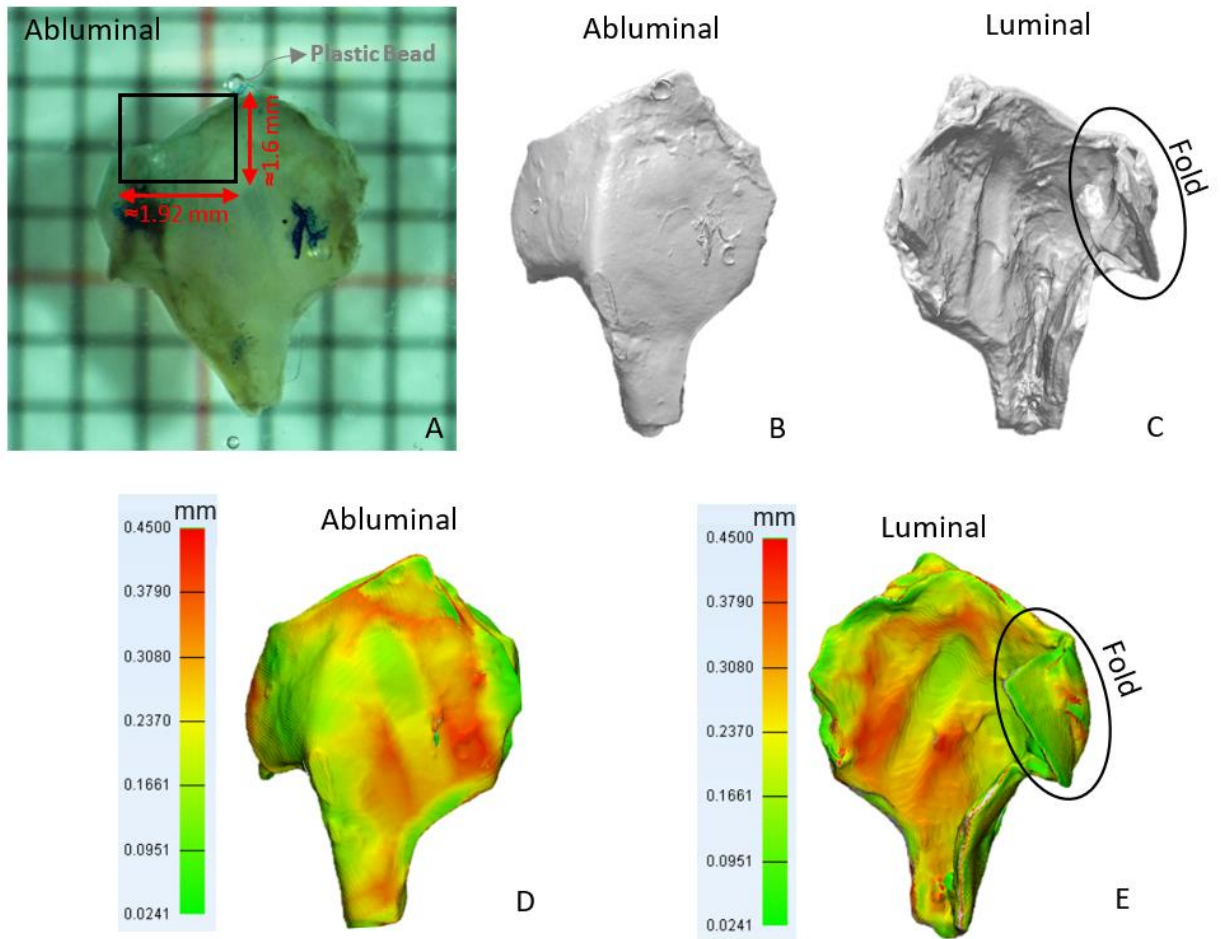
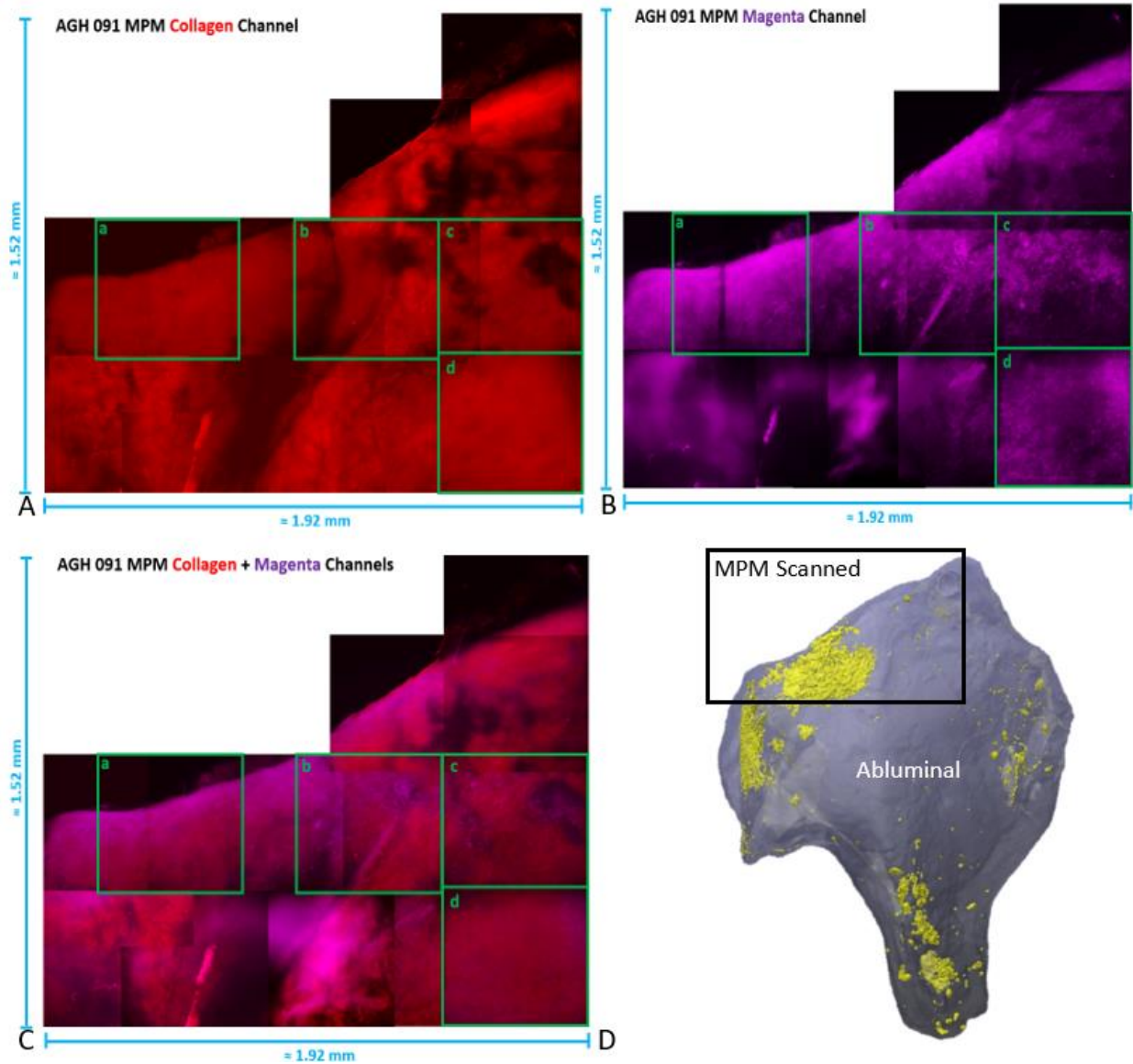


**Figure 22** AGH 091 Appearance. Subfigure A is the post-fixed image of AGH 091. Subfigure B and C are screen-shots of micro-CT images from the abluminal and luminal side. Subfigure D and E elaborate on the wall thickness of the entire sample from the abluminal and luminal views.

### **3.3.2 Imaging calcification and collagen fibers in AGH 091 under Multiphoton Microscopy**

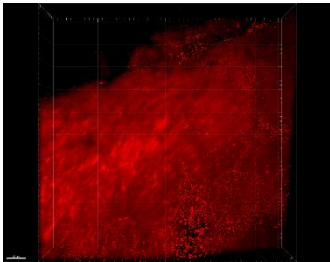
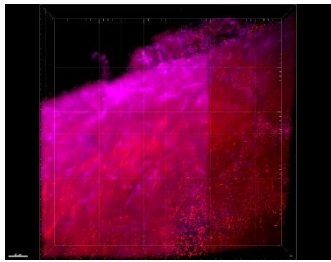
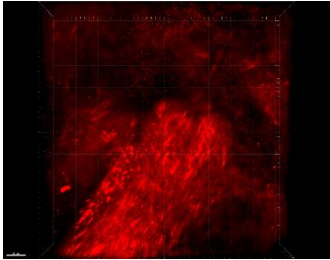
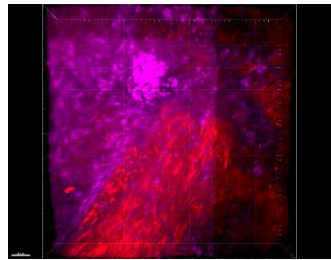
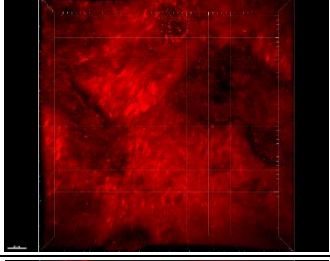
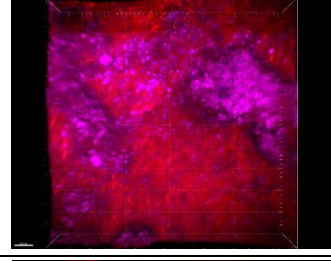
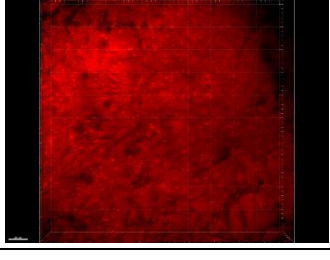
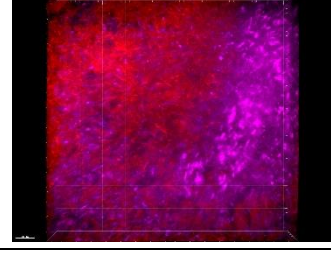
Figure 23 below was created as described for UIC 011, Section 3.2.2. The only difference was that MPM images on this sample were scanned at a slice thickness of 2 micron per scan. On average, roughly 50 scans were taken in one stack, corresponding with an overall height in z of 100 microns for the 3D reconstructed Imaris pictures from Figure 25 through Figure 27. Figure 23A and Figure 23B are the projected 2D images of the scanned region in collagen and calcification separately. Stitched images from collagen and calcification signal were merged, Figure 23C, to illustrate if these two signals overlap or fill each other's gaps. Figure 23D is a micro-CT image reproduced here as a reference to find the calcified region, labeled in yellow.

On the abluminal side, four locations, labeled as a, b, c, and d from Figure 23 were reconstructed with Imaris. 2D results for each them are tabulated below in Table 4 respectively. Additionally, several zoom-in views were imaged at certain places, among which three were selected as representatives to categorize the relationship found between the distribution of collagen and calcification. Further details will be discussed in Section 3.3.3. From observation, calcification can be ranked in terms of the aggregation patterns in these chosen regions. One common trait shared between them is that calcification appears to fill, or overlap with, loose collagen areas.



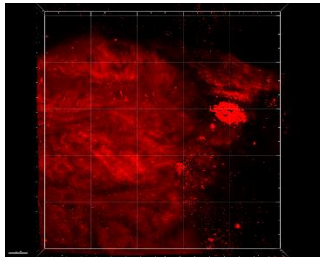
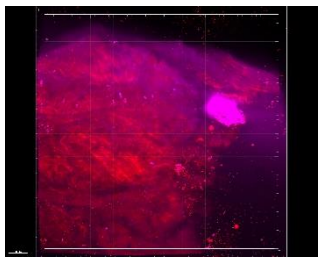
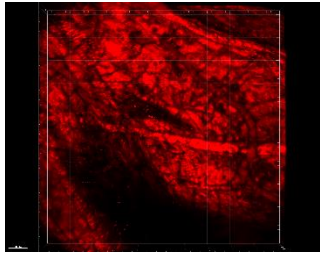
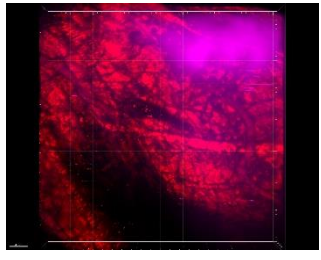
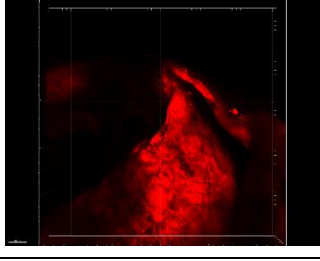
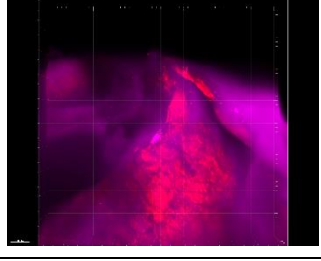
**Figure 23** AGH 091 MPM Imaging of collagen and calcification. Subfigure A and B are the montage of 2D projected MPM images captured from the collagen and calcification signal in MPM. Subfigure C merges the 2D projected images from calcification and collagen altogether. Subfigure D is reproduced from Figure 6B to clarify the physical morphology of AGH 091, as well as the calcification region.

**Table 4** AGH 091 Abluminal locations selected from 3D reconstruction (2D projections)

Locations	Collagen	Collagen + Calcification
Abluminal <b>a</b>		
Abluminal <b>b</b>		
Abluminal <b>c</b>		
Abluminal <b>d</b>		

The luminal side was also scanned with MPM to illuminate whether the presence of calcification also exists on the other side of the wall. Only three places were imaged on this side and reconstructed with Imaris, as shown in Table 5 and Figure 24. In order to avoid confusion with the abluminal side, no dye marker was made on this side of the tissue. Instead, for convenience, the three locations were selected by using the bead and the tissue's morphological characteristic at the bottom right plateau corner as reference.

**Table 5** luminal locations selected for 3D reconstruction (2D projections)

Locations	Collagen	Collagen + Calcification
luminal <b>a</b>		
luminal <b>b</b>		
luminal <b>c</b>		

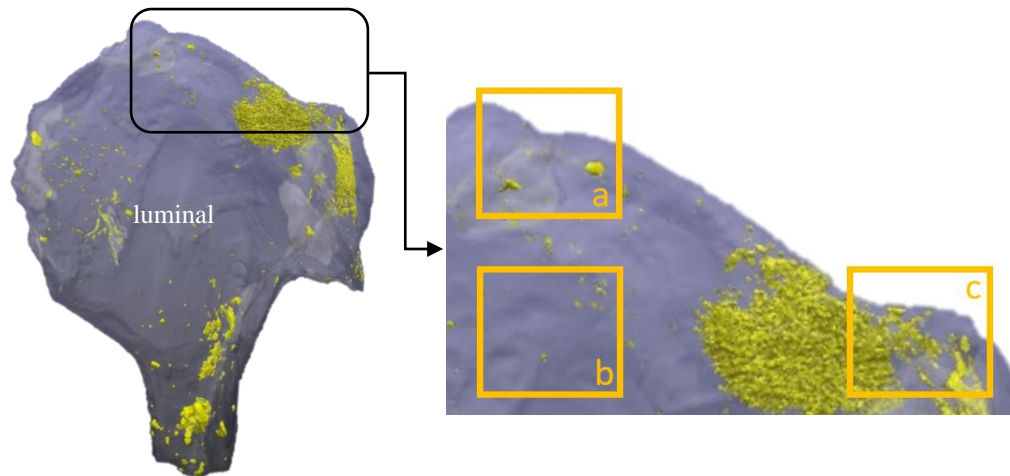


**Figure 24** AGH 091 Imaging from the luminal side. Squares labeled with a, b and c are the locations imaged under MPM from the luminal side

### 3.3.3 Categories of relationships between collagen and calcification

Figure 25 through Figure 27 contain a series of images reconstructed with Imaris for location **b**, **c**, and **d** emphasized in Figure 23. Specifically, subfigure A provides visual information about the pattern of collagen fibers. Subfigure B shows the overlap of two MPM channels, collagen in red, and calcification in magenta. Subfigure C is one selected zoom-in view of the focused area circled in yellow from subfigure B. In every subfigure, four corner are labeled in a counterclockwise order, corresponding with the views numbered accordingly at different orientations.

The categories are established based on two criteria, one concerning the size of empty pockets found between collagen fibers, and the other concerning the shape and aggregation pattern of calcification filling these pockets. They are used as a scale in ranking these categories. Table 6 summarizes the findings from Figure 25 through Figure 27.

**Table 6** Summary of relationship categories

	Category I	Category II	Category III
Collagen	Small disperse cavities	Aggregated small cavities	Greater than 50 microns in diameter
Calcification	Disperse particles	Mix of disperse particles and aggregation with non-convex shape	Amorphous aggregation forming a continent

### **Category I: Small pocket with disperse calcification particles**

Viewing from orientation 1 in Figure 25, we observe that calcification and collagen region appear to divide the captured view and occupy each half individually, as traced out by a white curve in Figure 25B. To start from the smallest rank on the scale, we focus on the zoomed-in area, as shown in Figure 25C, where the collagen gaps are approximately 10 microns wide on average and separated from one another. Calcification can be seen here as distinctive dots dispersed among collagen fibers. When rotated to 3D views, we can identify these individual dots with well defined shapes. In particular, they have enclosed volumes close to ellipsoids, and the largest measurable particle size is roughly 3 to 5 microns in diameter, measured using ImageJ. Collagen fibers behave in a way such that they do not penetrate through these particles, but rather localize around them. While these particles do not seem to concentrate at any particular point, they tend to aggregate towards corner 3 in Figure 25C, where the magenta color increases in signal, indicating that this location is close to the neighborhood with larger aggregated calcification region that borders with collagen fibers on the other side.

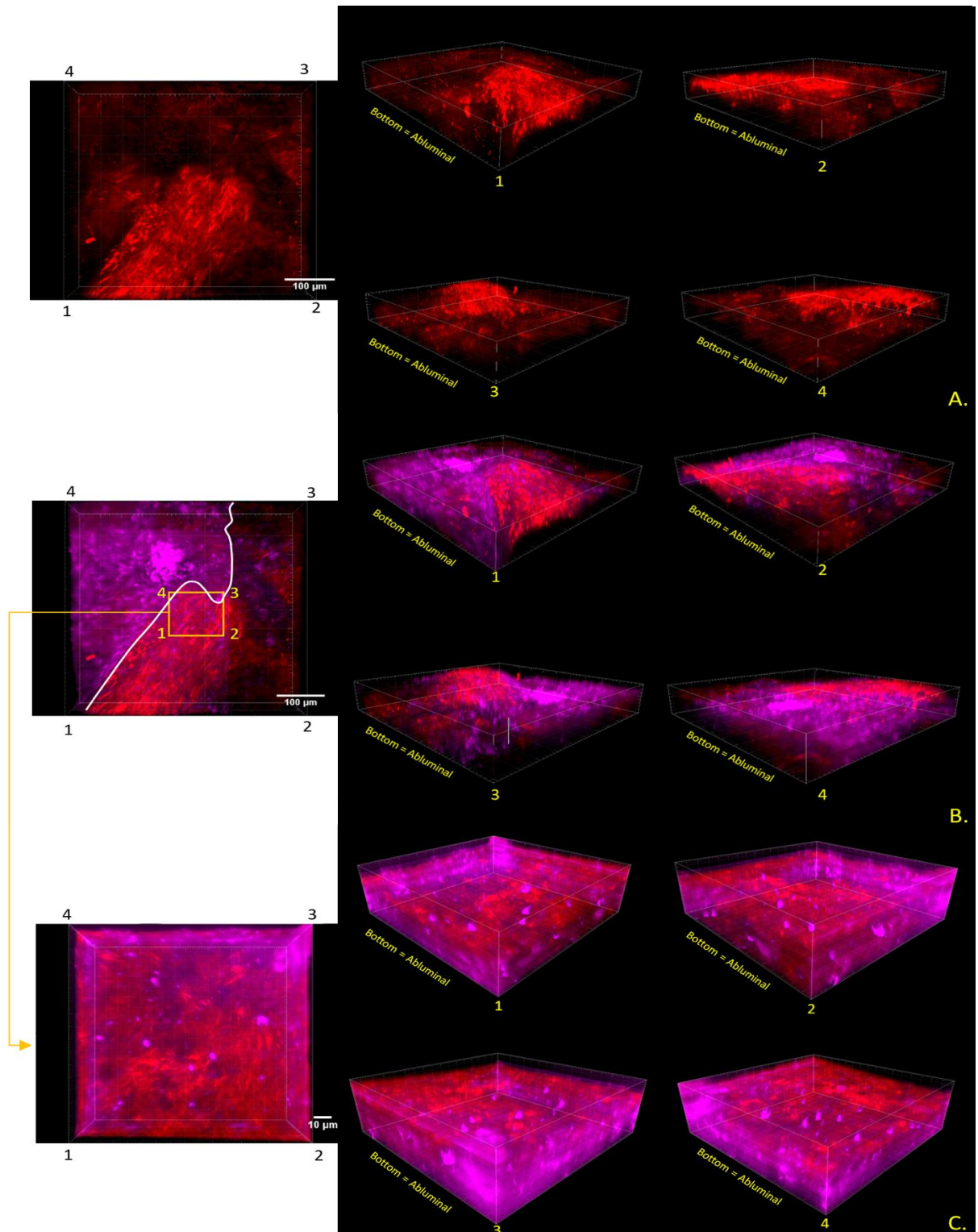


**Figure 25** Relationship category I between collagen and calcification. Subfigure A and subfigure B were 3D reconstructed images from Imaris, illustrating the collagen and calcification signal separately. Subfigure C merges these two channels.

## **Category II: Medium pocket with aggregated calcification in non-convex shape**

The primary standard used for this category is the medium size collagen pocket, as shown by the zoom-in view in Figure 26C. Circled in blue are a number of empty holes that are almost connected altogether to form a larger void between collagen. These holes are filled with disintegrated-like collagen debris, in combination with calcification both in the disperse and aggregated forms. Furthermore, as shown in Figure 26B, we also find a pattern where collagen and calcification localize near each other with borders between them. When comparing the distribution of collagen with calcification, we again observe that calcified region fills up the empty spaces that were not found in the collagen channel. At areas where they overlap, from zooming in and rotating to 3D view, collagen appears to be around the calcification.

From corner 1 of the zoom-in view, Figure 26B, there is a good abundance of small-sized calcification particles with concrete ellipsoid shape near the aggregations. It is likely that the aggregation started originally from these smaller ones, and eventually expand into an individual standalone region.

Besides the small disperse particles, in Figure 26C, aggregated calcification are present as arbitrary non-convex shapes, such as those circled in white. On average, the measurable aggregation size via ImageJ is roughly 8 microns in diameter. Another noticeable characteristic is a decrease of collagen signal near such aggregation, but the signal is still visually distinguishable from the magenta background

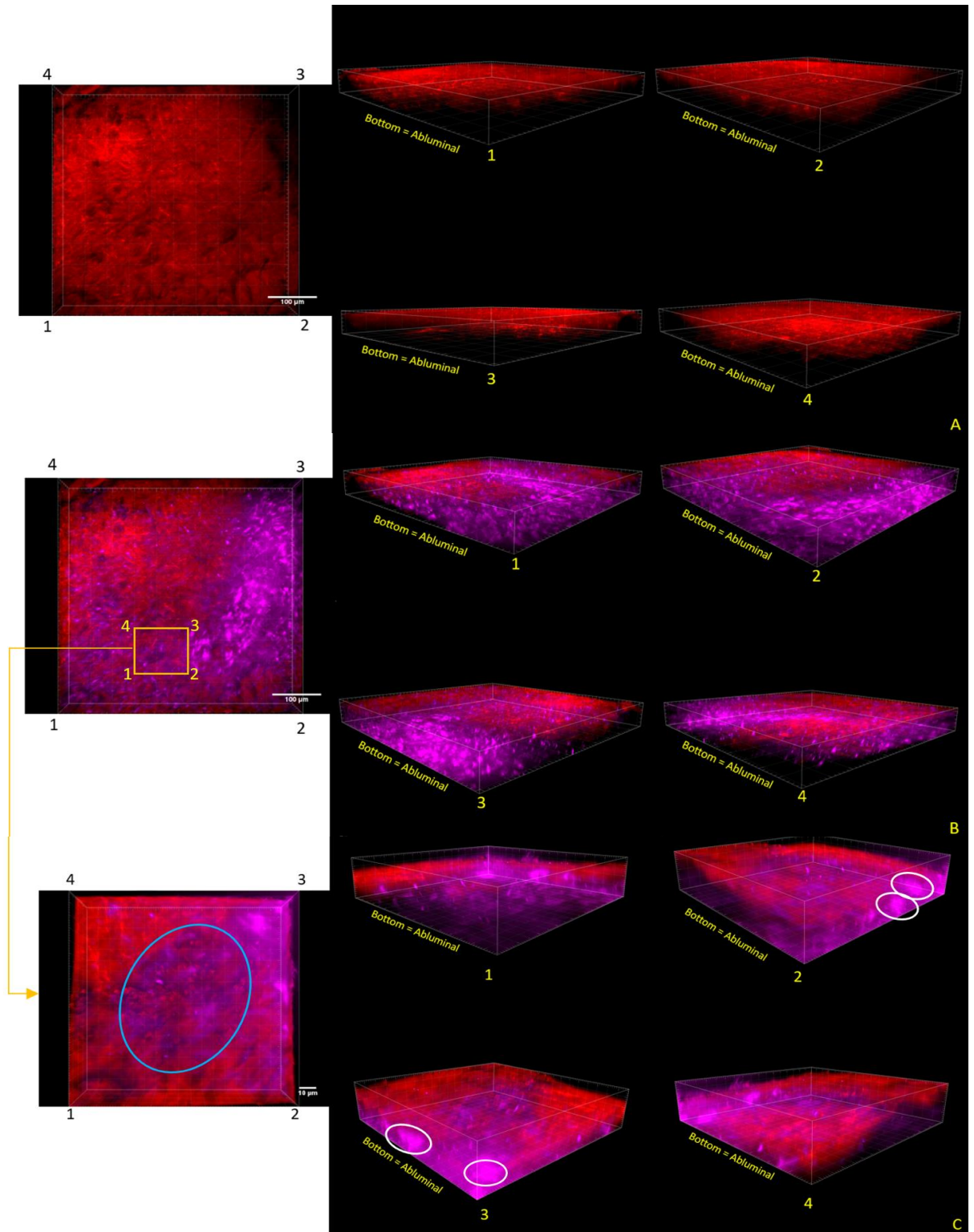


**Figure 26** Relationship category II between collagen and calcification. Subfigure A and subfigure B were 3D reconstructed images from Imaris, illustrating the collagen and calcification signal separately. Subfigure C merges these two channels.

### **Category III: Large collagen pocket with amorphous aggregation of calcification**

Similar to all other locations described earlier, in Figure 27, calcification and collagen occupy individual regions and border one another with defined boundaries around them, as shown by various orientations in the Figure 27B. Also from this subfigure, collagen fibers appear to be routed around the calcified region rather than direct penetration.

From observation, the selected zoomed-in location in Figure 27C, the collagen pocket appears as one large cavity, traced out by the white curve. At this location, we can find the presence of small to medium sized calcification particles as presented in the first two categories, and also a much larger calcification aggregation that starts to appear as amorphous bundles undisrupted by other signals. For example, the bundle size, circled in white, is roughly 15 microns in diameter when measured via ImageJ. There is a sign that this bundle continues its linkage with other segments that were not captured in this frame. This is likely the case because when viewing from corner 2 in Figure 27C, the structure seems to have been cut off by the frame edge. Additionally, there is one entire continuous calcification region neighboring this corner.

Almost no collagen fibers can be visually detected and distinguished from the background near large aggregation of calcification in this category. Collagen fibers appear to distribute themselves either at region without positive calcification stain, or at region with small to medium sized calcification spots.

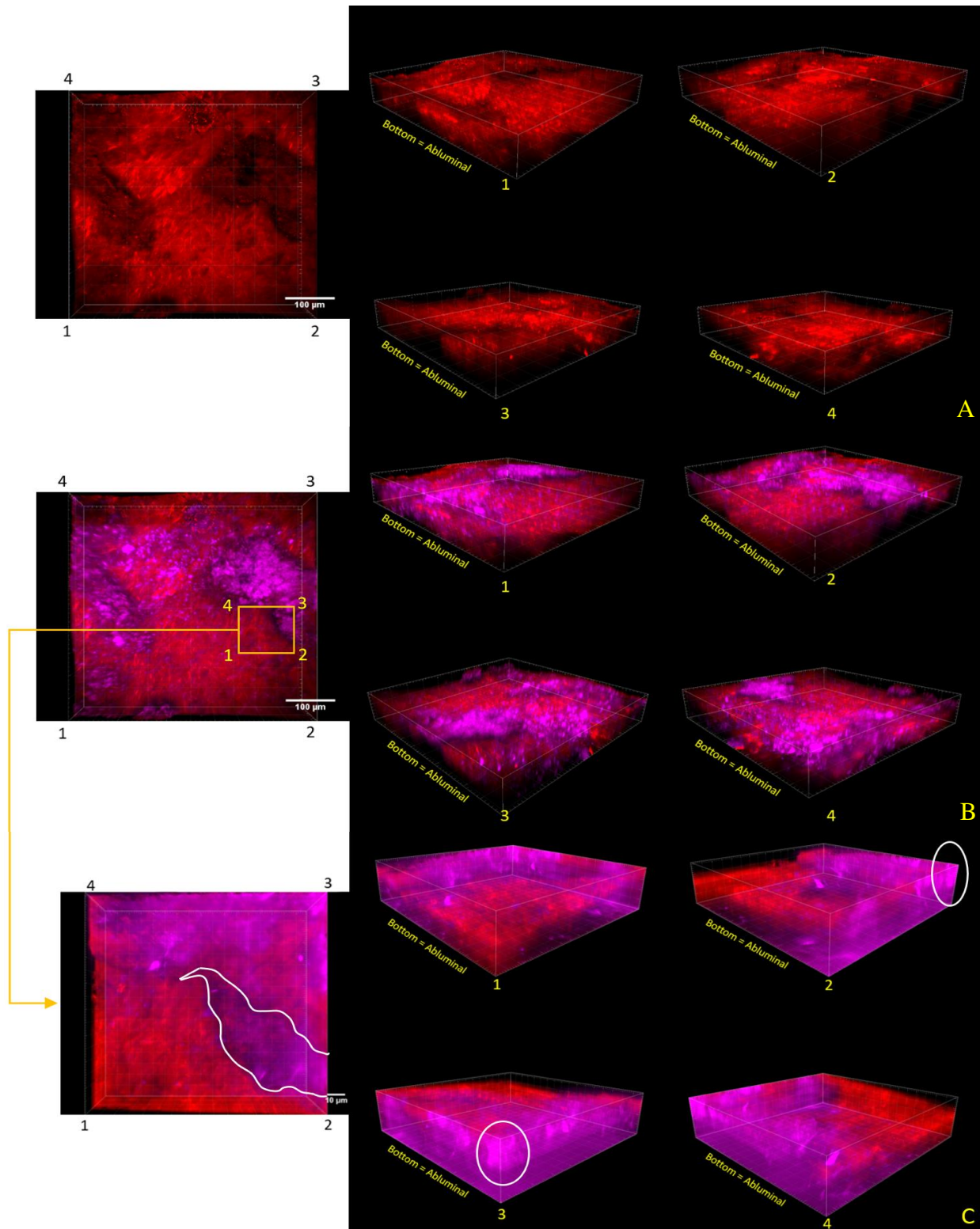


**Figure 27** Category III between collagen and calcification. Subfigure A and subfigure B were 3D reconstructed images from Imaris, illustrating the collagen and calcification signal separately. Subfigure C merges these two channels.

### 3.3.4 Histology

Tissue sections were made via cryosectioning and stained with H&E, Alizarin Red, von Kossa, and Oil Red O respectively to examine, and verify cell presence, calcification and lipid regions within the MPM image. A total of 56 slices were made, and classified into three groups, namely top, middle, and bottom of the region. They were mapped with micro-CT images according to the depth information acquired from cryosectioning, and also by morphological landmarks. 2D micro-CT images illustrate lipid as low greyscale value, close to black in color, and calcification as high value close to white. Because a lot of manual handling was done during micro-CT scan, and during tissue preparation for histology staining, the tissue's shape would change at different time points. For this reason, morphological comparison between micro-CT images and histology slices is not exact.

Table 7 demonstrates the types of histology information presented. We started first with H&E to identify cell nucleus and cytoplasmic inclusions. Areas without cell nuclei are likely to be occupied with various substances, such as lipid and calcification, which are the focus of our interest. Because von Kossa binds specifically to calcium phosphates, the positively stained locations are more limited than the results from Alizarin Red, which stains calcium more generally. For this reason, using Alizarin Red as indicator of calcification in the aneurysm wall would be more efficient.

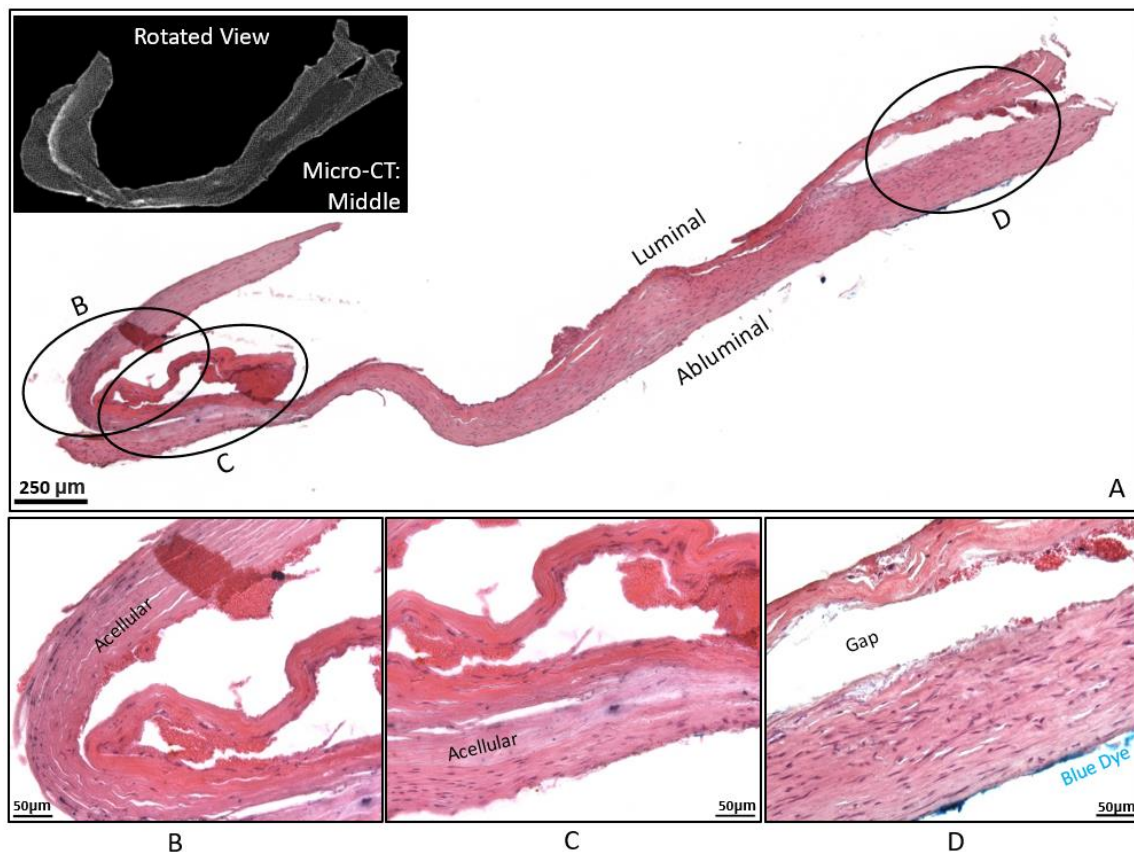
**Table 7** Confirmation of calcification and lipid from physical aneurysm tissue with histology

Histology Information from AGH 091			
	Locations of slices collected for histology (from cryosectioning data)	Locations of slices collected for histology (from micro-CT data)	Histology
Top			Oil Red O, Alizarin Red
Middle			H&E, von Kossa, Oil Red O, Alizarin Red
Bottom			Oil Red O, Alizarin Red

### H&E Staining

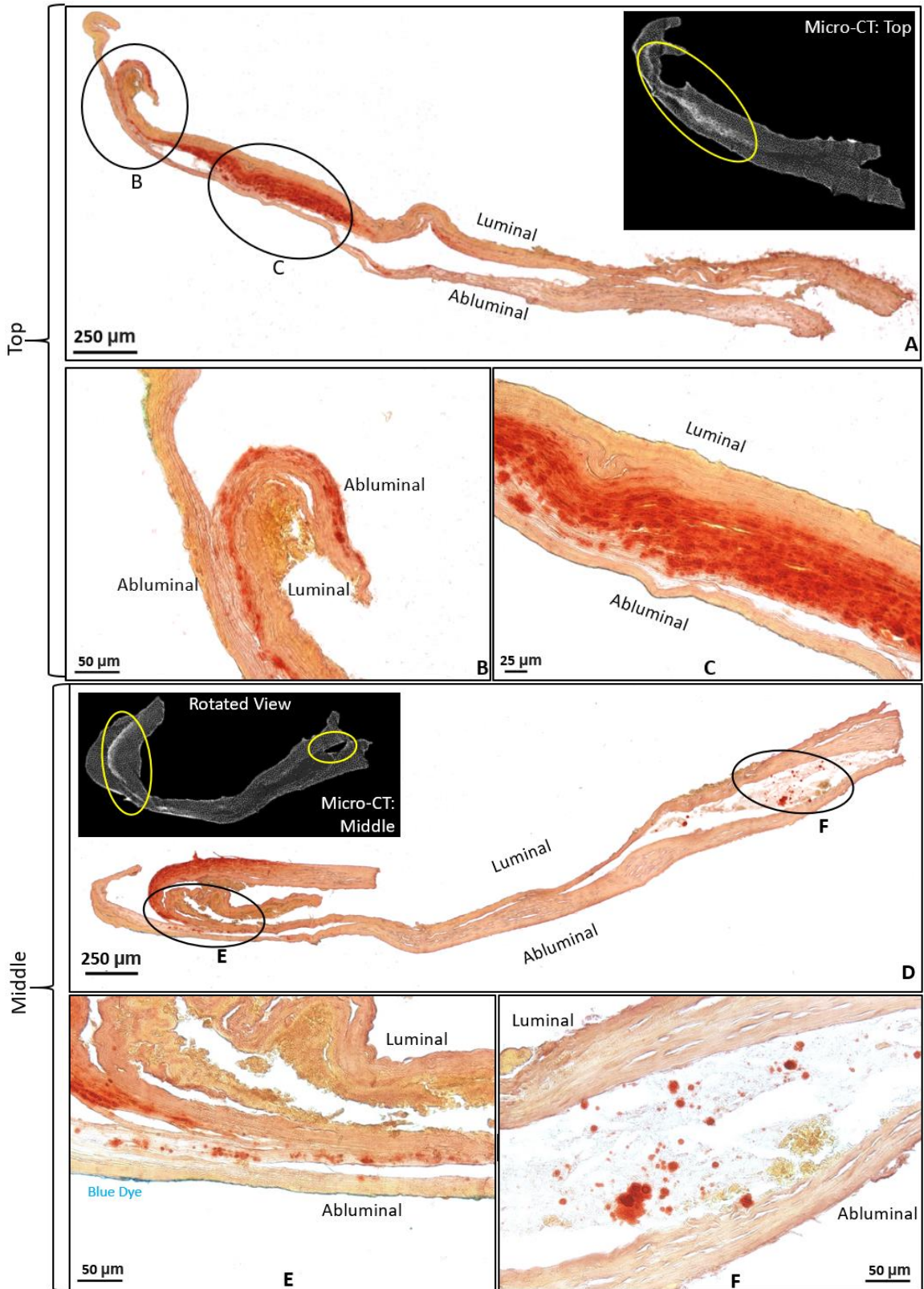
Figure 28A is a H&E stained slice, acquired with 10X magnification using Eclipse Ti-E Nikon microscope, from the middle portion of the MPM scanned region, as illustrated by Table 7. The top left corner of Figure 28A is a micro-CT slice image that has been rotated to match the

orientation of H&E image. Locations A, B and C are 20X zoom-in views that contain either a large gap or acellular areas. Cell nuclei are presented here as deep-blue/purple, and the rest in pink indicating other substances that would require more specific labeling for identification. The light blue strip on the abluminal surface in Figure 28D comes from the blue dye marker previously applied for location reference. It is observable that the gap and acellular areas correspond relatively with the location of lipid, in dark grey, and calcification, in white, from the micro-CT image. From this observation, the formation of the gap is likely due to lipid peeling off from the histology slice during the handling process, for example, at the rinsing step with ethanol. This occurred frequently.



**Figure 28** H&E staining of AGH 091. Subfigure A shows 10X image of a cross-section stained with H&E, as well as a micro-CT image (top left corner) taken near the associated depth. Subfigure B, C, and D are 20X zoom-in images at locations circled in black in subfigure A.

Alizarin Red



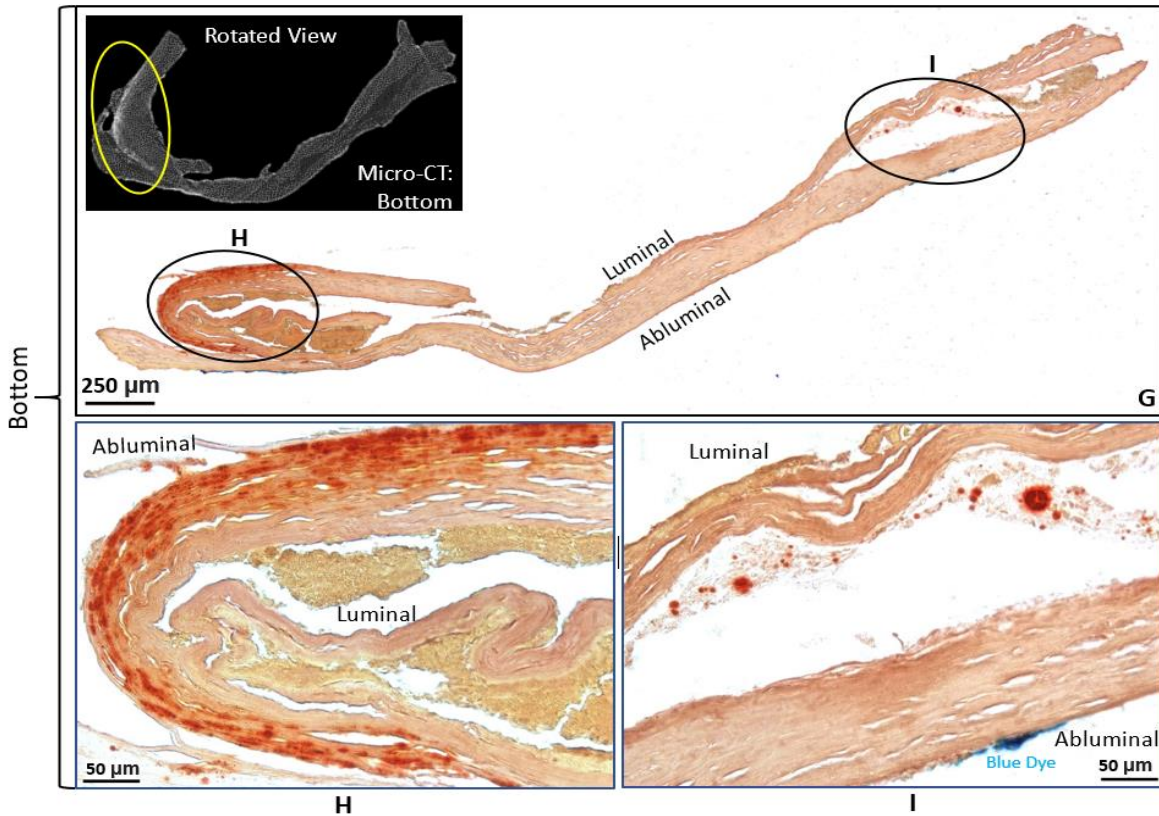
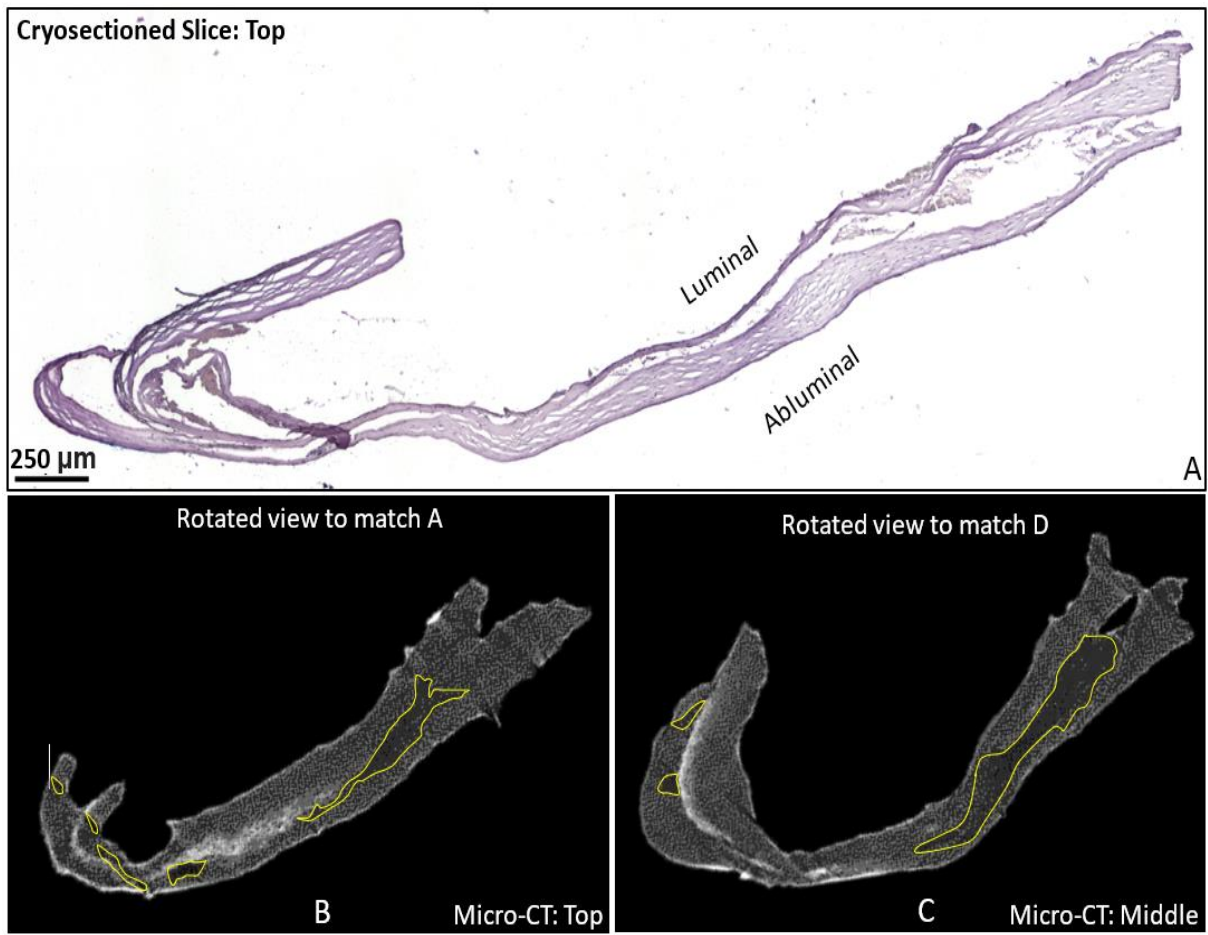


**Figure 29** Alizarin Red staining of AGH 091. Subfigure A, D, and G are 10X images of cross-sections stained with Alizarin Red, as well as a micro-CT image taken near the associated depth. Subfigures B, C, E, F, H, and I are 20X zoom-in pictures from the locations circled in black in subfigures A, D, and G.

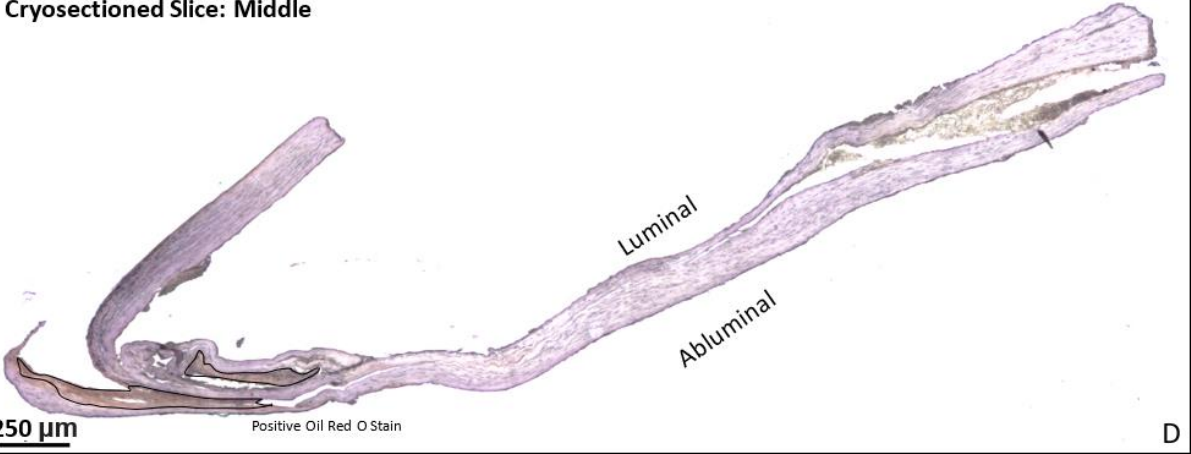
Figure 29 A, D, and G are semi-serial cryosectioned slices stained with Alizarin Red to identify calcification, and the results were captured with 10X magnification using Eclipse Ti-E Nikon microscope. They are arranged in an order from top to bottom, which corresponds with the sequence as illustrated in *Table 7*. Figure 29 B, C, E, F, H, and I are zoom-in views from A, D, and G with 20X magnification. Here, calcification appears as bright red, either as aggregated, or disperse particles. From micro-CT images attached to Figure 29 A, D, and G at each associated depth, calcification aggregates mostly on the left-hand side, displayed as white, and circled in yellow. This distribution can also be found from Alizarin Red stain.

One uniform pattern found between three different depths is that calcification tends to localize more closely to the abluminal side. A thin external layer borders, and slightly overlaps with calcification on the outside, as shown in Figure 29 C and E. In Figure 29 H and B, calcification appears to have travelled even further, occupying this external layer and becoming almost the first immediate contact with the external environment. Although calcification is found to aggregate mostly by the abluminal side, there are a few exceptions, where disperse spots show positive stain with Alizarin Red near lumen on the tissue's right half, as shown in Figure 29 F and I. However, at these areas, large gaps are present within the wall, which might indicate artifacts that took place during the handling process. Therefore, there exists a possibility that positive calcification stains near the luminal side could have originally been from the abluminal side, and become shifted by an external force.

Oil Red O

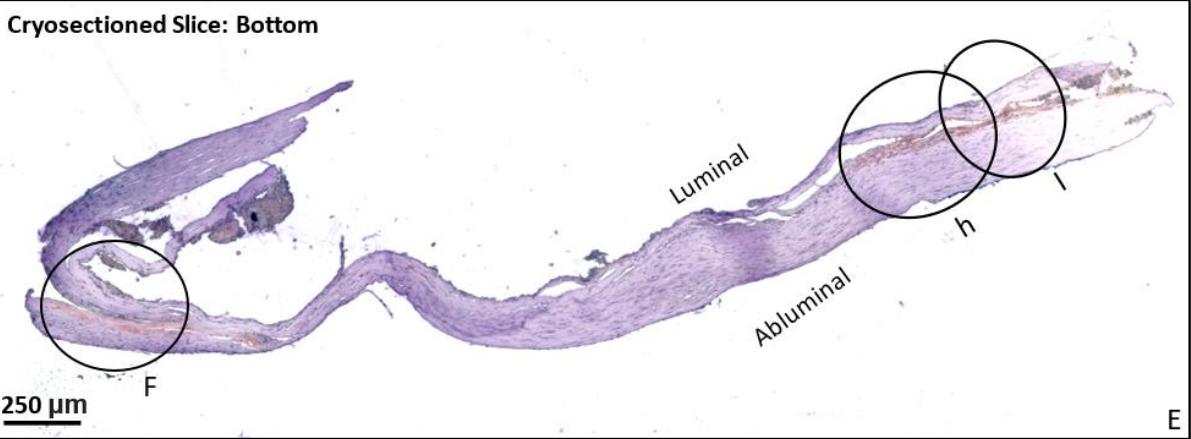


Cryosectioned Slice: Middle

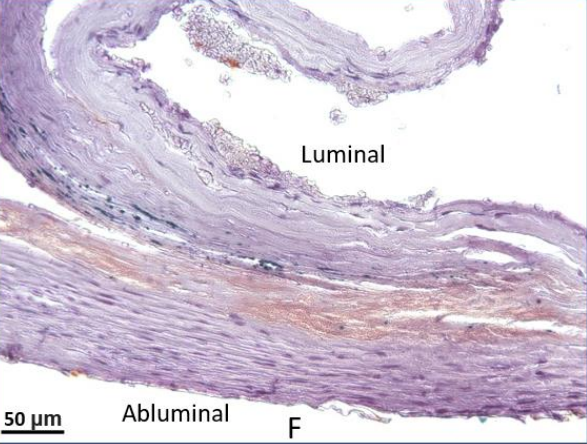


D

Cryosectioned Slice: Bottom



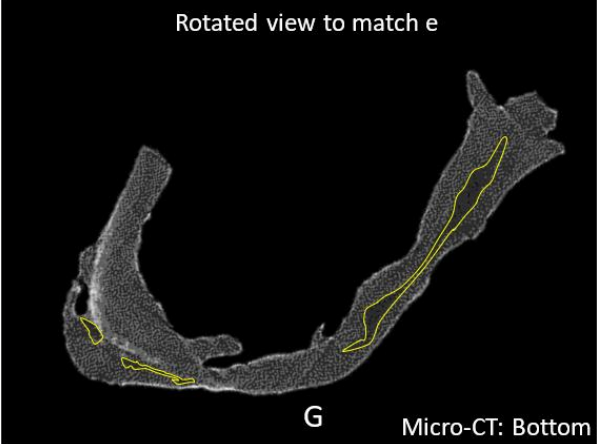
E



Luminal

Abluminal

F



G

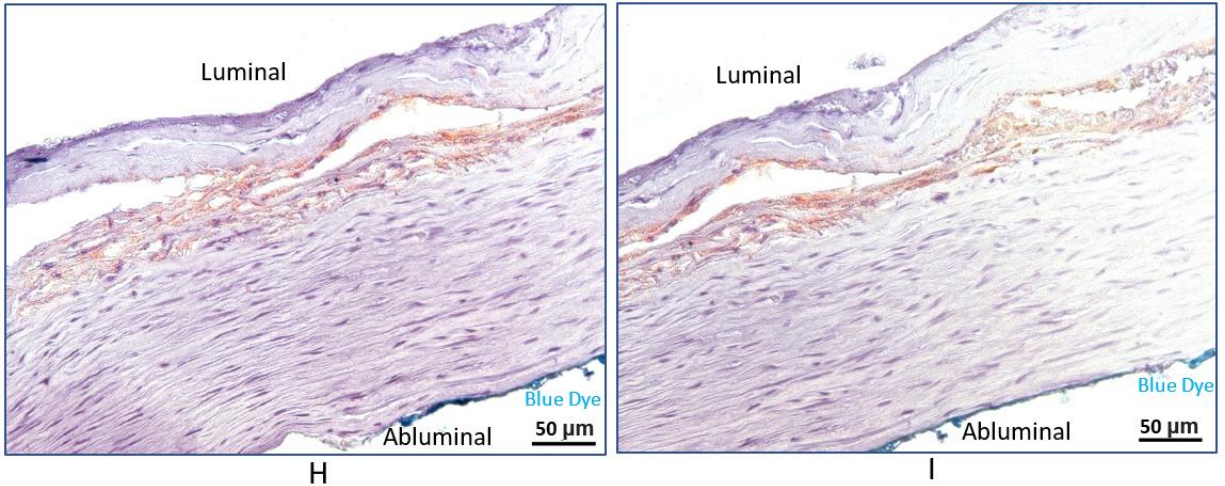


**Figure 30** Oil Red O staining of AGH 091. Subfigures A, D, and E are cross-sections stained with Oil Red O. Subfigures B, C and G are the micro-CT images at the associated depths. Subfigures F, H and I are 20X zoom-in pictures from locations labeled accordingly in subfigure E

Figure 30 A, D, and E are semi-serial cryosectioned slices arranged in the order from top to bottom, as in the sequence illustrated by *Table 7*, and stained with Oil Red O to identify the presence of lipid. The results were captured with 10X magnification using Eclipse Ti-E Nikon microscope. Figure 30 B, C, and G are the micro-CT images at each associated depth, where the enclosed regions in yellow indicate lipid pools. Figure 30 F, H, and I are the 20X zoom-in pictures for a few locations at the bottom slice, which are circled and labeled respectively in Figure 30E.

As stated above from H&E staining, maintaining intact stained lipid pools is difficult because they have strong tendency to be removed during the histology protocol. Figure 30 A is an example, where lipid might have been washed off, leaving behind cavities within the tissue wall. When comparing between Figure 30A with Figure 30B, where the lipid region identified by micro-CT, highlighted with yellow borderline, match with the location of an empty gap in the histology

slice. A similar finding also applies to Figure 30C and Figure 30D. The bottom slice, from Figure 30E is the most successfully stained, and the positive lipid stain locations match with their counterparts in the micro-CT image, Figure 30G. It should be recalled that the micro-CT is done on intact specimens and therefore avoids this artifact. This histological staining is used to validate our findings under micro-CT and provide additional information about the relationship of the location of calcification and lipids with the location of intramural cells and other entities not visible under micro-CT.

One common pattern found here from histology is that lipid pools tend to aggregate towards the luminal side, as shown by the orange/red stain in Figure 30F, H, and I, as well as the left lower half of Figure 30D, traced with black lines. Also, judging from Figure 30F, H, and I, two aggregation types can be seen. Particularly, lipid molecules appear to be either in-between cell nuclei, as shown in Figure 30H and I, or form into a larger acellular pool of its own as shown in Figure 30F. The density of cell nuclei appears to decrease towards the location where lipid is found.

## Von Kossa Staining

Figure 31A is a cryosectioned slice, stained with von Kossa, from the middle region as arranged by Table 7. This image was captured using 10X magnification with the Eclipse Ti-E Nikon microscope. Figure 31B is a 40X zoom-in view, where positively stained calcium phosphates appear as black dots, and the location of which matches with the larger white calcified region as shown by the micro-CT image in Figure 31C. When compared with Alizarin red results, depicted by Figure 29D, the area stained with von Kossa seems to overlap with, and is contained within the Alizarin Red area. This is an expected result, since positive von Kossa stain would be more limited in size due to its more specialized label. Although the Alizarin Red and von Kossa were not performed on the same slices, they were performed on slices originating from the same mid-tissue region that are less than 100 microns apart, based on the recorded cryosectioning depth information.

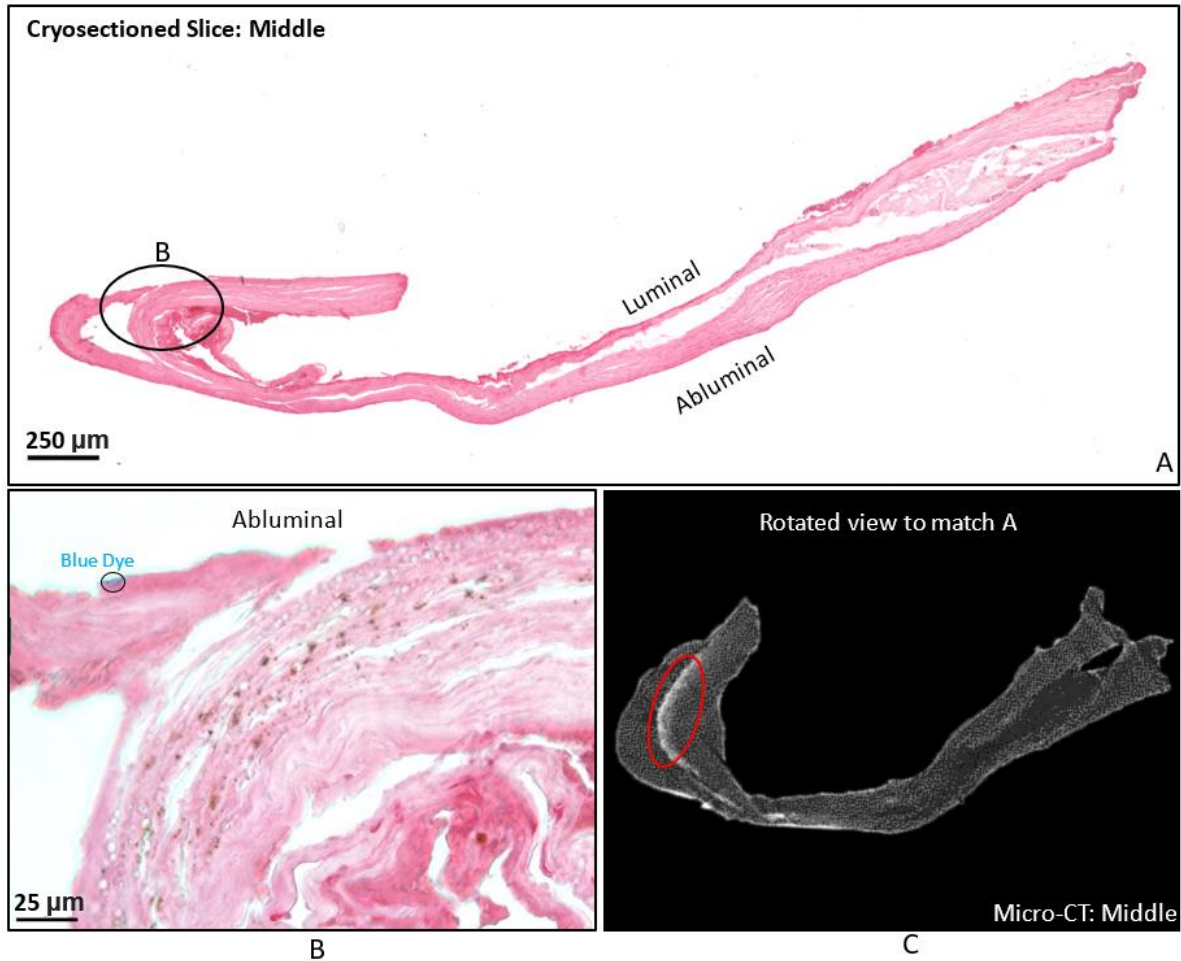


**Figure 31** Von Kossa staining of AGH 091. Subfigure A is a cross-section of AGH 091 stained with von Kossa. Subfigure B is a 40X zoom-in picture at the location as circled in black and labeled accordingly in subfigure A. Subfigure C is the micro-CT image taken at the associated depth.

## **4.0 DISCUSSION**

### **4.1 CONFIRMATION OF CALCIFICATION AND LIPID POOLS IDENTIFIED UNDER MICRO-CT**

One of the objectives for acquiring histology information was to confirm calcification and lipid pools as seen in micro-CT. For the purpose of confirming calcification, two histology staining techniques, namely Alizarin Red and von Kossa, were used to identify the location of calcification in a control cerebral artery and an aneurysm sample, after they had been scanned by micro-CT. In both the control and aneurysm case, the areas positively stained by Alizarin Red and von Kossa matched with regions identified in micro-CT with calcification, confirming these high grayscale regions in micro-CT as calcification. For the purpose of confirming the lipid pools identified under micro-CT by their lower grayscale, we used Oil Red O. Confirmation of the lipid regions via histology was more difficult because, using the current protocol, lipid regions peeled off frequently during the rinsing step. While the control cerebral artery slice was stained successfully, only cross-sections from the mid-region and bottom region, illustrated in Table 7, had evidence of lipids that was identifiable via bright-field microscope. Nonetheless, histology lipid areas matched with micro-CT data by appearing either as positive Oil Red O stain, or as empty gaps indicating presence of lipid prior to staining.

## **4.2 CALCIFICATION LOCATION AND APPEARANCE IN THE ANEURYSM WALL**

The focus of this thesis is the development of protocols for visualizing calcification and lipids in cerebral aneurysm tissue. Therefore, rather than studying a large number of samples, we focused on using multiple modalities to study two aneurysm samples. The findings for distribution of calcification and lipid in these samples were compared with findings in the published literature for the arterial wall, laying the ground work for future studies with a larger number of samples.

### **4.2.1 Distribution of calcification in the aneurysm wall**

In aneurysm sample AGH 091, from Section 3.3.4 in Chapter 3.0, staining with Alizarin Red and von Kossa showed calcification towards the abluminal side of the tissue, (Figure 29 and Figure 31). This same result was seen in micro-CT slices taken near the histology cross-sections, where calcifications were identified by grayscale value. Aneurysm tissue stained with OsteoSense and imaged under MPM also showed calcification in the outer wall. When imaging with MPM from the lumen, an OsteoSense calcification signal was seen that was not found using histology or micro-CT, Table 5 from Section 3.3.2. Because calcification was not seen in this region using micro-CT or histology and because this signal is different than that seen for the calcification in the abluminal side, it seems likely that this signal is a false positive. Further study is needed to address this issue.

#### **4.2.2 Calcification shape & size observed in the aneurysm wall under different modalities**

Although calcification has been reported in intracranial aneurysms using clinical scanning, it has not been investigated further. Clinical CT is able to scan at a voxel size of 156 to 300 microns in plane, and 300 to 500 microns in slice thickness [53]. Ex vivo, it is possible to use different modalities, in particular micro-CT and multiphoton microscope, and the resolution increases significantly, allowing ultrastructural analysis. One of the main contributions from this thesis is the development and application of protocols to use these latter image modalities to image calcification particles as small as 3 microns in diameter. Furthermore, we obtained information about the form and distribution of the calcification in a case study of two aneurysms. For example, from the multiphoton imaging results of AGH 091, calcification was seen to appear either as disperse singular ellipsoid particles, Table 8 category 1, or as aggregates. When aggregated, the shape of calcification becomes non-convex, Table 8 category 2, and sometimes even amorphous, Table 8 category 3. Such patterns were found to co-exist on the abluminal side. When analyzed under micro-CT, the largest aggregate was measured as 1.28 mm in diameter.

#### **4.2.3 Calcification in the artery wall**

Previous studies about the location of calcification have been primarily focused on atherosclerosis in the artery wall, in which calcification of the atherosclerotic plaque is limited to the subintimal space [34]. The appearance and shape of calcification in arteries is known to vary across the artery wall [44]. Calcium deposits in the intimal layer have been reported to be spherical shape measuring approximately 1.5 micron in diameter and composed largely of calcium phosphate [44]. Arterial calcification is a gradual and progressive process. Calcium

deposits have also been found in the media and are believed to be of a different etiology. These deposits are seen as lamellar structures, that are sheet like with sharp specular edges, consisting of calcium colocalized with cholesterol [44]. We have not found reports of calcification in the adventitial layer of arteries. In this regard, it should be recalled that aneurysm walls show diverse wall structures which includes a loss of distinct wall layers. Therefore, the calcification seen in the outer wall may or may not correspond to the adventitia of artery walls.

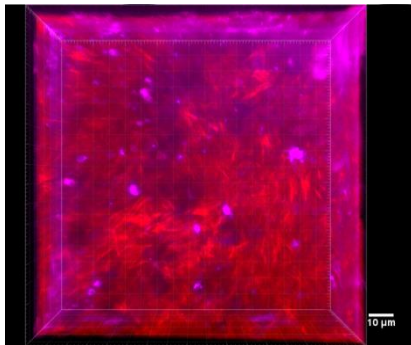
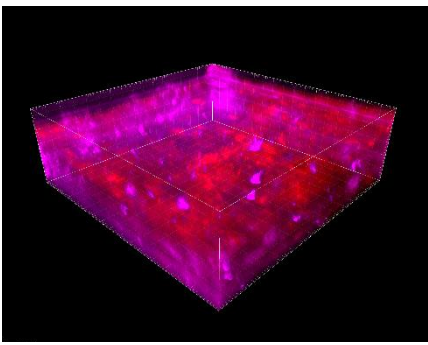
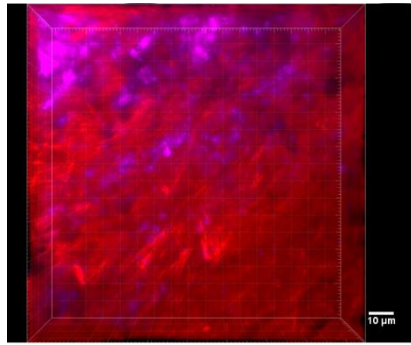
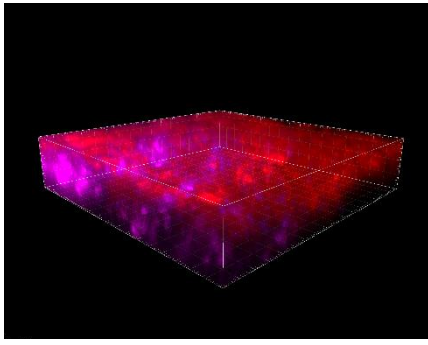
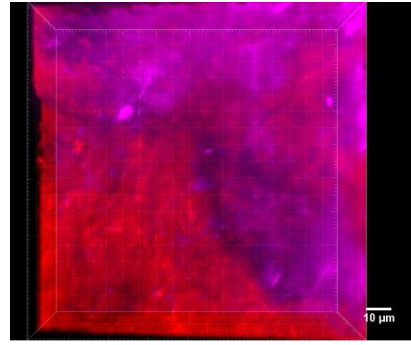
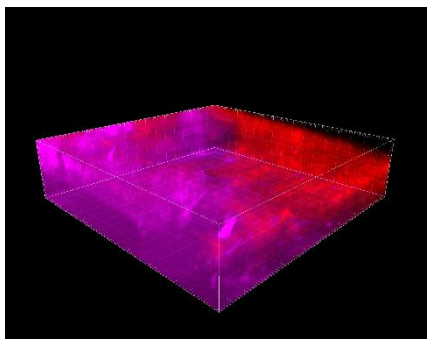
Atherosclerotic plaque calcification has been suggested by some as a biologically organized and regulated process. For example, Doherty et al. [34] believed that calcified plaque exhibits close similarities to new bone formation and remodeling.

#### **4.2.4 Comparison of calcification in the aneurysm and artery wall**

The goal of Table 8 is to compare calcifications in the aneurysm wall with atherosclerotic calcification. In terms of shape, there seems to be a commonality between the disperse particles, Category 1 in the aneurysm case, and the globular deposits identified from the atherosclerotic plaque, Table 8 $\alpha$ . But, Category 2 and Category 3, in the observed aneurysm, are fundamentally different from the other two lamellar shapes found in atherosclerosis, Table 8 $\beta$  and  $\gamma$ . The sheet-like structure from arterial atherosclerotic calcification appears to be much more organized than the non-convex, Category 2, and amorphous, Category 3, aggregation patterns in the aneurysm wall. Srinivasan et al. [44] conjectured that the lamellar shaped calcification in arteries are the result of colocalized calcium and cholesterol deposits. In comparison, substances near sites of calcification in an aneurysm have yet to be identified via additional histology analysis. Currently, this thesis only focused on finding correlations between lipid and calcification. Further, little is known about the growth of calcification deposits within the aneurysm wall. In arteries, the discrete

agglomerates of calcium depositions, Table 8a, are considered to be the initiating form of calcification in the atherosclerotic plaque [44]. For this reason, there is a possibility that, in aneurysm tissue, the disperse particles from Category 1 also play a critical role in leading the development of the observed shapes in Category 2 and Category 3 walls.

**Table 8** Examples of calcification patterns for aneurysm calcification categories 1-3 and descriptive summary of histological findings for categories  $\alpha$   $\beta$   $\gamma$  that have been used for atherosclerotic plaque

Calcification Pattern in an aneurysm, denoted as AGH 091			Atherosclerotic plaque	
	Calcification Appearance 2D	Calcification Appearance 3D		SEM morphological and ultrastructural characterization of calcified deposits, provided by Srinivasan et al. [44]
Abluminal (Category 1)			Luminal intimal surface	( $\alpha$ ) Tiny nodular aggregates of calcium on the luminal aspect of plaque
Abluminal (Category 2)			Luminal intimal surface	( $\beta$ ) Plate like lamellar calcification seen piercing the intima
Abluminal (Category 3)			Media	( $\gamma$ ) Crystalline plaques of calcium on the irregular surface of an atheromatous plaque

### 4.3 COLLAGEN FIBERS NEAR CALCIFICATION IN ANEURYSM TISSUE

As can be seen in Table 8, collagen fibers among the three categories appear to localize around calcification, rather than to penetrate it. Hutcheson et al. [45] suggested that collagen acts as a scaffold and directs the aggregation and calcification of extracellular vesicles. From in vivo experiment [45], degradation of collagen was found to be one requirement for the formation of calcification aggregates. Also, when unencumbered by collagen, microcalcifications could serve as building blocks for larger calcifications [45].

Figure 32 shows an example from MPM results where two types of calcification patterns are seen in the aneurysm specimen, one as the disperse particles pointed by blue arrows, and the other as non-convex aggregations pointed by white arrows. The two patterns appear to localize near each other with less than 100 microns apart. The blue and white circles correspond in color with the arrows. There appears to be a correlation between the pocket size created between collagen and the size of calcification. Smaller pockets, as seen in the blue circled area, appear with some light red signal indicating collagen near disperse calcification particles. But, the larger pocket, as circled in white, has no sign of collagen and shows the primary signal as arising from aggregated calcification in magenta. As reported in [45], collagen and calcification interactions are correlated inversely in arteries. There is therefore a possibility that such correlation also applies to the aneurysm tissue. But, due to the limitations in the z-stack resolution, more processing work on the tissue would be required to distinguish the morphology of collagen fibers.

According to [46], over fixation by immersing tissue in paraformaldehyde will increase autofluorescence. This article suggested that fluorescence coming from fluorescent labels will almost always be much brighter and more distinctive at specific locations than autofluorescence [47].

Autofluorescence appears dim and relatively uniform [47]. Because the aneurysm specimen studied for this thesis was fixed longer than usual, it is possible that the cloudy collagen signal on the luminal side was due to over fixation and the collagen signal could be improved in general by decreasing the fixation time.

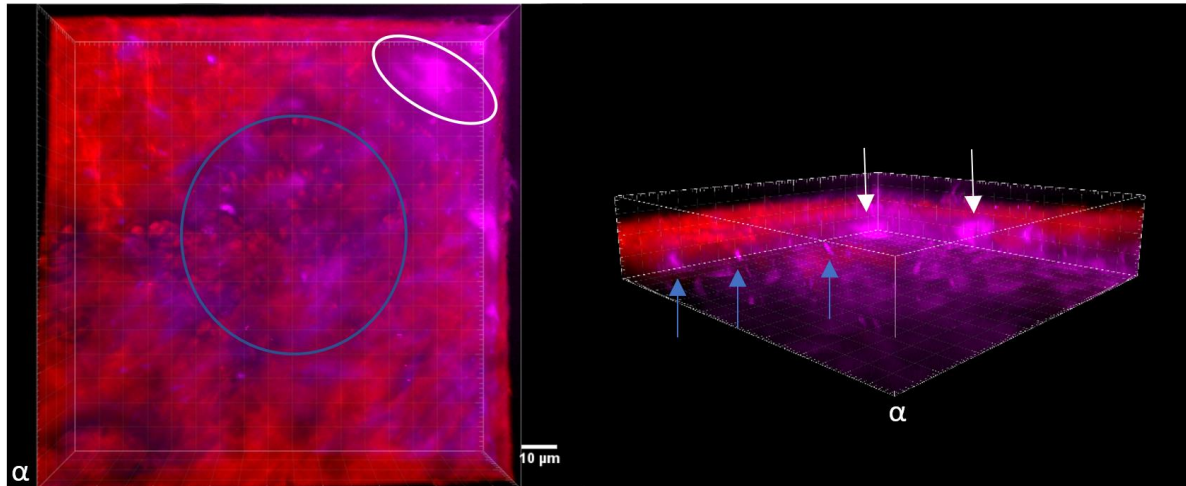


**Figure 32** Mix of calcification patterns from category 1 and category 2.

#### 4.4 LIPID POOL AND CALCIFICATION

In atherosclerosis, calcification is found within the plaque, and associated with lipid accumulations [22]. Specifically, the plaque is composed of cellular debris containing lipids, calcium, and fibrous connective tissue between the endothelium lining and the smooth muscle cell-rich medial wall [48]. In the aneurysm samples considered in this thesis, as shown in Figure 33, calcification and lipid do not appear to colocalize, results consistent with findings in the micro-CT image. In a recent study of 56 human aneurysm samples [49], Gade et al. identifies three categories of calcified walls based on the relationship between lipid pools and calcification in aneurysms and calcification size

and clustering. In comparison, the non-colocalization finding from the tissue studied in this thesis, AGH 091, corresponds with the type IIB category in [49], where lipid pools are present but not localized with aggregated micro or macrocalcifications.

Furthermore, we did not find regions in the aneurysm tissue that resemble the necrotic core from atherosclerosis. These results suggest changes in the aneurysm wall associated with calcification and lipid pools may represent a different pathology than that in atherosclerotic arteries and therefore the rupture process may also be different from that of an atherosclerotic wall.

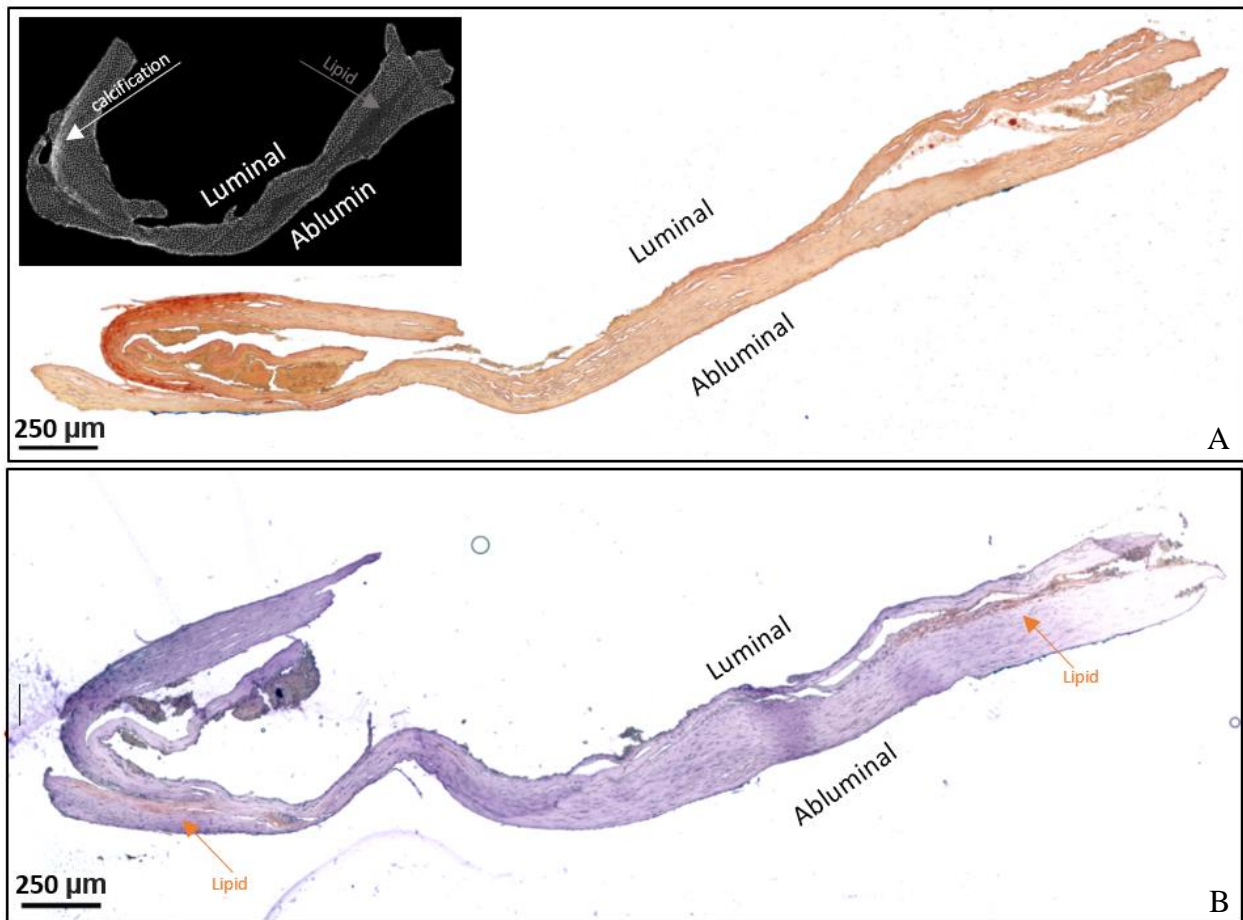


**Figure 33** Location of lipid and calcification in the aneurysm sample AGH 091. Subfigure A and B are images of Alizarin Red and Oil Red O stained cross-sections, reproduced here from Figure 29G, and Figure 30E respectively.

## 4.5 COMPARISON OF DIFFERENT MODALITIES

Table 9 compares three different modalities that were applied to the calcification study in aneurysm tissue, and summarizes the advantages and disadvantages of each. The main contribution from using these modalities together is that they provide complimentary information and also validation across modalities. When used together, they increase the robustness of our understanding about calcification at different scales. For the first time, details about calcification location, morphology, interaction with collagen, and mineral composition in aneurysm tissue are demonstrated here as one complete set of information.

Table 9 Comparison of different modalities for imaging calcification and collagen

		Multiphoton with OsteoSense	Micro-CT	Histology
Visualization Dimensions		3D & 2D	3D & 2D	2D
Co-imaging calcification and collagen		Yes	No	No
Identification of calcification		Requires staining	Doesn't require staining	Requires staining
Identification of collagen		Doesn't require staining	No	Requires staining
Need for prior tissue processing, other than staining		No	No	Fixation and cryosectioning
Handling environment		Room temperature	Room temperature	Environment varies based on the protocol between -80°C, -20°C, 4°C, and room temperature.
Timeframe for data collection	Processing time	Minimum at 48 hours with OsteoSense	No prior tissue processing required	2 days (dehydration with sucrose, OCT embedding, and cryosectioning)
	Imaging time	≈ 30 minutes/ stack of images	Range from 2 to 12 hours	Time based on speed of manual operation, but typically ≈20 mins/montage
	Acquisition size	a stack of 50 images, each with 500-micron by 500- micron in plane at 2-micron step size	Entire tissue	One cross-section of the tissue in 2D
Places for human errors		Scope settings, image quality	Equipment settings	All steps throughout the protocol
Exposure to chemical hazard		No	No	Yes
<b>Summary</b>				
Major Advantage		Non-destructive for imaging collagen	Minimum tissue processing required	Clear identification of composition at cellular level
Major Disadvantage		Risks associated with signal attenuation/overly magnified	Unable to identify collagen	Human artifacts

## 4.6 MECHANICAL IMPLICATIONS OF THE CALCIFICATION STUDY IN ANEURYSM TISSUE

There is a gap in knowledge about what causes an aneurysm to be vulnerable to rupture. Collagen fibers in the aneurysm tissue have been considered to be the major contribution to its mechanical behavior, and so a great focus has been given to the collagen fibers themselves as well as their organization. Humphrey (2002) [50] suggested that rupture may in part be explained by the difference in the rate of collagen turnover at different regions, and the higher the production rate in collagen, the stronger the weakening effects arising from immature collagen. Previous studies generally assumed that only collagen fibers provide load-bearing capacity to the aneurysm wall, after a loss of media, [51][52]. For example, in modeling cerebral aneurysm growth, Kroon et al. [51] proposed that the aneurysm wall consists of  $n$  discrete and distinct layers of collagen fibers, and that there is a continuously ongoing process of production and degradation of collagen in each layer. In their conjecture, as the degradation of the media proceeds, an increasing part of the load from the static blood pressure is transferred onto the adventitial collagen.

However, from the multiphoton images discussed earlier, calcification was found between collagen fibers. Different patterns were identified and used to define categories of the collagen-calcification interactions. Based on our findings, it appears that calcification particles and aggregates are localized to fill cavities between collagen fibers, and can vary significantly in shape. For this reason, we expect some calcification deposits will impact on load bearing when collagen fibers are recruited under load. As mentioned previously, calcification found in atherosclerosis can lead to both stabilization and deterioration of the plaque. Thus far, calcification minerals have only been included in computational studies in a handful of cases [54][55]. Information about the

organization and morphological characteristics of calcification will provide important guidance for designing computational studies of aneurysm biomechanics that includes collagen interaction with the calcification.

#### **4.7 FUTURE DIRECTIONS**

Streamlined protocols and associated preliminary investigations of calcification in the aneurysm wall were developed from this thesis to support future studies of calcification in cerebral aneurysms. They will be used in a large, ongoing study of sources of weakness and strength in the walls of cerebral aneurysms. In particular, the validation of the micro-CT protocol for identifying calcification and lipid pools in fresh, intact aneurysm specimens is of great use for this work. Furthermore, the development of the OsteoSense protocol for simultaneous imaging of calcification and collagen fibers under MPM, enables us to directly study the relationship between collagen fibers and the calcified regions as well as to identify different categories of wall calcification. Currently, these relationships were only evaluated qualitatively, and additional post processing analysis can be performed to quantify these relationships.

There were some limitations in the current study that can be addressed in future studies. For example, the positive OsteoSense signal on the luminal side of the aneurysm wall needs to be reconsidered. In this regard, the fixation time frame should be systematically tested to determine if this is a source of autofluorescence. With regards to mapping methodologies, shifting from a manual technique to one that is fully automated for positioning specimens under the multiphoton microscope will expedite imaging, and also increase the accuracy for mapping the location of the MPM results back to the physical tissue.

## BIBLIOGRAPHY

- [1] N. Chalouhi, B.L. Hoh, D. Hasan. Review of Cerebral Aneurysm Formation, Growth, and Rupture. *Stroke*, 44 (2013), pp. 3613–3622.
- [2] Seibert B, Tummala RP, Chow R, Faridar A, Mousavi SA, Divani AA. Intracranial Aneurysms: Review of Current Treatment Options and Outcomes. *Frontiers in Neurology*. 2011; 2:45.
- [3] I. Jalava, L. Pyysalo, M. Alanen. Regional Differences in the Incidence of Aneurysmal Subarachnoid Haemorrhage in Finland. *Acta Neurochirurgica*, (2017) 159: 1657.
- [4] H. Ohkuma, H. Tabata, S. Suzuki, and M. S. Islam. Risk Factors for Aneurysmal Subarachnoid Hemorrhage in Aomori, Japan. *Stroke*, 34 (2003), pp. 96-100.
- [5] Keedy, A. An Overview of Intracranial Aneurysms. *McGill Journal of Medicine*. 2006; 9:141-146.
- [6] Krings T, Mandell DM, Kiehl TR, Geibprasert S, Tymianski M, Alvarez H. Intracranial aneurysms: from vessel wall pathology to therapeutic approach. *Nature Reviews Neurology*. 2011; 7:547-559.
- [7] Weir, B. Unruptured intracranial aneurysms: A review. *J. Neurosurg*. 2002; 96: 3–42.
- [8] Wiebers DO, Whisnant JP, Huston J III. Unruptured intracranial aneurysms: natural history, clinical outcome, and risks of surgical and endovascular treatment. *Lancet* 2003; 362:103-110.
- [9] Lall RR, Eddleman CS, Bendo BR. Unruptured intracranial aneurysms and the assessment of rupture risk based on anatomical and morphological factors: sifting through the sands of data. *Neurosurgical Focus* 2009; 26: E2.

- [10] Thompson BG, Brown RD Jr, Amin-Hanjani S, Broderick JP, Cockroft KM, Connolly ES Jr. Guidelines for the management of patients with unruptured intracranial aneurysms: a guideline for healthcare professionals from the American Heart Association/American Stroke Association. *Stroke*. 2015; 46:2368–2400.
- [11] Fratzl P (2008) *Collagen: structure and mechanics*. Springer, Boston, MA.
- [12] V.S. Fennell, M. Y. S. Kalani, G. Atwal, N.L. Martirosyan, and R. F. Spetzler. *Biology of Saccular Cerebral Aneurysms: A Review of Current Understanding and Future Directions*. *Frontiers in Surgery*, vol. 3:43, 2016.
- [13] Aoki T, Kataoka H, Morimoto M, Nozaki K and Hashimoto N (2007) Macrophage-derived matrix metalloproteinase-2 and -9 promote the progression of cerebral aneurysms in rats. *Stroke* 38:162–169.
- [14] Wang Y, Emeto TI, Lee J, Marshman L, Moran C, Seto SW, Golledge J. Mouse models of intracranial aneurysm. *Brain Pathol.* (2015) 25(3):237–247.
- [15] Chalouhi N, Ali MS, Jabbour PM, Tjoumakaris SI, Gonzalez LF, Rosenwasser RH, Koch WJ, Dumont AS. *Biology of intracranial aneurysms: role of inflammation.*” *J Cereb Blood Flow Metab.* 2012, 32:1659–1676.
- [16] Starke RM, Chalouhi N, Ding D, Raper DM, Mckisic MS, Owens GK. Vascular smooth muscle cells in cerebral aneurysm pathogenesis. *Transl Stroke Res.* 2014; 5:338–436.
- [17] Rensen S. S., Doevendans P.A., van Eys G.J. 2007. Regulation and characteristics of vascular smooth muscle cell phenotypic diversity. *Netherlands Heart Journal.* 15:100-108.
- [18] Frösen, J. *The Pathobiology of Saccular Cerebral Artery Aneurysm Rupture and Repair -a Clinicopathological and Experimental Approach*. Helsinki University Press: Helsinki, 2006.
- [19] Frösen J. Smooth muscle cells and the formation, degeneration, and rupture of saccular intracranial aneurysm wall—a review of current pathophysiological knowledge. *Transl Stroke Res* 2014;5(3):347–356.
- [20] Sakaki, T.; Kohmura, E.; Kishiguchi, T. (1997) Loss and apoptosis of smooth muscle cells in intracranial aneurysms. Studies with in situ DNA labeling and antibody against single-stranded DNA. *Acta Neurochirurgica*, vol. 139, 469-475.

- [21] Kosierkiewicz TA, Factor SM, Dickson DW. (1994) Immunocytochemical studies of atherosclerotic lesions of cerebral berry aneurysms. *Journal of Neuropathology and Experimental Neurology*. 53: 399–406.
- [22] Lusis AJ. Atherosclerosis. *Nature*. 2000; 407: 233–241.
- [23] Gimbrone (Jr), MA. Vascular endothelium, hemodynamic forces, and atherogenesis. *The American Journal of Pathology* 1999. 155:1-5.
- [24] Libby P, Ridker PM, Maseri A. Inflammation and atherosclerosis. *Circulation* 2002; 105:1135–1143.
- [25] Insull, W. Jr. The pathology of atherosclerosis: plaque development and plaque responses to medical treatment. *The American Journal of Medicine*. 122, S3-S14 (2009).
- [26] Newby AC, Zaltsman AB. Fibrous cap formation or destruction – the critical importance of vascular smooth muscle cell proliferation, migration and matrix formation. *Cardiovasc Res*. 1999; 41:345–360.
- [27] Ross, Russell. The Pathogenesis of Atherosclerosis: a perspective for the 1990s. *Nature* 1993; 362:801-809.
- [28] Thompson B, Towler DA. Arterial calcification and bone physiology: role of the bone-vascular axis. *Nature Reviews Endocrinology*. 2012;8(9):529-543.
- [29] Leopold JA. Vascular Calcification: Mechanisms of Vascular Smooth Muscle Cell Calcification. *Trends in Cardiovascular Medicine*. 2015; 25:267-274.
- [30] F. Otsuka, K. Sakakura, K. Yahagi, M. Joner, R. Virmani. Has our understanding of calcification in human coronary atherosclerosis progressed? *Arteriosclerosis, Thrombosis, and Vascular Biology*, 34(2014), pp. 724–736.
- [31] Trion A, van der Laarse A. Vascular smooth muscle cells and calcification in atherosclerosis. *American Heart Journal* 2004; 147:808-814.
- [32] Leopold, Jane A. Vascular calcification: mechanisms of vascular smooth muscle cell calcification. *Trends in Cardiovascular Medicine*, 25 (2015); 25: 267-274.

- [33] Proudfoot D, Skepper JN, Hegyi L, Bennett MR, Shanahan CM, Weissberg PL. Apoptosis regulates human vascular calcification in vitro: evidence for initiation of vascular calcification by apoptotic bodies. *Circ. Res.* 2000; 87:1055–1062.
- [34] Doherty, T. M., Asotra, K., Fitzpatrick, L.A. Calcification in atherosclerosis: bone biology and chronic inflammation at the arterial crossroads. *Proceedings of the National Academy of Sciences USA.* 2003; 100: 11201–11206.
- [35] Demer LL, Watson KE, Bostrom K. Mechanism of calcification in atherosclerosis. *Trends Cardiovasc Med.* 1994; 4:45–49.
- [36] Maldonado N, Kelly-Arnold A, Laudier D, Weinbaum S, Cardoso L. Imaging and analysis of microcalcifications and lipid/necrotic core calcification in fibrous cap atheroma. *The international journal of cardiovascular imaging.* 2015; 31:1079–1087.
- [37] Vengrenyuk Y., Carlier S., Xanthos S., Cardoso L., Ganatos P., Virmani R. A hypothesis for vulnerable plaque rupture due to stress-induced debonding around cellular microcalcifications in thin fibrous caps. *Proc. Natl. Acad. Sci. U S A.* 2006;103: 14678 – 14683.
- [38] Wenk J, Papadopoulos P, Zohdi T. Numerical modeling of stress in stenotic arteries with microcalcifications: a micromechanical approximation. *Journal of Biomechanical Engineering* 2010; 132: 091011.
- [39] Cheng GC, Loree HM, Kamm RD, Fishbein MC, Lee RT. Distribution of circumferential stress in ruptured and stable atherosclerotic lesions: a structural analysis with histopathological correlation. *Circulation*, 1993, vol. 87 (pg. 1179–1187).
- [40] Huang H, Virmani R, Younis H. The impact of calcification on the biomechanical stability of atherosclerotic plaques. *Circulation*, 2001; 103: 1051–1056.
- [41] Huang, B. Q., and E. C. Yeung. Chemical and physical fixation of cells and tissues: an overview. In: *Plant Microtechniques and Protocols*, edited by E. C. T. Yeung, C. Stasolla, M. J. Sumner, and B. Q. Huang. Berlin: Springer, 2015, pp. 23–43.
- [42] Ustione A., Piston D.W. A simple introduction to multiphoton microscopy. *J. Microsc.* 2011; 243:221–226.

- [43] Cebal, Juan R., Duan, Xinjie, Gade, Piyusha S., Chung, Bong Jae, Mut, Fernando, Aziz, Khaled, Robertson, Anne M. (2016) Regional Mapping of Flow and Wall Characteristics of Intracranial Aneurysms, *Annals of Biomedical Engineering*, 44(12), pp. 3553–3567.
- [44] Srinivasan, A., Ramaswamy, V., Kuruvilla, S., Sehgal, P. K. & Balakrishnan, K. Calcified atherosclerotic plaque -where exactly is the calcium and what does it contain? *Indian Journal of Thoracic and Cardiovascular Surgery*. 28. 6-14 (2012).
- [45] Hutcheson JD, Goettsch C, Bertazzo S, Maldonado N, Ruiz JL, Goh W, Yabusaki K, Faits T, Bouten C, Franck G, Quillard T, Libby P, Aikawa M, Weinbaum S, Aikawa E. Genesis and growth of extracellular-vesicle-derived microcalcification in atherosclerotic plaques. *Nature Mater* 2016; 15:335–343.
- [46] Armor, Rumelo. Fixation – Using Paraformaldehyde. *QBI Histology and Microscopy*, 11 Jan. 2012, [web.qbi.uq.edu.au/microscopy/fixation-using-paraformaldehyde/](http://web.qbi.uq.edu.au/microscopy/fixation-using-paraformaldehyde/).
- [47] Armor, Rumelo. Autofluorescence. *QBI Histology and Microscopy*, 4 Nov. 2011, [web.qbi.uq.edu.au/microscopy/autofluorescence/](http://web.qbi.uq.edu.au/microscopy/autofluorescence/).
- [48] Insull, W. Jr. The pathology of atherosclerosis: plaque development and plaque responses to medical treatment. *American Journal of Medicine*, 122, S3–S14 (2009).
- [49] In prep
- [50] Humphrey, J.D., 2002. *Cardiovascular solid mechanics. Cells, Tissues, and Organs*. Springer, New York.
- [51] Kroon M., and Holzapfel G. A., 2007, A model for saccular cerebral aneurysm growth by collagen fibre remodelling,” *J. Theor. Biol.*, 247(4), pp. 775–787
- [52] Selimovic, A., Y. Ventikos, and P. N. Watton. Modelling the evolution of cerebral aneurysms: biomechanics, mechanobiology and multiscale modelling. *Procedia IUTAM* 10:396–409, 2014.
- [53] Burghardt AJ, Link TM, Majumdar S. High-resolution computed tomography for clinical imaging of bone microarchitecture. *Clin Orthop Relat Res*. 469, 2179-2193 (2010).

- [54] Robertson, A. M. et al. (2017) 'Role of Calcification in Aneurysm Failure – A Case Study', in Nithiarasu, P. and Robertson, A. M. (eds) 5th International Conference on Computational and Mathematical Biomedical Engineering – CMBE2017. Pittsburgh, pp. 52-55.
- [55] K.Y. Volokh, J. Aboudi. Aneurysm strength can decrease under calcification, *J Mech Behav Mater*, 57:164-174, 2016.